POLITECNICO DI TORINO

Master's Degree in Mathematical Engineering

Final Essay

Fatigue Analysis of Welds using nCode DesignLife

Tutors:

Luigi Preziosi, Giorgio Chiandussi

Company Tutor:

Simone Ferrero (Nova Analysis)

Candidate:

Lorenzo Lamia

Contents

Premise and Thanks

The aim of the thesis is to present fatigue analyses' results of welded joints and to compare them with experimental results in literature. The thesis is structured as follows:

- The first chapter will introduce the fatigue phenomenon and briefly explain how it is approached, then brief reviews of the fatigue histories of discoveries and of tragic accidents are presented.

- The second chapter will present the common design criteria in fatigue analysis. A description of the three basic fatigue analysis method will follow: Stress-Life, Strain-Life and Crack Growth. In this chapter, the main fatigue concepts are explained and the ideas introduced in the first part of the first chapter are developed.

- The third chapter is divided into two parts. In the first one, weld types and welding processes are illustrated, while in the second one the fatigue analysis methods for weld joints are introduced, with an explanation of their characteristics.

- The fourth chapter presents the software that will be used to perform fatigue simulations. The glyphs for weld analysis are illustrated, with an explanation of the theory behind them.

- The fifth chapter is the core of the thesis. In this chapter, the analysis setups and results will be presented.

- The sixth chapter briefly summarizes what has been done and draws the conclusions of the analyses.

- The seventh chapter contains all the FE models, grids and linear elastic analysis' results.

I want to thank Simone Ferrero for providing me with all the FE analyses and for his support and guidance during the thesis. I also want to thank my tutor professor Luigi Preziosi and my cotutor professor Giorgio Chiandussi for their reviews of my dissertation. Last, but not least, I want to thank my family and my friends for their support and precious advice.

Chapter 1

Introduction to Fatigue

In this chapter, an introduction to fatigue analysis is given. In the first part the basic approach to the problem is explained, then it follows a brief review of some of the most important achievements in the field. The last part highlights the importance of addressing the fatigue problem, presenting to the reader famous tragic accidents from the past.

1.1 What is fatigue?

The word "fatigue" finds its origins in the Latin expression "fatigare" which means "to tire"[8]. We can find definitions such as "Fatigue is the deterioration of a component caused by the crack initiation and/or by the growth of a crack" [4] or "Fatigue is the mechanical failure mechanism primarily caused by the repeated application of variable loads"[1].
Even if the second one is the most general and common definition, the first one highlights an important feature of the fatigue phenomenon which is typically characterized by crack nucleation and growth through the component until failure (at least for the vast majority of industrial materials). In the second definition it is also important to interpret the word "loads" in its broader sense. I think that "stresses" is probably more fitting in this case since the word "loads" is often only interpreted as "mechanical loads", while,

with the word "stresses", careful readers will remember that there are various non-mechanical ways of inducing stress in a component (e.g. thermal stress). From the definitions, we can deduce that fatigue is some sort of damage which accumulates in the object of interest as a result of variable stresses and manifests itself in the form of cracks. What primarily drives fatigue will then be the stress range more than the stress peak itself, which plays a secondary, but still important, role.

Another delicate point is the fact that since the damage accumulates in the component we can't neglect it just because stress ranges are small: the material doesn't recover from fatigue and it will eventually fail (unless we perform proper maintenance). What we can get from this is that we should always perform some kind of fatigue analysis (even just a rough one) if we want to avoid unexpected failures, even under small loads.

We can now highlight the main differences between fatigue and standard structural analysis. In the first case, we are dealing with variable loads, while in the second one we usually try to understand if the component can endure the static stress applied to it. Another important fact is that fatigue is a highly localized process, so it is influenced by local hot spots where the stresses concentrate and not so much by the global behavior of the structure.

Now that we have defined what fatigue is, it's easy to understand the concept of fatigue life: the amount of "time" that our component will endure under variable loads before failure. The word "time" usually means the number of load cycles or, in the case of variable amplitude cycles, the number of duty cycles (which are just blocks of cycles of variable amplitude). It becomes now clear that what we want to determine when we are performing fatigue analysis is the life of the component. In order to do that, we need three kinds of input data: material, geometry, and load history.

Material properties of the specimen are extremely important. Fatigue cracks nucleation and growth are caused by cyclic dislocation movements at the microscopic level. It is obviously not convenient to describe the process' details, so engineers usually divide the fatigue life in two phases. The life up to the macroscopic size (when the length of the crack is greater than the size scale of the intrinsic anisotropy of the material) is called the crack nucleation phase, while the rest of the component's life is called the crack growth phase. Properties like yield strength, ultimate tensile strength, elastic modulus, and stress-strain curves are essential to get a rough estimate of simple component fatigue life, while more detailed material fatigue life curves are necessary whenever we need more precise and reliable results.

The geometry of the specimen plays an important role in fatigue analysis as well. We have already underlined the fact that fatigue is a local process, driven by local hot spots. These hot spots are nothing more than places where the stresses concentrate due to the geometry of the component. Because of this, failing at properly describing and accounting for geometrical features could end up in severely miscalculating the fatigue life of the component! In the most simple and well-known cases (e.g. a circular hole in a steel plate) we could be able to use simple coefficients from the literature in order to account for the geometry of the specimen, but in more complicated cases, we will have to measure with precision the concentration effects due to the geometry.

The last input we must provide is the load history which is obviously necessary to quantify the stress history in the hot spots. This may seem trivial, but it's not always easy to identify the usage of the product: different clients will use it in different ways and one should try to account for them all! It is a crucial step because fatigue life is very sensitive to load range and a small difference could end up shortening the life of the component beyond expectations. Even if you have the proper load history you could have to manipulate it because of its length. It is indeed really expensive to run long fatigue experiments or FE analysis. This is not an easy task and it could, if performed improperly, lead to big overestimations of the fatigue life which is what should be avoided at all costs.

Finally, it's important to understand the statistical nature of fatigue life: All the components have at least microscopic differences that we cannot account for.

1.2 A bit of fatigue's history

The expression fatigue has been in use for a very long time but the first fatigue test was performed around 1829 by the German mining engineer W.A.J. Albert [1, 8]. In 1842-43, W.J.M. Rankine, a British railway engineer, studied the effects of stress concentration and sharp notches. Some years later, between 1852 and 1869, Wöhler, carried out full-scale fatigue tests on railway axles. He discovered how fatigue life was controlled by the stress range and measured the first stress-life curve (S-N curve). He also noted that below a certain amount of stress range the component seemed to not accumulate any damage. Gerber (1874) and later Goodman (1899) contributed to the development of methods to account for mean stress in fatigue cycles. Ewing, Rosenhain, and Humfrey (1900-03) investigated the fatigue of Swedish iron and showed the presence of slip bands which led to the formation of cracks. In 1910, O.H. Basquin redrew the S-N curve in a log-log plot, pointing out how the relationship between the logarithm of the stress range and of the number of cycles was linear over a large span of stress ranges. In 1845, Miner formulated a linear cumulative fatigue damage criterion based on the work done by Palmgren (1924). In the same years, Neuber studied the effects of a notch on the fatigue life. Coffin and Manson (1954) independently proposed an empirical relationship between fatigue life and plastic strain amplitude which will later pose the basis of the strain-life methodology. After the work of Inglis (1913), who studied the stress concentration factors of elliptical holes in infinite plates, and of Griffith (1920), who showed that cracks could remain stable if there wasn't enough energy to propagate them, Irwin (1957) introduced the stress intensity factor K to model crack effects. Following him, Paris, Gomez and Anderson first and then Paris and Ergodan (1961-63) suggested that crack propagation was controlled by the stress intensity factor range ΔK. After them, Elber (1968) discovered plasticity-induced crack closure, which is an important concept to explain some load sequence effects.

This brief overview of fatigue's history does not claim to be exhaustive at all. Many other researchers that gave important contributions to the fatigue's theory are omitted here, simply because a complete reportage of the fatigue's history is beyond the aim of this thesis.

1.3 The need to perform fatigue analysis

The need for fatigue analysis is the same as structural analysis: we want to avoid failure. Sometimes fatigue predictions are not needed just because their cost is higher than the losses due to the failure. Nonetheless, there are a lot of cases where estimating and improving the fatigue life of a component will end up in saving money or, even more importantly, lives. Unfortunately, the urge to study new phenomena has often occurred after tragic events and fatigue is not an exception to this rule. In 1842 a train returning to Paris from Versailles derailed because of fatigue failure of the locomotive front axle, which resulted in the loss of human lives. More than a hundred years later, in 1954, Comet G-ALYP, a passenger aircraft, crashed into the sea near Elba Island. Later, in the same year, Comet G-ALYY crashed near Naples while on a flight from Rome to Cairo. The Royal Aircraft Establishment affirmed that " ...the accident at Elba was caused by structural failure of the pressure cabin, brought about by fatigue" and that "Owing to the absence of wreckage, we are unable to form a definite opinion on the cause of the accident near Naples, but we draw attention to the fact that the explanation offered above for the accident at Elba appears to be applicable to that at Naples" [9].

Another example of an aircraft accident is that of a Boeing 737-200 in 1988 when it experienced an explosive decompression due to fatigue damage which led to the failure of a lap joint and the separation of the fuselage upper lobe (1.1). Ten years later a high-speed ICE train derailed, killing 101 people, at Eschede in Lower Saxony, Germany. The rim of one wheel failed under fatigue provoked by cyclic local deflections against rubber cushions: it is still one of the biggest tragedy in recent German history (1.2). Not only aircraft and trains are sensible to fatigue: on December 15, 1967, the Silver Bridge in Ohio collapsed with many casualties. It was supported by chain links instead of wire cables and that reduced the force path redundancy, therefore the failure of a single link, caused by the propagation of small cracks, resulted in the collapse of the bridge (1.3).

This incomplete series of catastrophes shows well how to account for fatigue damage is important in various dramatic applications, but there are a lot of examples of fatigue failures in our everyday lives. I, myself, experienced the fatigue failure of two of my hand-grippers after long usage. The first broke abruptly, while the second (of a different brand) cracked and then it still lasted a long time before completely breaking (1.4). This personal example let me also underline that in some way the second hand-gripper could endure better the presence of small cracks and this can be an important property in fatigue design.

I hope it is now clear to the reader why performing fatigue analysis should be part of the design process in many applications. I also want to underline the fact that there are a lot of ways of doing fatigue analysis from more reliable and expensive to rougher and cheaper ones: it is up to the design engineer to decide how many resources dedicate to it.

Figure 1.1: Boeing 737-200 (Photo by Robert Nichols/Black Star, iconicphotos.wordpress.com).

Figure 1.2: Eschede Train Disaster. Credit: Reuters, www.itv.com.

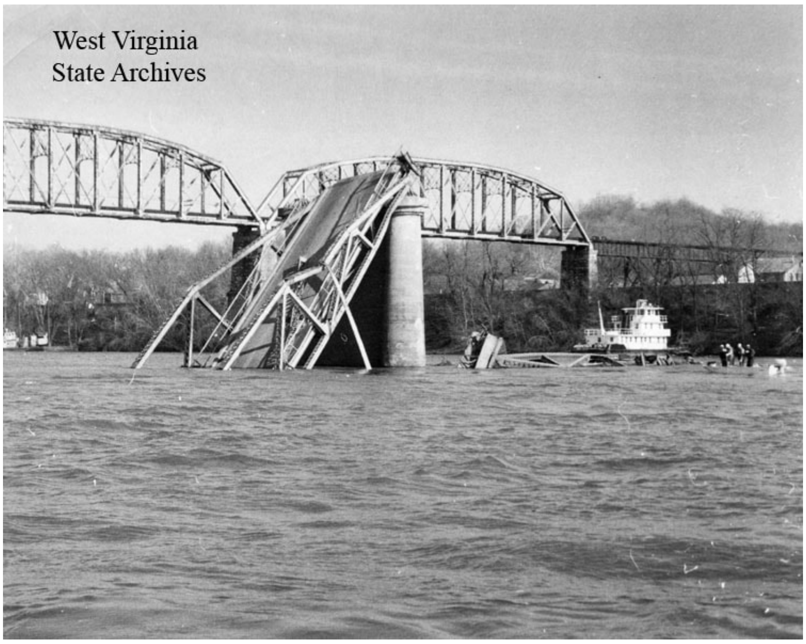

Figure 1.3: The scene of the Silver Bridge Collapse in 1967. (Photograph from the West Virginia State Archives, www.byrdcenter.org).

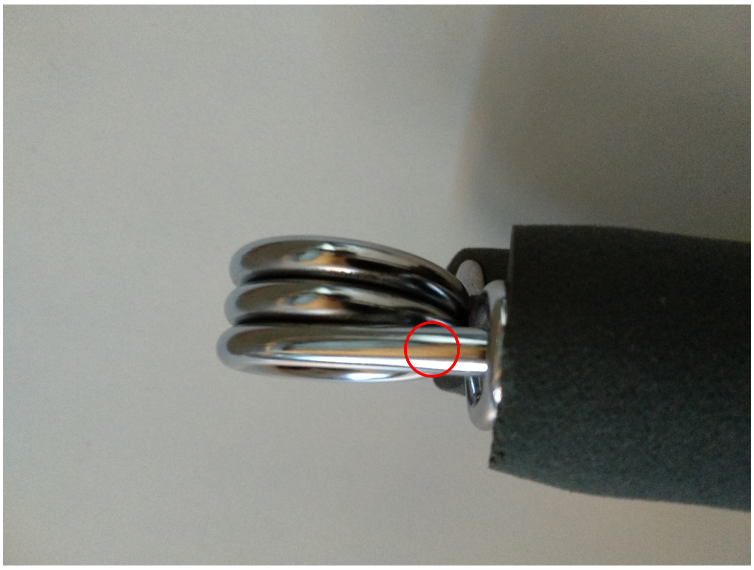

Figure 1.4: Hand gripper: the place where the crack started is circled.

Chapter 2

Fatigue Design Theory

In this chapter, firstly the fatigue design criteria will be presented, then, in the second section, the three basic fatigue life models are introduced.

2.1 Design criteria

Design criteria are very important in fatigue analysis since they will define how the component should be fabricated. There are four criteria: Infinite-Life, Safe-Life, Fail-Safe, and Damage Tolerant [10].

The Infinite-Life design criterion is the oldest one. As the name says the component should have an infinite life under the applied stresses. In order to obtain that, stresses and strains must remain well below the yield point, in the elastic region. Even if we do that, as has been said before, our component won't have an infinite fatigue life, but it could easily last many millions of cycles and that's often enough (the part could already have failed because of other reasons or could have just been replaced with a new version). This criterion is not economical and sometimes not even practical (e.g. due to weight restrictions).

The Safe-Life criterion consists in designing for a finite life including a safe margin for the variability of fatigue results. The margin could be given in term of stress (e.g. reduce the stress of 10%) or in term of life (e.g. the desired work life is one-tenth of the expected life) or both. This method is used when we don't need or don't want the Infinite-Life design, but we can't perform regular inspections.

The Fail-Safe design philosophy was the answer of the aircraft engineers to the impossibility of adding weight in order to ensure good safety factors and to the waste of money caused by always retiring components way before their average test life was obtained. The main concept of this criterion is that the system must not fail if one part fails. Engineers acknowledged that cracks nucleation was possible and so they started to design parts with that in mind: the component should endure cracks enough for them to be detected and repaired. This is for example achieved with multiple load paths (the careful reader will remember what happened to the Silver Bridge 1.3), crack arrestors, and periodic inspections.

The Damage-Tolerant design assumes that cracks already exist in the structure and want to determine if they will lead to failure and how much it will take in order to find the optimal inspections' schedule. If no cracks are found, the analysis is performed as if cracks of the smallest detectable dimension exist. It requires fracture mechanics knowledge to model the crack growth behavior and crack detection methods for the analysis of the length and size of cracks. This criterion can lead to huge savings if compared to the safe-life methodology but can have disastrous consequences if not applied well.

2.2 Fatigue life models

There are four well-known methods for fatigue analysis: Stress-Life, Strain-Life, Crack-Growth, and the Two-Stage method.

The Stress-Life method, also called the S-N method, aims to express the relationship between stress range and life cycles through a simple life curve. This method works pretty well for high-cycle fatigue. The Strain-Life method, also known as the E-N or ε-N method, expresses the same relationship but using strain instead of stress. This allows to account for plasticity effects, neglected by the S-N methodology, and for this reason, it is appropriate for both low and high-cycle fatigue (though it is not frequently used in the second case since it's just easier to apply the S-N method). These first two methods don't model the crack-growth phase of fatigue. There are, however, cases where the Crack Growth model is needed to evaluate the speed of the advancement of defects. In such cases, the Crack Growth approach may provide useful predictions. Finally, sometimes the fatigue life is dominated neither by the first phase nor by the second. In these cases, we must account for both phases combining an E-N model for the crack nucleation phase and a Crack Growth model to determine the life from the end of the first phase up to the rupture of the component.

Before starting with the description of the methods it is necessary to highlight the fact that, as in every engineering application, the model can, at most, give as good outputs as the inputs it has received. So it is necessary to properly measure the material properties, the geometry, and the load history: if we get those wrong we cannot expect to get decent results. It is then equally important to spend resources on both the models' and the measurements' part since our results will be at most as good as the worst of the two parts.

2.2.1 The S-N method

Being the simplest design method, the Stress-Life methodology is widely applied in industry. "S-N models assume fatigue damage in any complex structure can be properly simulated by describing the damage evolution at its critical point, supposing it is caused by the stress history that loads it in service" [1]. This means that we can just use small test specimens that accurately reproduce the critical points (same material and same local details) of the structure and then apply to them the same stress history of the hot spots. The S-N procedure is often used when the stresses are low and the crack initiation life is long. It assumes that the fatigue damage is driven by stress at the hot spot of the structure and that the behavior of the component is macroscopically elastic. This is a really important concept because fatigue damage is always caused by cyclic plastic deformations, but they can be macroscopic or microscopic. We have in fact already explained how cracks are formed by slip bands due to cyclic deformations at critical points, usually in the direction of the maximum shear stress. After that, the crack starts to grow in the direction perpendicular to the maximum normal stress, in order to avoid friction given by the contact of the faces.

The method follows three main steps. Firstly, the fatigue strength at the critical point is determined, then the stress history considering all the geometry effects must be properly assessed, finally, all the damage induced by each load cycle is summed.

Determine the fatigue strength

In order to determine the fatigue strength we need a stress-life curve, so we have to perform fatigue tests. This is a very delicate aspect of fatigue analysis since while it is important to run tests, they are quite expensive. The best possible case is when we can perform fatigue tests on the whole structure under actual service load histories so that our calculations will be as reliable as possible. This procedure, even if desirable in complex structures that require high reliability, it is rarely seen because of its high costs. It is though used when safety is the most important factor, as in the aerospace industry, and when the mass production dilutes costs, as in the automotive industry [1]. The second best option would be testing only the critical components under service loads, or, if it is not possible, under constant amplitude load blocks (Gassner's approach). It could seem strange to the reader (it was for me when I learned about this), but even the second procedure is often too expensive and, in that case, we can measure their critical points fatigue strength with test specimens designed to reproduce their behavior. Again, we can simplify the test using the Gassner's approach. When also these options are impracticable, what can be done is to test the material fatigue strength instead of the component's one under real service loads or Gassner blocks. These tests are less expensive since standard test specimens don't cost too much and for constant amplitude loading we don't even need the equipment that reproduces the service loads. However, everything comes with a price and, in this case, the price is the accuracy. We are no more testing the component with its details, but just its material. We are not accounting for the geometry and we have to do it in our model but, remember, estimating the effects of the geometry is always worse than measuring them and should be avoided when possible. Nonetheless, the last option is the one usually chosen in the classical S-N curves. Finally, when just a really rough estimate for simple design tasks is needed and testing can't be done, engineers estimate (recall how we should not estimate material properties, geometry's effects, and load history if possible?) the fatigue strength from material properties like ultimate strength S_U or Brinell hardness HB.

The fatigue life curve of the model takes the form:

$$NS_F^B = C \;\Rightarrow\; S_F = \left(\frac{C}{N}\right)^{\frac{1}{B}} \tag{2.2.1}$$

where N is the number of load cycles and $S_F = S_F(N)$ is the fatigue strength, while B and C are respectively the Wöhler (or Basquin) exponent and coefficient. This law can be transformed and seen in a log-log plot:

$$S_F = \left(\frac{C}{N}\right)^{\frac{1}{B}} \;\Rightarrow\; \log(S_F) = \alpha - \beta \cdot \log(N) \tag{2.2.2}$$

where $\alpha = \frac{1}{B} \cdot \log(C)$ and $\beta = B^{-1}$.

Usually this law fits well the experimental S-N points, but, in general, we can use any curve that better fits the data because it is not a physical law (I like to think of it as a kind of constitutive law). For example, another type of law used is:

$$S_F = \gamma - \lambda \cdot \log(N) \tag{2.2.3}$$

where γ and λ must be chosen so that our curve fits well the experimental data.

As already mentioned in the brief historical overview of fatigue; Wöhler also discovered that below a certain threshold of stress range the cycles weren't inducing any fatigue damage on the component. This threshold is called "fatigue limit" S_L and it could be equal to the fatigue strength around 10^6-10^8 $\Rightarrow$ $S_L \approx S_F(10^6\text{-}10^8)$, but it really depends on the material and there are even materials that do not present such limit (Fig.2.1). In those cases, usually, instead of having a straight horizontal line starting from the fatigue limit, the slope of the line is changed, making it less steep. Even for the materials (e.g. steel) that present the horizontal line after the fatigue limit, it is important to remember that this is an approximation, though a pretty good one, because the component always accumulates damage. However, it wouldn't be smart at all to perform tests for 10^7-10^8-10^9 cycles in order to obtain data for small slope's corrections: the long tests are extremely expensive, the correction is pretty small and it could also be useless because it's rare to have such low stresses. Since the fatigue limit tells us for which stress ranges the part does not accumulate damage, it is useful when we want to design for infinite life.

Looking at an S-N curve (Fig.2.1), we will note that the x-axis does not start from 1 cycle but from 10^3-10^4 and that could seem strange: why it starts from 10^3-10^4? why don't we just prolong the line? The problem is that under 10^3-10^4 cycles we are already in the low-cycle part and we can't use the S-N method for the vast majority of low-cycle fatigue lifes, so it is better to start from the high-cycle zone in order to avoid possible mistakes.

Note that often the modern S-N curves are given with the stress amplitude $S_A = \frac{\Delta\sigma}{2} = \frac{\sigma_{max}-\sigma_{min}}{2}$ instead of the stress range $\Delta\sigma$, also pay attention to the fact that sometimes the x-axis corresponds to the number of reversal $R_f = 2N_f$: each cycle correspond to two reversals.

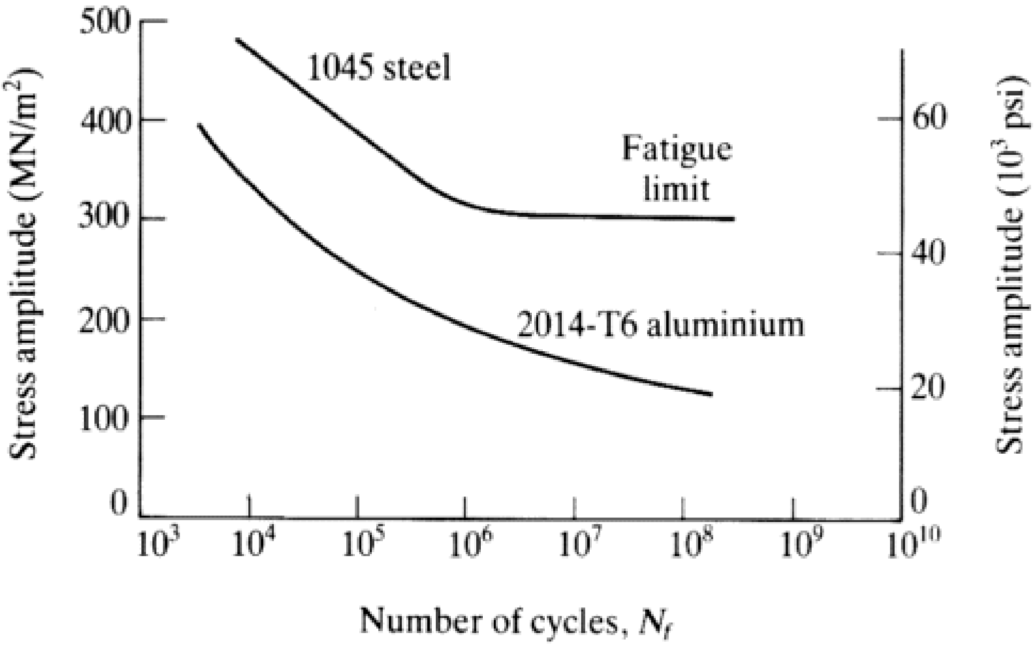

Figure 2.1: 1045 steel and 2014-T6 aluminium S-N curves (Picture by www.efunda.com).

Another possible trap is to confuse the material S-N law and the component S-N curve. As we learned above, there are many ways to perform fatigue tests, we could test the component or the material, but, as already underlined, the second procedure does not account, by itself, for all the properties of the component: don't even think of taking the material S-N curve and using it for your component! The only case where you could actually do that would be when your component is exactly the same (and here I don't mean only same geometry and material because we will see that there are also other important factors) as the specimens which are used in the tests. In this pathological case the material curve is also the component curve, but, in

general, those two are different! A reasonable question is now how to obtain the component S-N curve when only the material curve is known and the answer is in the usage of corrector coefficients. Among them we can find the surface finish factor k_{sf}, size factor k_{sz}, load type factor k_{lt}, fretting factor k_{ft}, surface treatment factor k_{st}, temperature factor k_{Θ} and reliability factor k_{RI}.
The surface finish factor k_{sf} accounts for the type of material surface, the more the surface is rough the more the coefficient is small. In fact, a rough surface will have a lot of valleys where cracks can easily start, so it will have a reduced fatigue life. It's not easy to evaluate the surface roughness and it's not obvious what correction we should apply. There are various parameters to quantitatively describe the surface roughness: for example if the mean roughness of the surface is known and if we are lucky enough to work with well-known materials, it could be possible to find a plot of the surface finish factor like the one in Fig.2.2.

When such measurements can't be done, we should look at graphics that plot the k_{sf} coefficient for different finish operations like in Fig.2.3. The biggest problem is to find such curves for your material and how much you can trust them. Remember that we are already estimating the component effects instead of measuring them, if we also don't do it properly we will end up with completely wrong results. One general rule of thumb that we can deduce from these plots is that the surface factor has a greater impact on high strength materials.

The size factor k_{sz} and the load type factor k_{lt} account for the effect of the stress gradient. "The driving forces for fatigue crack initiation are the stress range and the maximum stress that load the critical point, but many experts believe cracking is caused by their mean values evaluated in a small characteristic material volume V_C located there..." [1]. In case of bending, the k_{sz} (for tensile test $k_{sz} = 1$) accounts for the fact that, while in small specimens the stress quickly decreases, in the large components the stress will remain high near the critical point. However, such a concept of V_C is

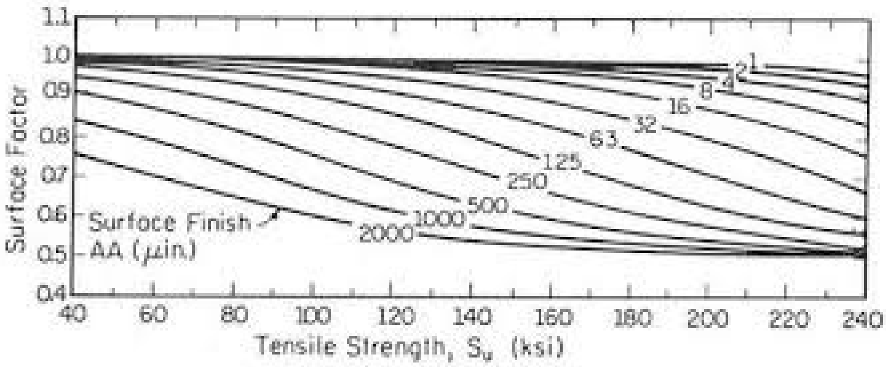

Figure 2.2: Surface factor given the tensile strength and the mean roughness for steel [12].

not really clear and we don't know what the size of V_C should be in general. Moreover, size-effects could also have another reason. It is more difficult to make high-quality large specimens than smaller ones, so the difference in performance could also be attributed to the presence of more defects, like vacancies or inclusions, in the bigger specimens. The load type factor, on the other hand, should account for the different type of load. For bending loadings $k_{lt} = 1$, while for tensile loadings $k_{lt} < 1$. Since both these two factors account for stress gradient's effects and are given in pretty heuristic ways, I have to agree with the authors of [1] when they say that it would be more reasonable to unify them in one stress gradient factor k_{sg}.
"Fretting is a superficial damage mechanism caused by small cyclic movements between contacting surfaces that transmit compressive loads" [1]. The fretting factor k_{ft} is a simple empirical way to account for fretting when its effects aren't negligible. The surface treatment factor $k_{st} > 1$ considers the beneficial effects of induced residual compressive stresses in the component. It is indeed well-known that they can delay or even stop the propagation of a crack.
The temperature factor k_Θ allows to express the dependence of the material properties from the temperature when those are relatively low ($\Theta_w <\sim 0.3 \cdot \Theta_f$, where Θ_w is the working temperature and Θ_f is the melting temper-

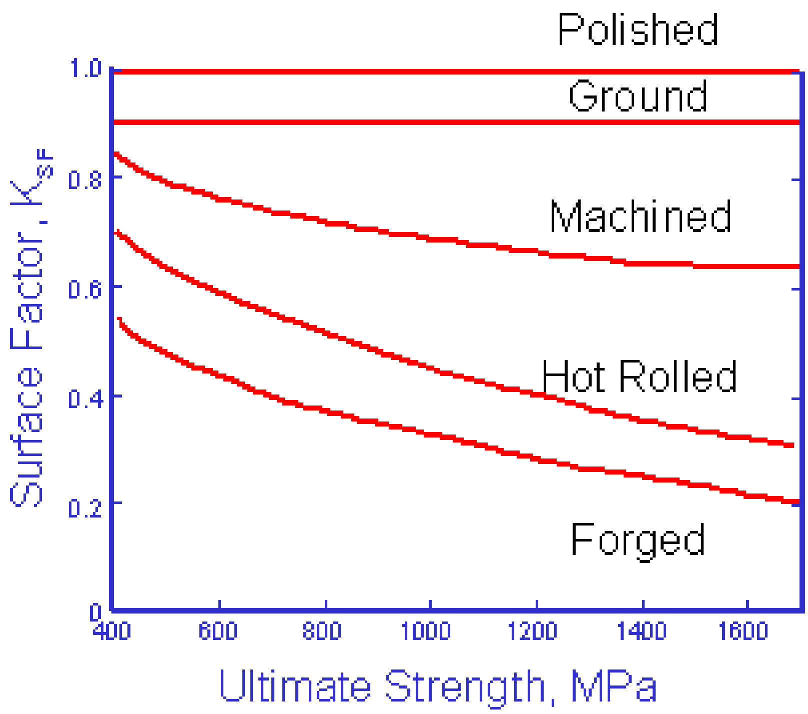

Figure 2.3: Surface factor given the tensile strength and the finish operation [17].

ature). Since the temperature has a negative effect on the fatigue properties of the material $k_\Theta \leq 1$.
Finally, the reliability factor k_{RI} is used as a safety factor to ensure that the vast majority of the components will have at least the fatigue strength that we are taking from the S-N curve. One way to calculate it is to fix the stress amplitude and make some assumptions on the probability distribution. After that, it is possible to use that distribution to calculate, for each stress range, the number of cycles that e.g. 90% of the specimens will endure. Interpolating in this way we obtain a new S-N curve with a 90% survival rate. Usually k_{RI} is evaluated at the two extreme values of the linear zone $k_{RI}(N_{EL})$ and $k_{RI}(N_L)$, where N_{EL} is the "elastic limit" (normally 10^3-10^4) of the plot and N_L is the lowest number of cycles corresponding to the fatigue limit S_L in the S-N curve.

The two values $S_F(N_{EL})$ and $S_F(N_L)$ are then modified and a new function $S_F^*(N)$ is obtained. The S-N curve $S_F'(N)$ for the component will then be defined as:

$$S_F'(N) = \begin{cases} S_F^*(N) & \text{if} \quad N_{EL} \leq N \leq N_L \\ S_F^*(N_L) & \text{if} \quad N > N_L \end{cases} \tag{2.2.4}$$

but first, it is important to make a clarification. The effects of these coefficients are not the same for both high and low number of cycles. In fact, besides the reliability and the temperature factors, the other corrections are not relevant at $N \sim 10^3$ and are thus not considered. $S_F^*(N)$ is defined by:

$$\begin{cases} S_F^*(N_{EL}) = k_\Theta \cdot k_{RI} \cdot S_F(N_{EL}) \\ S_F^*(N_L) = k_{ft} \cdot k_{sf} \cdot k_{st} \cdot k_{sg} \cdot k_\Theta \cdot k_{RI} \cdot S_F(N_L) \end{cases} \tag{2.2.5}$$

where the k_{sg} accounts for both k_{lt} and k_{sz}. Now we just have to find our two coefficients such that the line will pass through the points $(N_{EL}, S^*(N_{EL}))$ and $(N_L, S^*(N_L))$, let's take for example the law $S_F = \gamma - \lambda \cdot \log(N)$, in this case we have to solve:

$$\begin{cases} S_F^*(N_{EL}) = \gamma - \lambda \cdot \log(N_{EL}) \\ S_F^*(N_L) = \gamma - \lambda \cdot \log(N_L) \end{cases} \tag{2.2.6}$$

which results in

$$\begin{cases} \lambda = \dfrac{S_F^*(N_L) - S_F^*(N_{EL})}{\log(N_{EL}) - \log(N_L)} \\ \gamma = S_F^*(N_L) + \lambda \cdot \log(N_L) \end{cases} \tag{2.2.7}$$

Now putting together (2.2.5), (2.2.6) and (2.2.4) we get:

$$S_F'(N) = \begin{cases} \gamma - \lambda \cdot \log(N) & \text{if} \quad N_{EL} \leq N \leq N_L \\ \gamma - \lambda \cdot \log(N_L) & \text{if} \quad N > N_L \end{cases} \tag{2.2.8}$$

where λ and γ are given from equation (2.2.7).

Determine the stress history in the hot spot

We have, thus far, obtained an S-N curve for a component with the same geometry as the test specimen, but what if also the geometry is different? For complex geometries it is necessary to perform an adequate structural FEM analysis in order to obtain the stress in the critical point, but for easier ones (e.g. a hole in a plate) it is possible to find the Linear Elastic stress concentration factor $K_t = \sigma_{\max}/\sigma_n$, where $\sigma_{\max}$ is the maximum stress in the hot spot and σ_n is the nominal stress that would act in the hot spot if there wasn't the notch. K_t is basically an indicator of the difference between the stress at the notch tip and the stress far away from it. This coefficient depends on the type of load (e.g. bending or torsional), and obviously on the geometry (note that in the case of multiaxial stresses, it also depends on the chosen stress). It can be neglected in static analyses of ductile structures that can locally yield, but not in fatigue analyses. $K_t \to \infty$ when the notch tip radius $\rho \to 0$, but often this does not imply that $S'_L \approx 0$ so instead it is often used the fatigue stress concentration factor $K_f = \frac{S_L}{S'_L}$. In mechanical problems K_f is usually estimated using the notch sensitivity factor $0 \leq q \leq 1$:

$$q = \frac{K_f - 1}{K_t - 1} \;\Rightarrow\; K_f = 1 + q \cdot (K_t - 1) \tag{2.2.9}$$

For $q = 0$ we have $K_f = 1$ (complete insensitiveness), while $q = 1 \Rightarrow K_f = K_t$, so $K_f \leq K_t$. When $\rho \to 0$ we have that $q \to 0$ too, so that we don't have $K_f \to \infty$. This all seems empirical and indeed it is: q's laws are usually designed for a specific material after testing it with different notch tip radii. Lacking those, it is always possible to assume $K_f \approx K_t$ knowing that a conservative approximation has been taken. Finally, it is useful to clarify that the nominal stress could be calculated both as $\sigma_n = F/A_{\text{gross}}$ or as $\sigma_n = F/A_{\text{net}}$, where F is the force applied. In the first case, we would have $\sigma_n = \sigma_{\text{gross}}$ and K_t^{gross} while, in the second case, $\sigma_n = \sigma_{\text{net}}$ and K_t^{net} (Fig.2.4). For this reason, it is important to be aware of the method used to calculate K_t.

One also has to consider that, even in the case of uniaxial loads, the

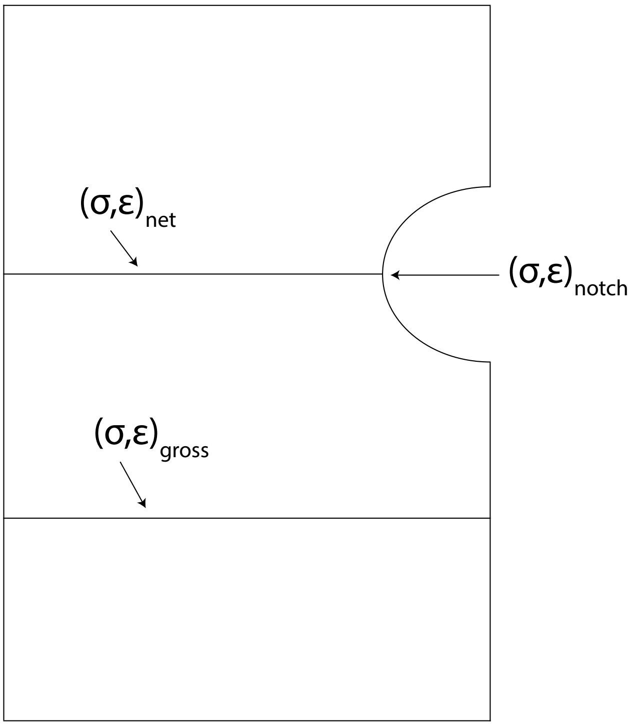

Figure 2.4: Example of the difference between net, gross, and notch tip stress and strain.

stress history at the hot spot could be multidimensional due to the geometry. However, in order to use a normal S-N curve we need a scalar factor that must account for the stress effects. When the load history is proportional (i.e. when the directions and the ratios of the principal stresses remain constant) we can use Tresca or Mises criteria:

$$\sigma_{\text{ Tresca}} = max(|\sigma_1 - \sigma_3|, |\sigma_2 - \sigma_3|, |\sigma_1 - \sigma_2|) \tag{2.2.10}$$

$$\sigma_{\text{Mises}} = \left[\frac{(\sigma_1 - \sigma_2)^2 + (\sigma_2 - \sigma_3)^2 + (\sigma_1 - \sigma_3)^2}{2} \right]^{1/2} \tag{2.2.11}$$

where $\sigma_1, \sigma_2, \sigma_3$ are the principal stresses. The idea is then to use this scalar as an equivalent stress amplitude in the S-N curve. Each nominal stress is multiplied by its fatigue concentration factor K_f (which will be different for different loading types), we then combine them in the chosen equivalent stress amplitude (e.g. Tresca's one). One last fundamental precaution that must be taken is to ensure that when there are negative (i.e. compressive) stresses, equivalent stress amplitudes which are always positive are avoided and instead other parameters, like the signed Von Mises, which can assume negative values, are used.

Mean-stress effects Even if the primary driving force in fatigue cracking is the stress range $\Delta\sigma$ (which can obviously be replaced with the stress amplitude $\sigma_a = \Delta\sigma/2$ when useful), the peak stress $\sigma_{\max}$ still plays an important role in the cracking process (e.g. by keeping microcracks opened). It is then reasonable to account for it in fatigue procedures. Usually the two parameters used in fatigue are the stress amplitude σ_a and the mean stress $\sigma_m = (\sigma_{\max} - \sigma_{\min})/2$ (sometimes the stress ratio $R = \sigma_{\min}/\sigma_{\max}$ is used instead), but it is possible to recover the peak stress from the simple relation:

$$\sigma_{\max} = \sigma_m + \sigma_a, \tag{2.2.12}$$

both the physical effects of $\Delta\sigma$ and $\sigma_{\max}$ are in this way included. As a general rule, tensile mean stress is detrimental to fatigue life, while compressive mean is beneficial. This is due to the fact that, while tensile stress helps to keep the crack opened, the compressive stress tries to close it inducing attrition between the faces which hinders the crack's propagation. In order to use the classic S-N curves which are given for $\sigma_m = 0$, engineers use the Haigh (or Goodman) diagram (see Fig.2.5). In the plot, we have the mean stress on the x-axis while the fatigue strength, expressed as stress amplitude, is on the y-axis. If N is fixed and combinations (σ_m, σ_a) are taken, it is possible to obtain a scattered curve of points with the same fatigue life. So let's say that we have point $1 \rightarrow (\sigma_m^1, \sigma_a^1)$ and point $2 \rightarrow (\sigma_m^2, \sigma_a^2)$, we could use one combination or the other and it would not change the result. Since zero mean stresses are needed, we just have to follow the curve up to its intersect with the y-axis where we will find an equivalent alternate stress $\sigma_{a_{eq}}$ which will give the same fatigue damage as our combination of σ_a and σ_m. There are many empirical curves that try to fit the data, but we can note that all of them intersect the same point in the y-axis. This is because for each curve, each point corresponds to a combination (σ_m, σ_a) which defines a cycle that the component can only endure N times. However, the fatigue strength for N cycles at zero mean stress is given by the S-N curve and so it must be the same for every curve.

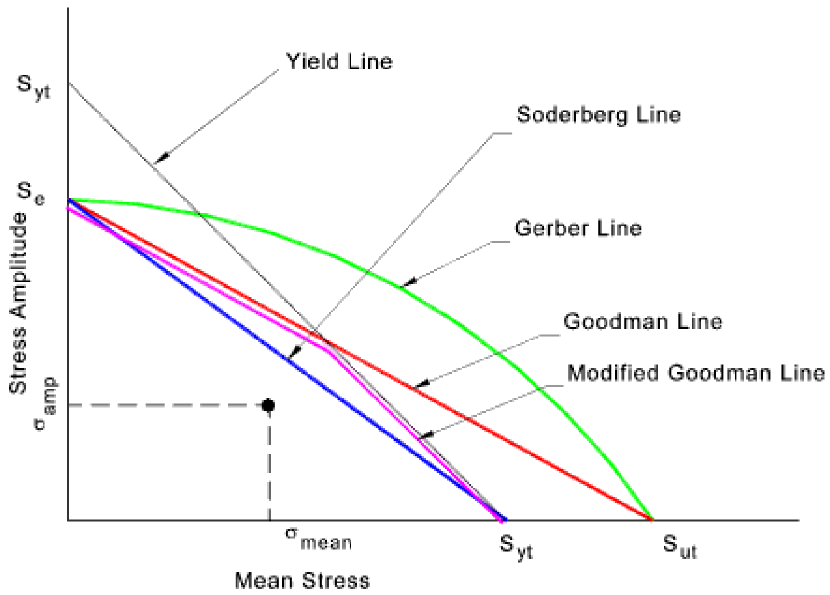

Figure 2.5: Example of Haigh diagram with various empirical curves (Picture by www.roymech.co.uk).

For $\sigma_m \geq 0$, the most used $\sigma_a \sigma_m$ rules are [1]

$$\text{Goodman: } \frac{\sigma_a}{S_F(N)} + \frac{\sigma_m}{S_U} = 1 \tag{2.2.13}$$

$$\text{Gerber: } \frac{\sigma_a}{S_F(N)} + \left(\frac{\sigma_m}{S_U}\right)^2 = 1 \tag{2.2.14}$$

$$\text{Soderberg: } \frac{\sigma_a}{S_F(N)} + \frac{\sigma_m}{S_Y} = 1 \tag{2.2.15}$$

$$\text{Marin: } \left[\frac{\sigma_a}{S_F(N)}\right]^r + \left[\frac{\sigma_m}{S_m}\right]^s = 1 \tag{2.2.16}$$

where S_Y is the yield strength and S_m is the resistance to the mean load (e.g. $S_m = S_Y$ or $S_m = S_U$). The Marin rule is a generalization of the other three since it is possible to obtain them by choosing appropriate r, s and S_m. For the case of compressive mean stress $\sigma_m \leq 0$, a Goodman-like law could be used:

$$\frac{\sigma_a}{S_F(N)} + \gamma \cdot \frac{\sigma_m}{S_U} = 1 \tag{2.2.17}$$

where $0 \leq \gamma \leq 1$ is a fitting parameter. A more complex fitting curve is:

$$\left[\frac{\sigma_a}{S_F(N)}\right]^k - \gamma \cdot \left[\frac{|\sigma_m|}{S_m}\right]^q = 1 \tag{2.2.18}$$

which is not always better since more parameters must be estimated.

Accumulated fatigue's damage

Until now we have only dealt with constant amplitude loads, but in real-life problems, stress histories are not that simple. We need to somehow sum the damage accumulated by each cycle in order to understand when failure will occur. The damage parameter D is usually taken such that $0 \leq D \leq 1$. For $D = 0$ no damage is dealt, while $D = 1$ means failure occurs. In fatigue theory, the damage D_i of a cycle with (σ_m^i, σ_a^i) is given by:

$$D_i = \frac{1}{N_i} \tag{2.2.19}$$

where N_i is the number of cycles to failure under a stress history only composed by (σ_m^i, σ_a^i) stress cycles. Now, let's say that we have n_i cycles of that kind, we will linearly interpolate the damage from the starting point $(1, 1/N_i)$ to the ending point $(N_i, 1)$ obtaining a damage $D_{n_i} = n_i/N_i$. This is obviously an assumption which tells us that the order of the cycles is not important and that they are independent since the j^{th} cycle will deal the same damage on the structure as the first, but nothing prohibits us from using another law. If, for example, we would like to assign more damage to the latest cycles and less to the earliest ones (because maybe we have some data which tell us that) we could use a quadratic law. Nonetheless the linear rule is simple and effective, while more complex rules need more data to work (e.g. to assign a quadratic function we need three points which could be $(0,0),(1,1/N_i),(N_i,1)$, and it could still make sense since for zero cycles we have zero damage, but the farther we go the more difficult it is to find sensible points): as always more complex models seem cooler but they are more difficult to calibrate. It is now possible to generalize this rule into the linear damage accumulation rule (also known as Palmgren-Miner rule). The total damage is then calculated as:

$$D = \sum_i D_i = \sum_i \frac{n_i}{N_i} \tag{2.2.20}$$

There is still one big problem: in everyday life, it's rare to have well-delineated cycles because they often overlap. Let's, for example, look at the load history in Fig.2.6. It is a simple load history and it's even periodic but we can't distinguish simple cycles of the form "$\sigma_1, \sigma_2, \sigma_1$" that we need in order to use the Miner rule and the Wöler curve. We would like to have a load history like that in Fig.2.7 but with the same damage as the first one: a possible solution is to use the rainflow counting method.

This method was developed by Matsuishi and Endo in 1968 and is an effective way of counting the events of variable (uniaxial) load histories [19, 20, 1]. It consists of three steps:

1) Assign a number to each peak and valley starting from 0.

2) Sequentially count the loading history's events until you find either:

   (a) an equal or higher peak (an equal or lower valley) than the initial point;

   (b) a previously started counting sequence; or

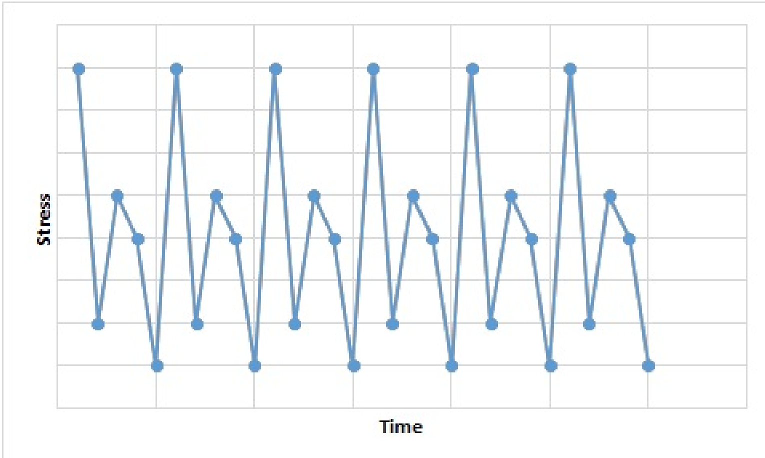

Figure 2.6: Simple periodic load history in the time domain (picture by En jen eer - Own work, CC BY-SA 3.0, wikipedia).

(c) the end of the load history.

3) Count 1/2 cycle for each i^{th} sequence founded in this way and assign to it the alternate and mean stresses:

$$\sigma_a^i = \frac{\sigma_{\max}^i - \sigma_{\min}^i}{2}$$

$$\sigma_m^i = \frac{\sigma_{\max}^i + \sigma_{\min}^i}{2}$$

Doing so we end up with a list of cycles and we can organize them in blocks of the same type so that from the signal in Fig.2.6 the load history in Fig.2.7 is obtained.
It is now possible to use the S-N curve and the damage rule in order to understand the damage imposed on the structure by the original load history.
Finally, I'd like to specify that the S-N method can, in general, be used only with homogeneous and isotropic materials when the stresses are elastic and the load is uniaxial (or multiaxial with proportional loading conditions).
Some authors (me included) sometimes use the high-cycle hypothesis as a substitute for the elastic's one, but they are not the same. Don't get me wrong, usually the high cycles hypothesis means that we are dealing with

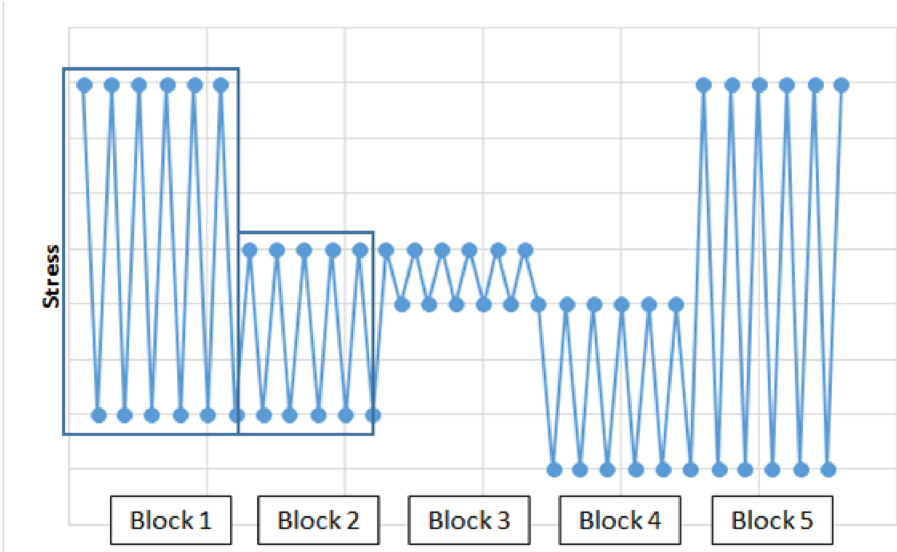

Figure 2.7: Simple periodic load history in the time domain (picture by En jen eer - Own work, CC BY-SA 3.0, wikipedia).

elastic stresses, but it's not always like that as we could have very ductile materials which endure a high number of cycles even under non-negligible yielding. That's the reason why it's not always correct to blindly use the implication:

$$\text{high-cycle} \;\Rightarrow\; \text{S-N method}$$

2.2.2 The E-N method

The E-N method (also known as the Coffin-Manson method by the authors who proposed it in independent works in 1954) or Strain-Life method recognizes the plasticity in the fatigue damage process and tries to account for it. It has been already explained how the fatigue process is characterized by the nucleation and growth of cracks and that the initiation of those is due to (at least in metallic alloys) cyclic plastic dislocations. The E-N method's most glaring difference compared to the S-N routine is the use of strain instead of stress. It's the plastic strain which drives the fatigue process and some problems could arise when using the stress in presence of yielding. In fact, if

the material does not strain-harden, we can't have stresses greater than S_Y, but the same can't be said for strains. For example, taking two specimens under tension loadings: we could induce two different plastic strains in the most critical points, but the two stresses in those hot spots would be equal $\sigma^1_{cr} = \sigma^2_{cr} = S_Y$! However, the reader will agree that different strains will induce different damages in the component.
The main assumption of the E-N model is that the fatigue damage induced on a structure is a local phenomenon that can be reproduced on a test specimen with the same properties (material and local details) and subjected to the same strain history of the critical point. The main advantages and drawbacks of the E-N routines are [2]:
Advantages:

1) they can model any crack initiation life (both low- and high-cycle);
2) they can quantify residual stresses and strains left after the unloading;
3) they consider plasticity-induced strain hardening or softening effects;
4) they use a directly measurable parameter;
5) they only require a local analysis.

Drawbacks:

1) they use non-invertible equations;
2) it's not possible to apply the superposition principle;
3) in order to consider plasticity-induced memory effects it isn't possible to rearrange the cycles in the loading history;
4) they do not model the transients from the monotonic curve to the cyclic curve;
5) they can't be used for crack growth predictions.

Hysteresis loops and Ramberg-Osgood equation

Firstly, let's introduce the notion of "true strain", which is different from "engineering strain":

$$\varepsilon_{\text{eng}} = \frac{L_f - L_0}{L_0} = \frac{L_f}{L_0} - 1 \tag{2.2.21}$$

$$\varepsilon_{\text{true}} = \int_{L_0}^{L_f} \frac{dL}{L} = ln(L_f) - ln(L_0) = ln\left(\frac{L_f}{L_0}\right) = ln(\varepsilon_{\text{eng}} + 1) \tag{2.2.22}$$

while in the elastic range we have that $L_0 \simeq L_f$ and so that $\varepsilon_{\text{eng}} \lll 1$ and $ln(\varepsilon_{\text{eng}} + 1) \simeq \varepsilon_{\text{eng}}$, this is not true for non negligible strain. So, from here on, the used notation will be $\varepsilon_{\text{true}} = \varepsilon$.

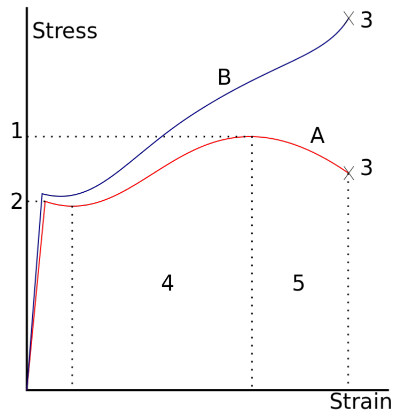

Figure 2.8: "Engineering" (red) and "true" (blue) stress–strain curve typical of structural steel. 1: Ultimate strength 2: Yield strength (yield point) 3: Rupture 4: Strain hardening region 5: Necking region (By [User:Slashme] (David Richfield) - Own work, CC BY-SA 3.0, wikipedia).

Before starting with the model, it's necessary to introduce some other basic notions of elastoplasticity. The main difference between a simple elastic model and an elastoplastic one is the fact that the strain ε can't be thought as a function of the current stress state σ alone, but, because of the memory effects of plasticity, it will be a function of the stress history as well. Plotting the σ-ε relation on the xy-plane, we will obtain hysteresis loops like the one in Fig.2.9. It is possible to see that during the loading phase $0 \rightarrow S_Y$, ε will follow the elastic rule $\varepsilon = \sigma/E$, but after that, in absence of strain hardening effects, the stress σ won't increase anymore because it can't exceed S_Y. The strain, on the other hand, will continue to grow until deloading occurs and, when $\sigma = -S_y$ is reached, the same phenomenon will happen in compression.

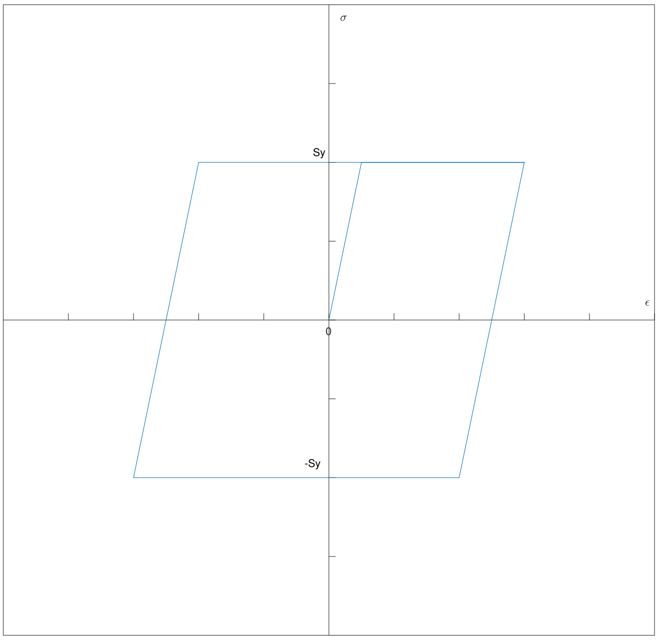

Figure 2.9: Simple simmetric hysteresis loop for non-hardening/softening materials.

More common hysteresis curves are the ones in Fig.2.10, where loops for different strain ranges, the cyclic curve, and the monotonic curve are plotted.

On the first loading event, the relation between stress and strain is described by the monotonic curve, but when there is an alternation of tension and compression, the hysteresis loops and the cyclic curve must be used instead. Whenever cyclic softening or hardening is present as well (note that these are different from their monotonic counterparts), we must "wait" until

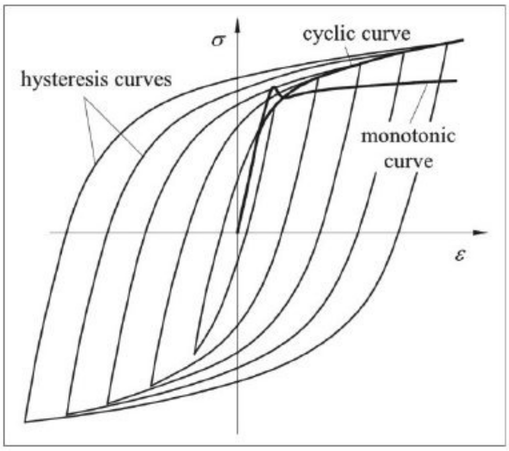

Figure 2.10: Hysteresis, monotonic and cyclic stress-strain curves (available via license: CC BY-NC-ND 4.0).

the cycles are stable before applying the cyclic curve and the hysteresis loops. The monotonic curve's law can often be modeled by the Ramberg-Osgood equation(at least for many structural alloys [2]):

$$\varepsilon = \varepsilon_{el} + \varepsilon_{pl} = \frac{\sigma}{E} + \left(\frac{\sigma}{H}\right)^{\frac{1}{h}} \tag{2.2.23}$$

where h and H are the strain-hardening exponent and coefficient. In this law, the idea is to divide the strain into the elastic and plastic part. The cyclic curve's law is usually found by fitting the tips of the stabilized hysteresis loops, as for the monotonic case, the Ramberg-Osgood equation can provide a good fitting:

$$\varepsilon = \varepsilon_{el} + \varepsilon_{pl} = \frac{\sigma}{E} + sign(\sigma) \cdot \left|\frac{\sigma}{H_c}\right|^{\frac{1}{h_c}} \tag{2.2.24}$$

where h_c and H_c are the cyclic strain-hardening exponent and coefficient, which are different from their monotonic counterparts (otherwise the equations would be the same). It should also be noted that the equation represents a symmetric cyclic behavior $\varepsilon(\sigma) = -\varepsilon(-\sigma)$, which is however, typical of many materials. Usually, the cyclic loops are described by the Ramberg-Osgood equation as well, correlating the stress amplitude $\sigma_a = \Delta\sigma/2$ with the strain amplitude $\varepsilon_a = \Delta\varepsilon/2$ [2]:

$$\varepsilon_a = \frac{\Delta\varepsilon_{el}}{2} + \frac{\Delta\varepsilon_{pl}}{2} = \frac{\sigma_a}{E} + sign(\sigma_a) \cdot \left|\frac{\sigma_a}{H_c}\right|^{\frac{1}{h_c}} = \frac{\Delta\sigma}{2E} + sign(\Delta\sigma) \cdot \left|\frac{\Delta\sigma}{2H_c}\right|^{\frac{1}{h_c}} \tag{2.2.25}$$

where H_c and h_c are the same as in the cyclic curve. Now we have to pay attention to the fact that the $\Delta\sigma\Delta\varepsilon$ loop curve is not the same as the cyclic $\sigma\varepsilon$ curve, if we rewrite (2.2.25) in terms of $\Delta\sigma$ and $\Delta\varepsilon$ we get:

$$\Delta\varepsilon = 2 \cdot \varepsilon_a = \frac{\Delta\sigma}{E} + 2 \cdot sign(\Delta\sigma) \cdot \left|\frac{\Delta\sigma}{2H_c}\right|^{\frac{1}{h_c}} \tag{2.2.26}$$

and not:

$$\Delta\varepsilon = \frac{\Delta\sigma}{E} + sign(\Delta\sigma) \cdot \left|\frac{\Delta\sigma}{H_c}\right|^{\frac{1}{h_c}} \Longleftarrow \textbf{this is wrong!!} \tag{2.2.27}$$

like what we would obtain using (2.2.24) with $\Delta\sigma$ and $\Delta\varepsilon$. In other words, the equation (2.2.25) is not linear. So:

$$\Delta\varepsilon(\sigma_a) = 2{\cdot}\varepsilon_a(\sigma_a) = 2{\cdot}\frac{\sigma_a}{E} + 2{\cdot}sign(\sigma_a){\cdot}\left|\frac{\sigma_a}{H_c}\right|^{\frac{1}{h_c}} \neq 2{\cdot}\frac{\sigma_a}{E} + sign(\sigma_a){\cdot}\left|\frac{2\cdot\sigma_a}{H_c}\right|^{\frac{1}{h_c}} = \varepsilon_a(2{\cdot}\sigma_a)\mathbf{!!} \tag{2.2.28}$$

Notch tip concentration factors and Neuber's rule

As in S-N routines, we need to account for notch's stress concentration, but even more, in this case, its effects could really be surprising: it could happen that under a nominal elastic stress history compressive yields are present. Let's take the elastic nominal history $\{0, \sigma_n, 0\}$ for an EPWH (elastoplastic without hardening) material and analyze the possibilities [2]:

1) $\sigma_n \cdot K_t < S_Y \Rightarrow$ no yielding, $\sigma_{\text{res}} = 0$.

2) $S_Y < \sigma_n \cdot K_t < 2S_Y \Rightarrow$ the specimen yields in tension but it doesn't in compression since $|\Delta\sigma| = |K_t \cdot \sigma_n| < |2S_Y|$, $\sigma_{\text{res}} = S_Y - K_t \cdot \sigma_n$.

3) $2S_Y < \sigma_n \cdot K_t$ and $\sigma_n < S_Y \Rightarrow$ the specimen yields both in tension and in compression, $\sigma_{\text{res}} = -S_Y$.

To understand it better, a good idea is to plot the stress-strain hysteresis loops of the hot spot like in Fig.2.9.
We can notice that the stress σ in the hot spot can't go beyond S_Y (for EPWH materials) so, after yielding, $K_t \cdot \sigma_n > S_Y$ while $\sigma = S_Y$. That's the reason because in general $K_t \neq K_\sigma = \sigma/\sigma_n$ and since there is plastic yielding $K_\sigma \neq K_\varepsilon = \varepsilon/\varepsilon_n$.
In 1961, Neuber discovered that the product $K_\sigma \cdot K_\varepsilon$ remains constant at notch tips in non-linear elastic prismatic bars under pure torsional loads that induce small strains [2], in these cases:

$$K_t^2 = K_\sigma \cdot K_\varepsilon = \frac{\sigma \cdot \varepsilon}{\sigma_n \cdot \varepsilon_n} \tag{2.2.29}$$

The rule is also used with cyclic loading conditions:

$$K_t^2 = \frac{\Delta\sigma \cdot \Delta\varepsilon}{\Delta\sigma_n \cdot \Delta\varepsilon_n} \tag{2.2.30}$$

as in the S-N routines, the K_t factor can be properly substituted with K_f when necessary. Since this rule was obtained with pure torsion it is valid for plain stress condition ($\sigma_z = 0$) and its reliability should be carefully verified under different assumptions. Another rule is that of Glinka, which assumes that the strain energy at the notch root is almost the same for the linear elastic case and the elasto-plastic case, as long as the surrounding zone has a linear elastic behavior [21]:

$$W_\sigma = \int_0^{\varepsilon_f} \sigma(\varepsilon)\, d\varepsilon \tag{2.2.31}$$

$$W_S = \int_0^{e_f} S(e)\, de \tag{2.2.32}$$

where W_σ and W_S are respectively the strain energy per unit volume at the notch and far from it. If we consider elastic behavior both near and far from the notch we get:

$$W_\sigma^e = \int_0^{\varepsilon_f} \sigma(\varepsilon)\, d\varepsilon = \int_0^{\varepsilon_f} E \cdot \varepsilon \, d\varepsilon = E\frac{\varepsilon_f^2}{2} = \frac{\sigma_f^2}{2E} = \frac{\sigma^2}{2E} \tag{2.2.33}$$

$$W_S = \int_0^{e_f} S(e)\, de = \int_0^{e_f} E \cdot e \, de = E\frac{e_f^2}{2} = \frac{S_f^2}{2E} = \frac{S^2}{2E} \tag{2.2.34}$$

and then:

$$\frac{W_\sigma^e}{W_S} = \frac{\sigma^2}{S^2} = K_t^2 \tag{2.2.35}$$

If the notch presents plastic yield, we can use the linear elastic rule and we have to use a new constitutive equation, e.g. the Ramberg-Osgood's one (2.2.24) and compute:

$$W_\sigma = \int_0^{\varepsilon_f} \sigma(\varepsilon)\, d\varepsilon \tag{2.2.36}$$

now, using the hypothesis:

$$K_t^2 = \frac{W_\sigma^e}{W_S} \simeq \frac{W_\sigma}{W_S} \tag{2.2.37}$$

Both Glinka and Neuber rules give only estimations of the real factors. If we want precise information, we should always perform reliable FE analysis, which can though be quite expensive.

Fatigue life and Coffin-Manson rule

We have so far analyzed the relationship between stress and strain (2.2.25) and between nominal and hot spot stresses and strains (2.2.30). What remains to be done is to establish a relationship with the fatigue life. One widely accepted method to do so is to use the Coffin-Manson rule:

$$\varepsilon_a = \frac{\Delta\varepsilon}{2} = \frac{\Delta\varepsilon_{el}}{2} + \frac{\Delta\varepsilon_{pl}}{2} = \frac{(2N)^b \cdot \sigma_c}{E} + (2N)^c \cdot \varepsilon_c \tag{2.2.38}$$

where E is the Young modulus and N is the number of cycles. Comparing (2.2.2) with this equation, we can notice some differences. It's easier and more natural to express this relation using the number of reversals $R_v = 2N$ (even if we could easily bring the 2^b and 2^c factors in σ_c and ε_c), there are more coefficients to fit (four versus two) and the law seems to be divided into two pieces: the elastic and the plastic one (similar to how Ramberg-Osgood equation is structured 2.2.24). Looking at Fig.2.11, the plastic life dominates the low cycles, while the elastic one is the most important for high cycles. Usually, the low cycles data are used to fit the plastic curve while the elastic curve should fit the high cycles data. Doing so, we get a good starting point for the resolution of the nonlinear problem for the Coffin-Manson fitting curve.

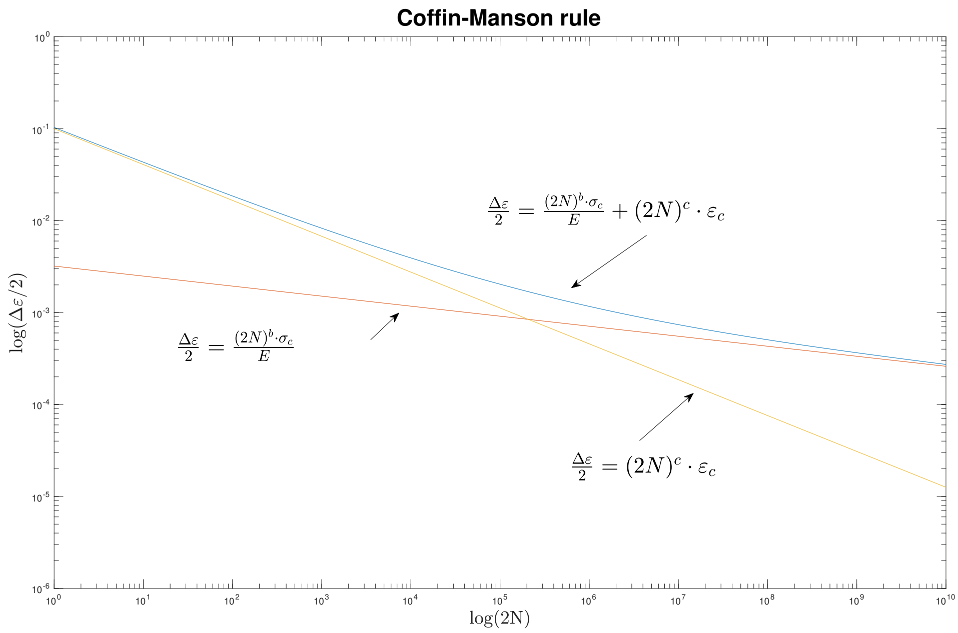

Figure 2.11: Example of a Coffin-Manson curve.

As in the S-N method, there are several ways to account for mean notch stress $\sigma_m \neq 0$:

$$\frac{\Delta\varepsilon}{2} = \frac{\sigma_c - \sigma_m}{E} \cdot (2N)^b + \varepsilon_c \cdot (2N)^c \quad \text{Morrow Elastic (ME)} \tag{2.2.39}$$

$$\frac{\Delta\varepsilon}{2} = \frac{\sigma_c - \sigma_m}{E}\cdot(2N)^b + \varepsilon_c\cdot(2N)^c\cdot\left(\frac{\sigma_c - \sigma_m}{\sigma_c}\right)^{\frac{c}{b}} \quad \text{Morrow Elastoplastic (MEP)} \tag{2.2.40}$$

$$\sigma_{\max}\cdot\frac{\Delta\varepsilon}{2} = \frac{\sigma_c^2}{E}\cdot(2N)^{2b} + \varepsilon_c\cdot\sigma_c\cdot(2N)^{b+c} \quad \text{Smith-Watson-Topper (SWT)} \tag{2.2.41}$$

these are simple corrections of (2.2.38) in order to consider σ_m's or $\sigma_{\max}$'s effects.

2.2.3 The Crack Growth method

The S-N and E-N methods are different, but neither one models the crack growth phase of fatigue life. There are, however, cases where the cracks are inevitably present and it is more productive to model their propagation and checking them periodically, instead of always replacing the cracked pieces. There are also components for which the crack growth life is longer than the crack nucleation life. An important field of application for this method can be found in the aerospace industry, but crack growth analysis is uselful whenever we approach the problem with a fail-safe or damage-tolerant design philosophy.

The Crack Growth method was first introduced by Paris, Gomez and Anderson in 1961 [3]. The innovation of this approach is to affirm that the crack growth rate $\frac{\Delta a}{\Delta N}$ (where a is the length of the crack, while N is the number of cycles) is a function of the stress intensity factor range ΔK (which is different from the stress *concentration* factor K_t). In linear elastic fracture mechanics (LEFM) K defines an approximation of the 2D stress field valid around the crack tip in the case of a homogeneous and isotropic material [3]:

$$\begin{pmatrix} \sigma_x \\ \sigma_y \\ \tau_{xy} \end{pmatrix} = \frac{K_I}{\sqrt{2\pi r}}\cdot\cos\frac{\theta}{2}\cdot\begin{pmatrix} 1 - \sin\frac{\theta}{2}\sin\frac{3\theta}{2} \\ 1 + \sin\frac{\theta}{2}\sin\frac{3\theta}{2} \\ \sin\frac{\theta}{2}\cos\frac{3\theta}{2} \end{pmatrix} \tag{2.2.42}$$

$$\begin{pmatrix} \sigma_x \\ \sigma_y \\ \tau_{xy} \end{pmatrix} = \frac{K_{II}}{\sqrt{2\pi r}} \cdot \begin{pmatrix} -\sin\frac{\theta}{2}[2+\cos\frac{\theta}{2}\cos\frac{3\theta}{2}] \\ \sin\frac{\theta}{2}\cos\frac{\theta}{2}\cos\frac{3\theta}{2} \\ \cos\frac{\theta}{2}[1-\sin\frac{\theta}{2}\sin\frac{3\theta}{2}] \end{pmatrix} \tag{2.2.43}$$

$$\begin{pmatrix} \tau_{xz} \\ \tau_{yz} \end{pmatrix} = \frac{K_{III}}{\sqrt{2\pi r}} \cdot \begin{pmatrix} -\sin\frac{\theta}{2} \\ \cos\frac{\theta}{2} \end{pmatrix} \tag{2.2.44}$$

where K_I, K_{II} and K_{III} are respectevely the stress intensity factors of the first, second and third loading mode (see Fig.2.12) and r, θ are the polar coordinates (see Fig.2.13).

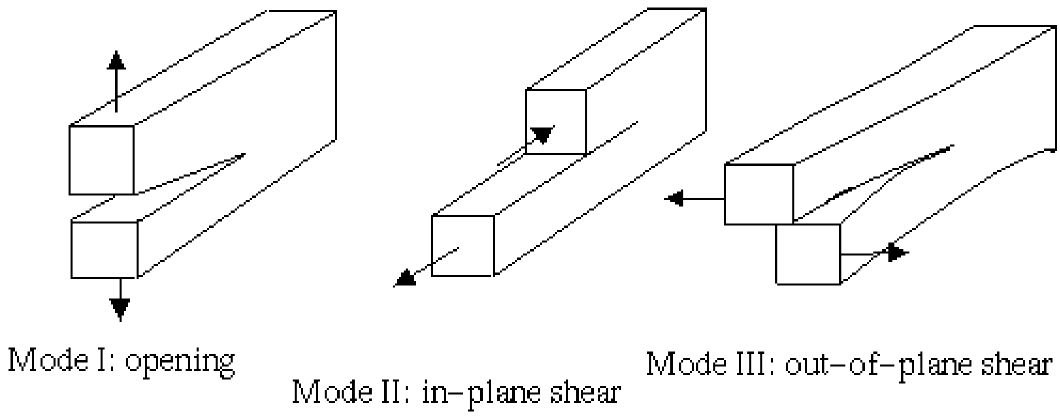

Figure 2.12: The three possible opening modes of cracks (Picture by www.lassp.cornell.edu).

However, cracks rarely grow under the second or third loading mode, so it is common to simply call $K_I = K$. We can see from (2.2.42) that K is not a dimensionless parameter, but it actually has the dimension of [stress] $\times$ [length]$^{0.5}$ (e.g. $MPa\sqrt{m}$) which sets it apart from K_t. It must also be noted that, even if at the crack tip the stress field will not be elastic, the usage of LEFM is still a good approximation when the non linear perturbation zone size pz is "small" compared to the piece and crack dimensions.
The generic form of K is:

$$K = \sigma_n\sqrt{a\pi} \cdot f(a/w) \tag{2.2.45}$$

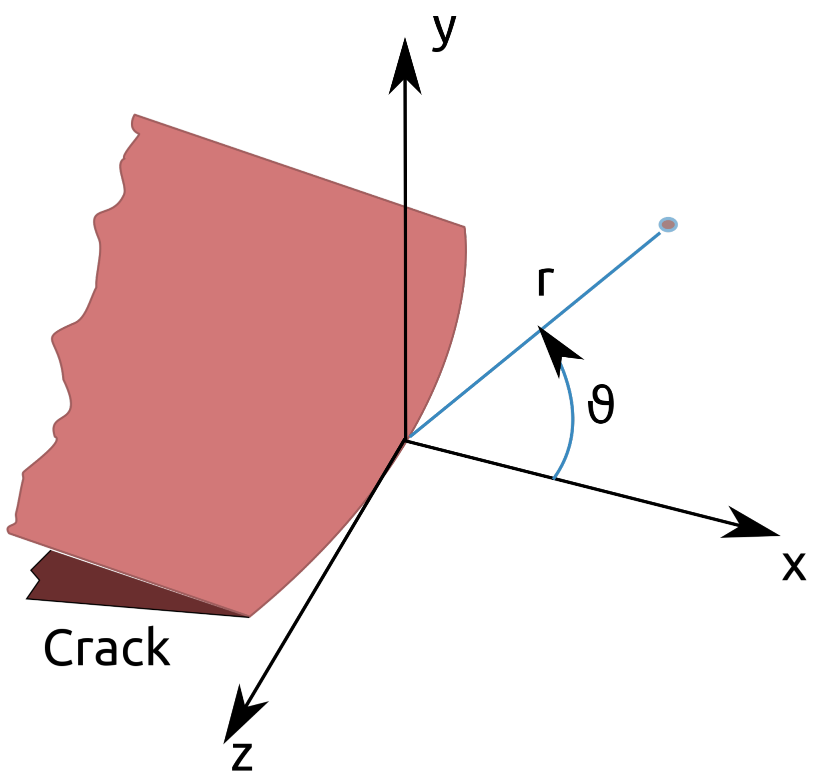

Figure 2.13: Crack tip coordinate system (By Bbanerje - Own work, CC BY-SA 3.0, wikipedia).

where σ_n is the nominal stress, a is the crack length, w is the dimension of the specimen in the direction of crack propagation (the width) and $f(a/w)$ is a dimensionless function that accounts for the geometry. Since in fatigue analysis ranges are of extreme importance, we need to define $\Delta K = K_{\max} - K_{\min} = \Delta\sigma_n\sqrt{a\pi} \cdot f(a/w)$. Looking at the crack growth rate plot in Fig.2.14, we can see that it is divided in three phases as illustrated in Fig.2.15. In the first phase, the reader can observe that there aren't any points with $\Delta K < \Delta K_{th}(R)$ $(R = K_{\min}/K_{\max})$. This shows that cracks won't grow if ΔK is smaller than the crack growth threshold ΔK_{th}. From the first phase, the slope decreases until it reaches the second phase where it remains constant. The second phase ends when the slope starts to grow again, while the third phase finishes when the peak of the stress intensity factor reaches the material toughness K_c:

$$K_c = K_{\max} = \Delta K/(1 - R). \tag{2.2.46}$$

Paris and Erdogan proposed a law for the second phase:

$$\frac{da}{dN} = A\Delta K^m \tag{2.2.47}$$

where A and m are material properties to be fitted for each individual stress intensity ratio R (taking the derivative with respect to N makes no sense from a mathematical perspective, see the appendix for a more in-depth discussion). Paris law is represented by a line with constant slope in the log-log plot of $da/dN \times \Delta K$ and can be used to estimate the fatigue life of a component if we know the crack initial size a_0 and the crack critical size a_c at which failure occurs. Integrating (2.2.47) we obtain:

$$\frac{da}{dN} = A\Delta K^m \to a(N') = a_0 + \int_0^{N'} A\Delta K^m dN \tag{2.2.48}$$

for example if we suppose that ΔK is costant (with respect to N):

$$a(N') = a_0 + \int_0^{N'} A\Delta K^m dN = a_0 + A\Delta K^m \cdot N' \tag{2.2.49}$$

This method is very simple but has one big problem: we need to know the length and direction of the initial crack a_0 and this is not an easy task in general (while the final length a_c is probably easier to estimate).
The crack growth rate can depend on the R-ratio since mean tensile stresses tend to open cracks, while mean compressive stresses tend to close them. Since Paris law does not consider the R-ratio, a modification has been proposed by Forman (1964):

$$\frac{da}{dN} = \frac{A\Delta K^m}{(1 - R)K_c - \Delta K} \tag{2.2.50}$$

where K_c is the fracture toughness and A and m are constants to be fitted. In the years, more models were proposed by different authors, but the common feature of them all was the idea of accounting for all the different R-ratios with one curve.

One last interesting feature of K is the possibility of getting an estimation of the plastic zone size around the crack tip. In fact, if we impose $S_Y = \sigma_y(x = 0)$ in (2.2.42) in the monotonic case:

$$S_Y = \max_\theta \sigma_y(\theta) = \sigma_y(\theta = 0) = \frac{K}{\sqrt{2\pi \cdot r_{pz}}} \Rightarrow r_{pz} = \frac{K^2}{2\pi S_Y^2} \tag{2.2.51}$$

while for the cyclic case:

$$2S_{Y_c} = \Delta\sigma_y(\theta = 0) = \frac{\Delta K}{\sqrt{2\pi \cdot r_{pz_c}}} \Rightarrow r_{pz_c} = \frac{K^2}{2\pi \cdot 4S_Y^2} \tag{2.2.52}$$

this estimation is important to understand if the LEFM hypothesis of small plastic zone is verified or not.

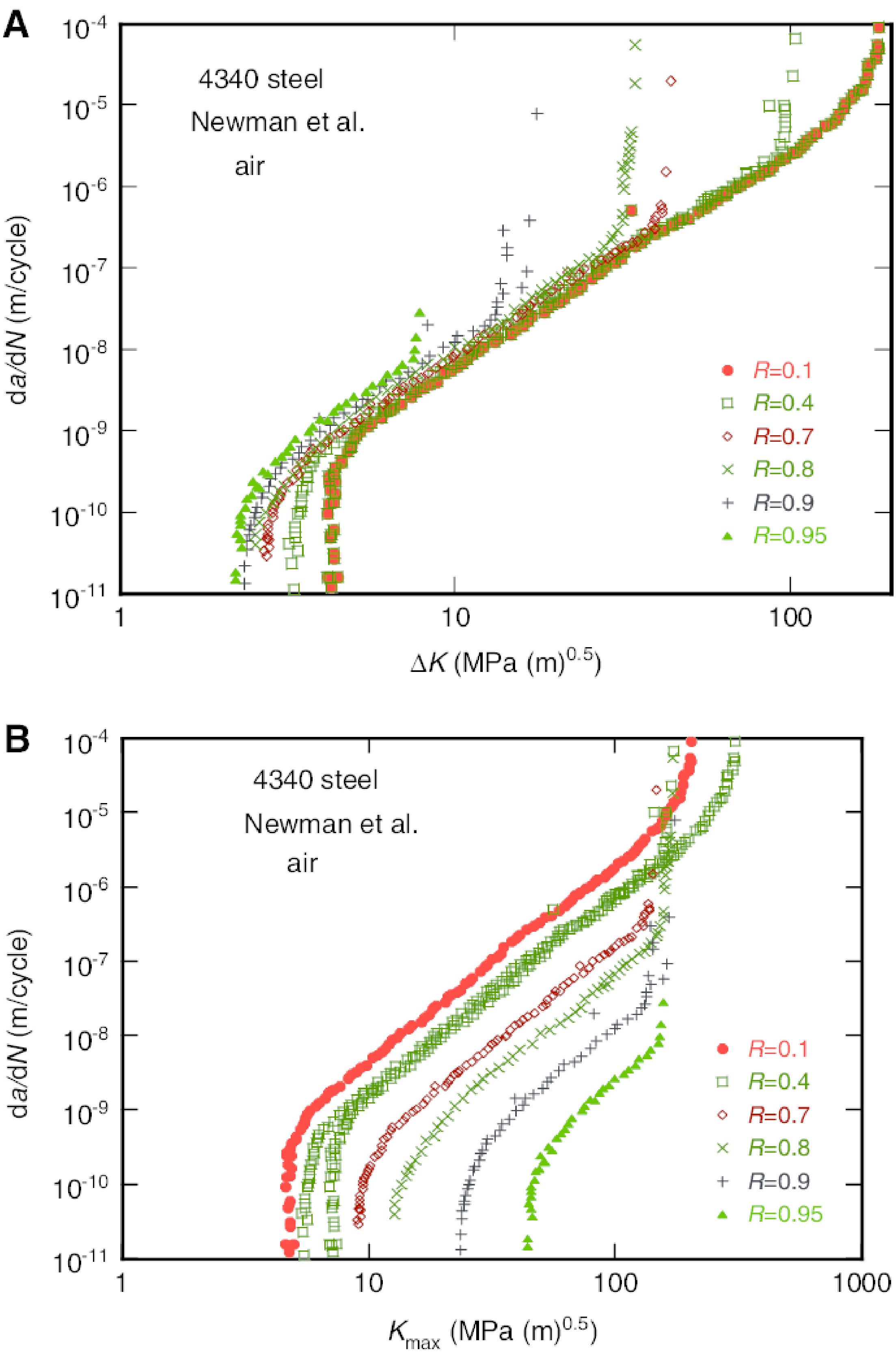

Figure 2.14: Example of crack's growth-rate tests' results [22].

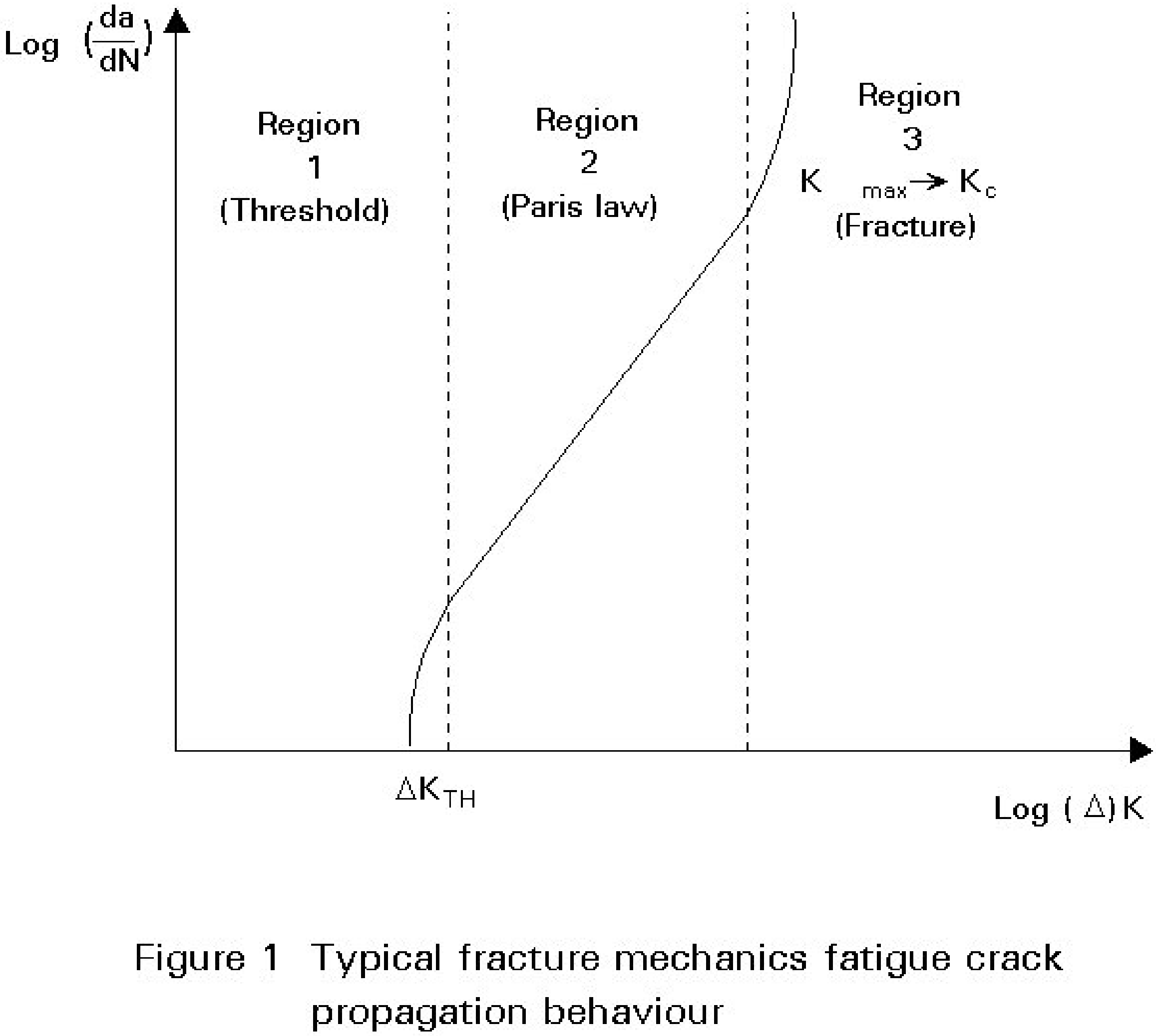

Figure 2.15: Typical crack growth rate behavior `http://fgg-web.fgg.uni-lj.si/~/pmoze/esdep/master/wg12/l1300.htm`.

Chapter 3

Welds

In this chapter welding processes and weld types will be presented in the first section while, in the second section, the main approaches to fatigue analysis of welds are illustrated.

Welding has been known since the Bronze Age, but it was only used by blacksmiths. Only at the end of the 19^{th} century, the actual methods of welding started to be discovered. Welding is "a joining process producing coalescence of materials by heating them to the welding temperature, with or without the application of pressure" ... "or by the application of pressure alone, and with or without the use of filler metal" [23]. Welding is vastly utilized in the metal industry and has applications in many fields.
Figures 3.1, 3.2, and 3.3 illustrate the different components of a weld. The position and geometry of the weld may change but the face, the root, the toes, and the legs are usually present. Two important parts of the parent material after welding are the fusion and the heat-affected zone. As the names say, the first is the part melted by the welding process while the second, even if not melted, has had its microscopic properties changed by the welding process.

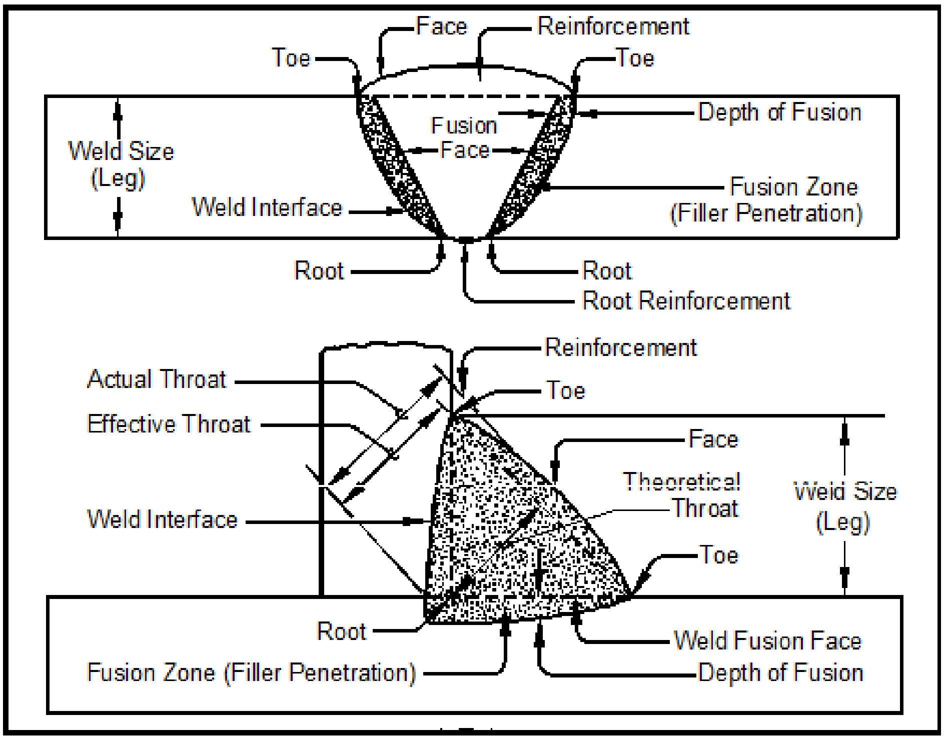

Figure 3.1: Description of the parts of a butt and a fillet weld (Picture by http://www.metalartspress.com).

3.1 A closer look at welds

Besides the materials, there are a lot of other differences among welds. The welding process and the weld type are two of the parameters which contribute to this variability.

3.1.1 Welding process

Looking at the different welding processes, it is possible to find a lot of different welding methodologies as Fig.3.4 shows. These are divided into two main categories: fusion welding and solid state welding. The first one requires the fusion of the base material, while in the solid state welding the temperature is always below the melting point of the base material.

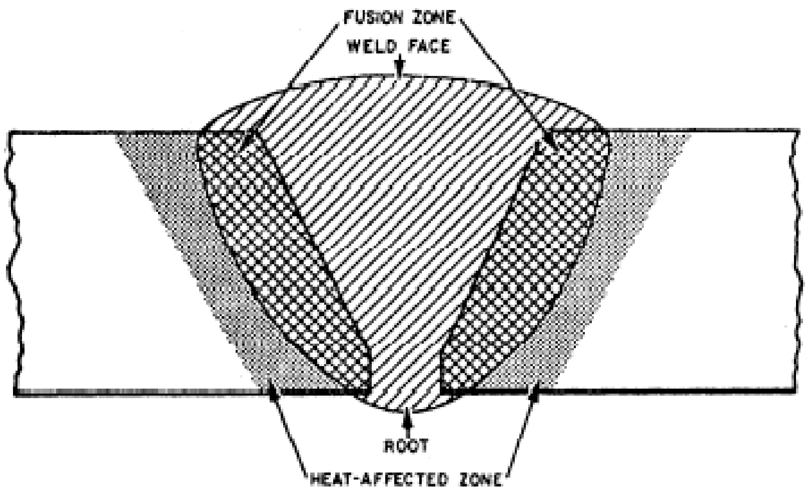

Figure 3.2: Heat-affected and fusion zone of a butt weld (Picture by https://waybuilder.net).

Fusion welding

The three main types of fusion welding are arc welding, gas welding and resistance welding (Fig.3.5).

In the arc welding process, the necessary heat is produced by an electric arc between the electrode and the working material. The arc can also supply the filler material. The welding area is usually protected from external contamination thanks to a shielding gas. There are many types of arc welding methods depending on the usage of a consumable electrode or not and depending on the type of shielding. Some notable examples are shielded arc welding (Fig.3.6), gas metal arc welding (metal inert gas (MIG) or metal active gas (MAG)) and gas tungsten arc welding.

In the gas welding process, the flame is generated by the combustion of fuel gas in an oxidizing gas (Fig.3.7). The heat created this way melts the base material and, if necessary, the filler material. It is one of the oldest methods of welding and it is still used today because of its relative low-costs and simplicity. Moreover, it does not require electricity supply and the equipment is easy to transport. On the other hand, because of the less concentrated flame, the heat affected zone will be larger and the cooling process will be slower. The subtypes of this method are based on the used gas: Oxy-acetylene, Air-acetylene, and Oxy-hydrogen welding.

Resistance welding is a thermo-electric process in which the current provided by the electrode generates heat at the interface surfaces of the welding plates due to electric resistance. The plates are also pressed against each other, and that's the reason why resistance welding also falls into the category of pressure welding methods. It is a pollution free, efficient and fast method, but it's quite expensive. There are many applications of resistance welding such as spot welding and seam welding. Spot welding is used for joining thin sheets (up to 3 millimeters) with overlap joints. The two sheets are strongly clamped by two electrodes which then provide the current needed to heat the metal and create a weld nugget between the faces (Fig.3.8). Seam welding is similar to spot welding, but in this case, the electrodes are wheel-shaped and roll on the two faces creating a continuous weld or many spot welds (Fig.3.9).

Besides the principal welding processes that have been mentioned here, there are many other methods. Some of them use filler materials while others don't. The heat source also changes and so the temperature and heat zone do as well, but the common feature is that the base material always gets melted.

Solid state welding

The main difference between fusion welding and solid state welding is that, while in the first one the working temperature is higher than the melting temperature of the base material, in the second category there isn't any melting involved and no filler material is necessary. The weld formation is due to molecular diffusion, where molecules flow from high concentration regions to low concentration areas, helped by pressure and sometimes by heat. Some famous examples are ultrasonic welding, friction welding, and explosion welding (Fig.3.10).

Ultrasonic welding (Fig.3.11) uses high-frequency ultrasonic acoustic vibrations to join the workpieces held together by pressure. It can't be used to join thick components, but it's fast and does not need a way to dissipate heat. It is for example used to join copper wires to copper or aluminum lead frames.

Friction welding consists in generating heat using the friction between the two components to then join them applying pressure (Fig.3.12). It is mostly used to join round bars, but it can weld a wide variety of metals.

Explosive welding is used to join a base, thicker, plate with a flyer, thinner, plate which usually serves as a coating. The secondary plate is placed above the main one at a stand-off distance so that the two surfaces do not touch each other; the explosive is then placed in a box on the flyer plate (Fig.3.13). The explosion creates a strong pressure wave which forms the bond between the two plates. This method works with a great number of materials, but it's restricted by the simple geometry of the components.

3.1.2 Weld types

Before the welding process starts, the parts need to be arranged in the required positions. The joint is the shape which the two parts will form after being welded. There are five basic types of joints (Fig.3.14): butt joint, corner joint, tee joint, lap joint and edge joint.

- In butt joints, the two parts lay on the same plane as in Fig.3.14, picture A;
- In corner joints, the two parts form an L-shaped right angle as in Fig.3.14, picture B;
- In tee joints, the two parts form a right angle as in corner joints, but in this case, the edge of one part and the face of the other form a T as in Fig.3.14, picture C;

- In lap joints, the two parts are simply overlapped as in Fig.3.14, picture D;
- In edge joints, the two parts are parallel with each other and have at least one edge in common as in Fig.3.14, picture E.

The two parts can be grooved as well. The groove is defined by the groove angle (or by the bevel angle) and by the root opening as shown in Fig.3.15.

Following this idea, many variations can be made for each type of joint as shown in Fig.3.16, 3.17, 3.18, 3.19, and 3.20.

Depending on the application there are many weld types, but the most common ones besides spot and seam welds are groove, fillet, slot and plug welds (Fig.3.21). As the name suggests, groove welds are simply made by filling the groove between the two components; they can be adapted to a variety of butt joints (see Fig.3.22) and be made by multiple layers. Fillet welds have a triangular shaped cross section and are used in lap, tee, and corner joints (Fig.3.23). Plug welds are made by filling circular holes on the upper plate of a lap joint, while in slot welds the holes are elongated.

Another important factor in weld geometry is the penetration. Fig.3.24 shows the difference between partial and complete penetration welds for both single and double butt joints. Besides the geometry, this feature has also a big impact on the performance of the weld, since a full penetration joint will be always more resistant than a partial penetration joint and the international guidelines, such as the Eurocode [49], underline the importance of this characteristic. Finally, the welding position may also affect the resulting geometry and make the process more difficult because of gravity. Some examples of welding positions for plate and pipe welding are illustrated in Fig.3.25.

3.2 Welds in fatigue

As any structural part, welds are subjected to all the typical failure modes like yielding, buckling, creep, corrosion etc. However, it is established that weld joints are particularly vulnerable to fatigue damage, especially when high strength materials are used and consequently, the loads are increased. This happens because, while the parent material will be certainly more resistant to fatigue, the weld will not significantly improve its fatigue strength. In fact, the fatigue properties of the welded joint differ from those of the parent plate due to large and small geometric effects and important residual stresses. Moreover, welds have a smaller (or sometimes they don't have it at all) crack initiation phase. Welds could be assimilated to notches as they are geometric discontinuities which induce stress concentrations, but they are more than that. In fact, while notch specimens are "just" geometric discontinuities, welds also present small geometrical defects and micro-flaws. These places are perfect crack initiation sites and that's the reason why the crack nucleation phase is so short for weld joints. Another important factor is the presence of residual stresses due to the heat effects generated during the welding process. In an as-welded joint (one which has not been treated with stress relieving processes), high tensile residual stresses, which tend to open cracks, may be present. All these characteristics make weld joints less resistant to fatigue and more complicated to study than simple notch specimens (Fig.3.26). In general, the most recurrent crack site is the weld toe, where there is an important discontinuity due to the transition from the parent material to the weld. Another possible site for crack initiation is the weld root, especially in the case of partial penetration, but in general, it is not obvious where the crack will start and it could easily change from one specimen to the other. For all these reasons, perform fatigue analysis on welds it's not an easy task and various approaches have been developed: the nominal stress, the structural stress, the effective notch stress (the local stress/strain), and the Crack Growth method.

3.2.1 Nominal stress approach

The nominal stress approach is the more straightforward one, we just need to determine the nominal stress and look at the S-N curve for the given joint.

Even if it may appear a simple procedure, it's important to pay attention to some possible difficulties. The first is to be able to clearly define the nominal stress (as we have seen for the elastic stress concentration factor it is not always obvious 2.4) which should include macroscopic effects(e.g. variation of the section's shape far from the joint), but shouldn't consider microscopic geometric features and effects of the joint's shape. Another requirement of the method is that there shouldn't be macroscopic geometrical entities near the welded joint: our aim when calculating the nominal stress is to consider macro-geometric features, but not the weld effects and, in these cases, it would become difficult to discern between the two. Moreover, the fatigue curves present in literature must match our specimen's and weld's geometry as well as the eventual misalignments and welding defects. When calculating the nominal stress, an overall elastic behavior of the component is assumed. This is the simplest method and can give good results for simple geometries, but requires a different fatigue curve for each change in the geometry.

3.2.2 Structural stress approach

The structural stress approach, also known as "hotspot stress method", aims to improve the nominal stress method considering the geometric effects of the joint. This methodology is useful when the loads and the geometry are complicated and it is difficult to define the nominal stress in a unique manner, or when there aren't appropriate data. At the weld toe, on the plate surface, the stresses are two dimensional and the stress component normal to the weld toe σ_{xx} (see Fig.3.27) is predominantly responsible for the fatigue damage in that area. The structural hot spot stress σ_{hs} is usually calculated as the normal stress at the weld toe (which is the hot spot) without considering the nonlinear behavior of the stress due to small discontinuities in the geometry (e.g. it does not consider the toe radius). In order to do so, the stress profile is linearized and the value at the weld toe is taken. The stress profile can be determined experimentally based on surface extrapolation (Fig.3.28), or with a FEM analysis. In the last case, we can either use the stress profile on the surface or the stress profile through the thickness (3.29). Whichever the case is, the stress profile is divided into three components: the membrane stress (normal stress), the bending stress and the nonlinear stress. The idea is to use only the first two components to get an estimate of the hot spot stress disregarding the nonlinear effects produced by the local discontinuity.

In the surface stress extrapolation procedure, the reference points (usually two or three) are established and then the structural stress at the weld toe is extrapolated. The reference point closest to the weld toe must still be far enough from it so that the measured stress is not influenced by the toe's discontinuity (which is responsible for the nonlinearity in the stress profile). This is obtained at a distance of $0.4\,t$, where t is the plate thickness. On the other hand, the linearization through the thickness consists in taking the linear part of the stress profile given by the sum of the membrane and bending stress. In practice, the membrane stress σ_m is just the average of the stress, while the bending stress $\sigma_b(y)$ is linearly distributed, it is zero in the middle, and it is such that the non linear stress profile $\sigma_{nl}(y) = \sigma(y) - \sigma_m - \sigma_b(y)$ is in equilibrium. So we have to compute:

$$\sigma_m = \frac{1}{t}\int_0^t \sigma(y)dy \tag{3.2.1}$$

$$\begin{aligned} \sigma_b^{\max} &= \frac{t/2}{b \cdot t^3/12}\int_0^t \int_0^b (\sigma(y) - \sigma_m) \cdot \left(\frac{t}{2} - y\right) dzdy \\ &= \frac{6}{t^2}\int_0^t (\sigma(y) - \sigma_m) \cdot \left(\frac{t}{2} - y\right) dy \end{aligned} \tag{3.2.2}$$

$$\sigma_{nl}(y) = \sigma(y) - \sigma_m - \sigma_b(y) = \sigma(y) - \sigma_m - \left(1 - \frac{2y}{t}\right) \cdot \sigma_b^{\max} \tag{3.2.3}$$

where b is the dimension of the plate in the z direction. We obtain $\sigma_b(y)$ knowing that $\sigma_b(t/2) = 0$ and that $\sigma_b(0) = \sigma_b^{\max}$ and using the basic property $\sigma_b^{\max} = \frac{t/2}{I_z} \cdot M_z$, then we just set $\sigma_{hs} = \sigma_m + \sigma_b$. Now we can check as the non linear part is in equilibrium:

$$\begin{aligned}\int_0^t \sigma_{nl}(y)dy &= \int_0^t \sigma(y) - \sigma_m - \sigma_b(y)dy = -\int_0^t \sigma_b(y)dy \\ &= -\sigma_b^{\max} \cdot \int_0^t \left(1 - \frac{2y}{t}\right) dy = -\sigma_b^{\max} \cdot (t - t) \\ &= 0\end{aligned} \tag{3.2.4}$$

$$\begin{aligned}\int_0^t \sigma_{nl}(y) \cdot \left(\frac{t}{2} - y\right) dy &= \int_0^t (\sigma(y) - \sigma_m - \sigma_b(y)) \cdot \left(\frac{t}{2} - y\right) dy \\ &= \frac{\sigma_b^{\max} \cdot t^2}{6} - \int_0^t \sigma_b(y) \cdot \left(\frac{t}{2} - y\right) dy \\ &= \frac{\sigma_b^{\max} \cdot t^2}{6} - \sigma_b^{\max} \cdot \int_0^t \left(1 - \frac{2y}{t}\right) \cdot \left(\frac{t}{2} - y\right) dy \\ &= \frac{\sigma_b^{\max} \cdot t^2}{6} - \sigma_b^{\max} \cdot \int_0^t \left(\frac{t}{2} - 2y + \frac{2y^2}{t}\right) dy \\ &= \sigma_b^{\max} \cdot \frac{t^2}{6} - \sigma_b^{\max} \left(\frac{t^2}{2} - t^2 + \frac{2}{3} \cdot t^2\right) = \sigma_b^{\max} \cdot \left(\frac{t^2}{6} - \frac{t^2}{6}\right) \\ &= 0\end{aligned} \tag{3.2.5}$$

The idea behind this approach is to resolve the ambiguity in the definition of the nominal stress and the need for different SN curves for each change in the macroscopic geometry of the joint.

3.2.3 Effective notch stress approach

The effective notch stress method is based on the assumption that the fatigue strength of the weld can be estimated using a linear elastic analysis and fictitious weld toe/root reference radius. The basic idea is to capture all the geometric effects due to flank angles (see Fig.3.30), weld penetration, misalignment, curved shape of weld flanks, and size effects [34] thanks to the finite element analysis, and using the fictitious reference radius r_f for assessing both weld toes' and roots' notches. In fact as we have seen in (2.2.42), (2.2.43), and (2.2.44), under elastic conditions, when $r \to 0$ the stress rises as $1/\sqrt{r}$, resulting in extremely high stresses at sharp notch tips [38]. However, since the strength of the notches is not as low as it seems it should be, Neuber hypothesized the existence of some sort of microstructural support which could be taken into account averaging the stress in the direction of the crack propagation for a certain, material-dependent, length ρ. Later on, since the averaging procedure required integration, Neuber proposed to substitute that methodology with the introduction of the fictitious radius, which could be evaluated from ρ, the real notch radius r, and a support factor s (which depends on the loading mode, on the multiaxiality condition at the notch tip, and on the applied strength criterion [38]) as:

$$r_f = r + s \cdot \rho$$

Since it's not always easy to measure the real notch radius, there are some reference values in literature. For welded joints with thickness $t \geq 5$ mm, the proposed radius derived for steel is $r_{\text{ref}} = 1$ mm (it is also used for welded joints in aluminum and magnesium alloys). For thinner connections, $r_{\text{ref}} = 0.05$ mm is suggested. This method should be used only when the root and/or the toe are the crack initiation sites and the FEM analysis has to be performed in terms of maximum principal stress range [18]. Moreover, a fine three-dimensional mesh is required and all the small geometric details must be known.

3.2.4 Crack growth approach

Since the crack initiation life is short in welded joints, it is reasonable to evaluate their fatigue life with a crack growth approach. The methodology is based on LEFM and has already been described in "The Crack Growth method" section. One more thing to emphasize here is the fact that the model requires an initial and a final crack size, and the direction of crack propagation. In particular, cracks grow slower at the beginning and for this reason the initial crack size should be measured with high precision.

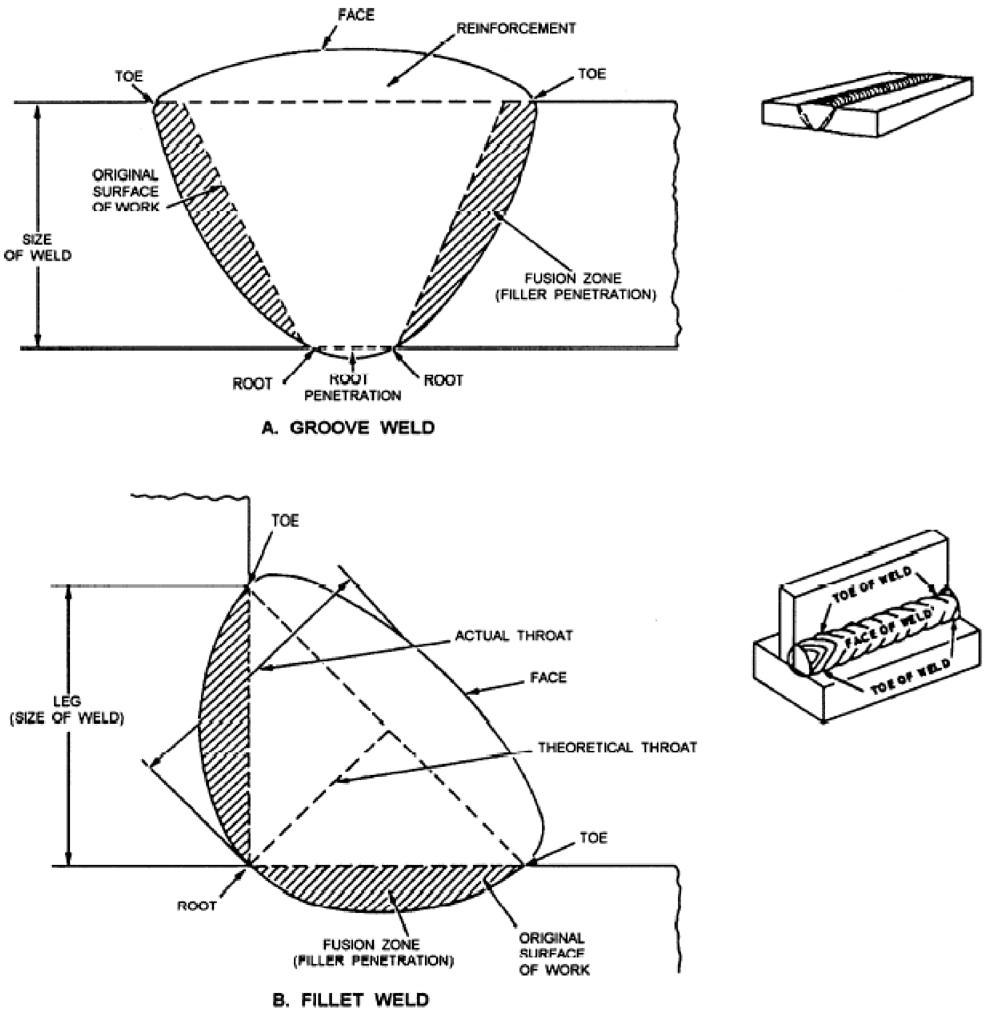

Figure 3.3: Description of the parts of a butt and a fillet weld (Picture by https://waybuilder.net).

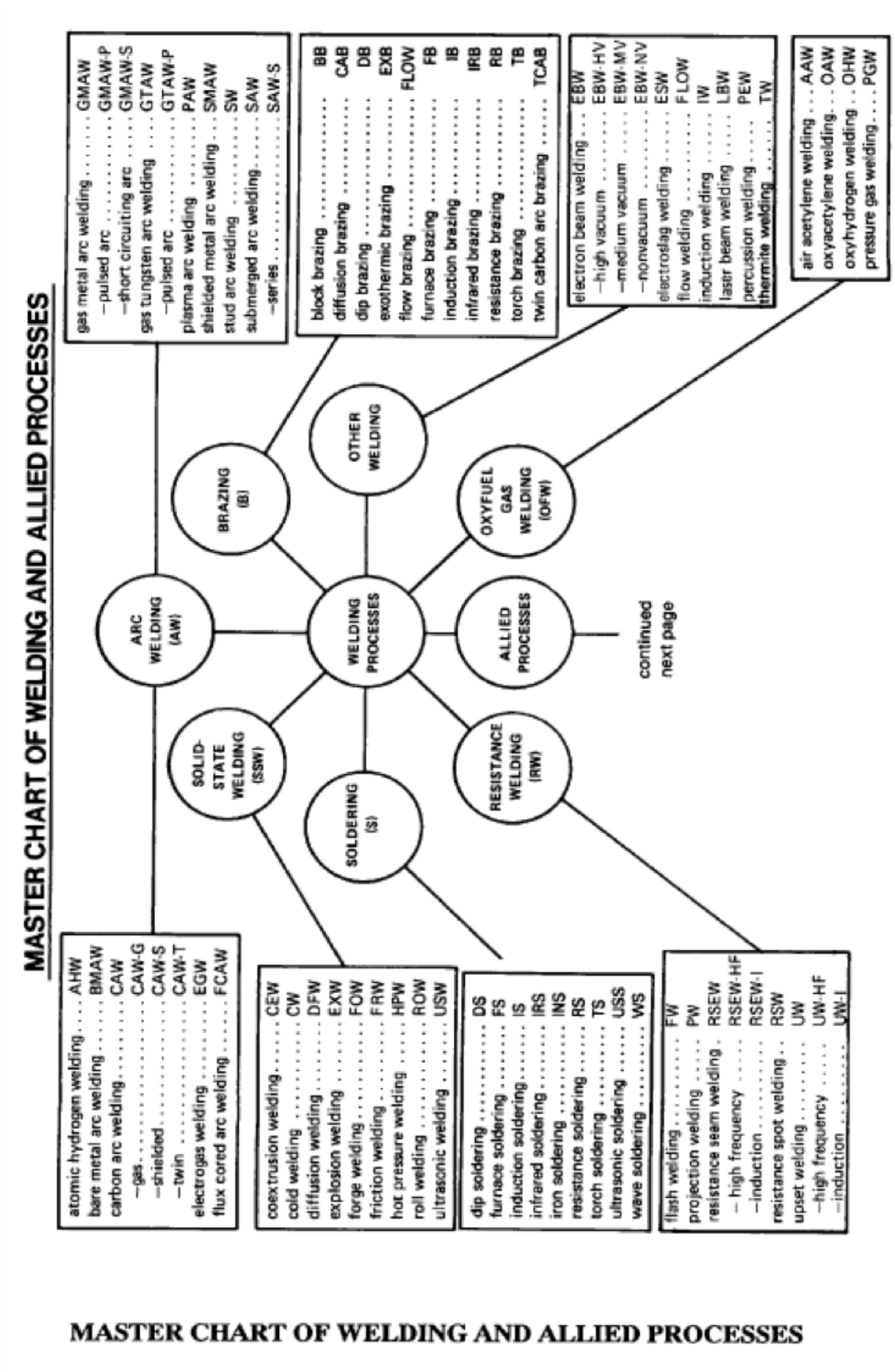

Figure 3.4: Scheme of available welding processes [32] .

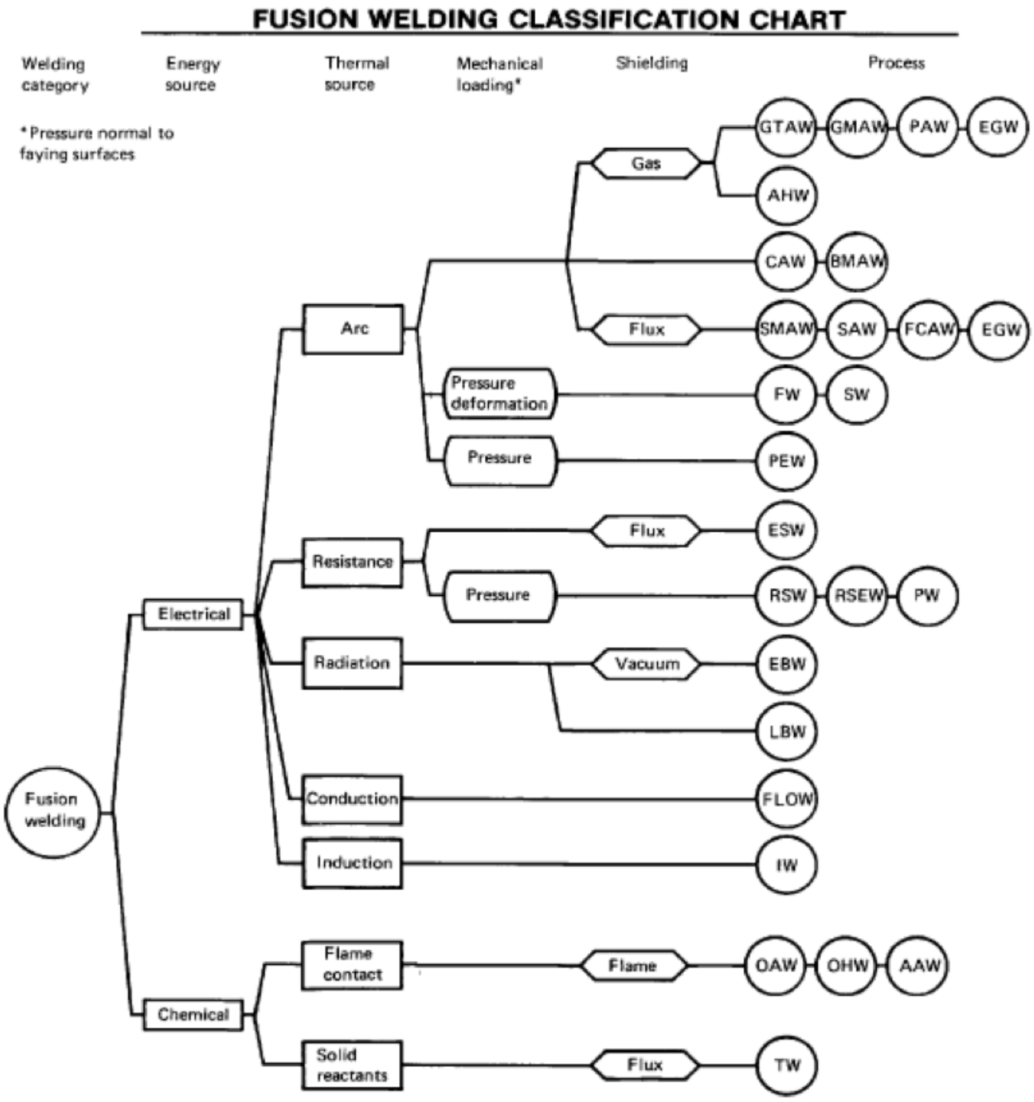

Definitions

Designation	Welding process
AAW	Air acetylene
AHW	Atomic hydrogen
BMAW	Bare metal arc
CAW	Carbon arc
EBW	Electron beam
EGW	Electrogas
ESW	Electroslag
FLOW	Flow
FCAW	Flux cored arc

Definitions

Designation	Welding process
FW	Flash
GMAW	Gas metal arc
GTAW	Gas tungsten arc
IW	Induction
LBW	Laser beam
OAW	Oxyacetylene
OHW	Oxyhydrogen
PAW	Plasma arc
PEW	Percussion

Definitions

Designation	Welding process
PW	Projection
RSEW	Resistance seam
RSW	Resistance spot
SAW	Submerged arc
SMAW	Shielded metal arc
SW	Stud arc
TW	Thermit

Figure 3.5: Scheme of fusion welding processes [32].

Figure 3.6: Shielded metal arc welding repair on a container. (By Weldscientist - Own work, CC BY-SA 4.0, wikipedia).

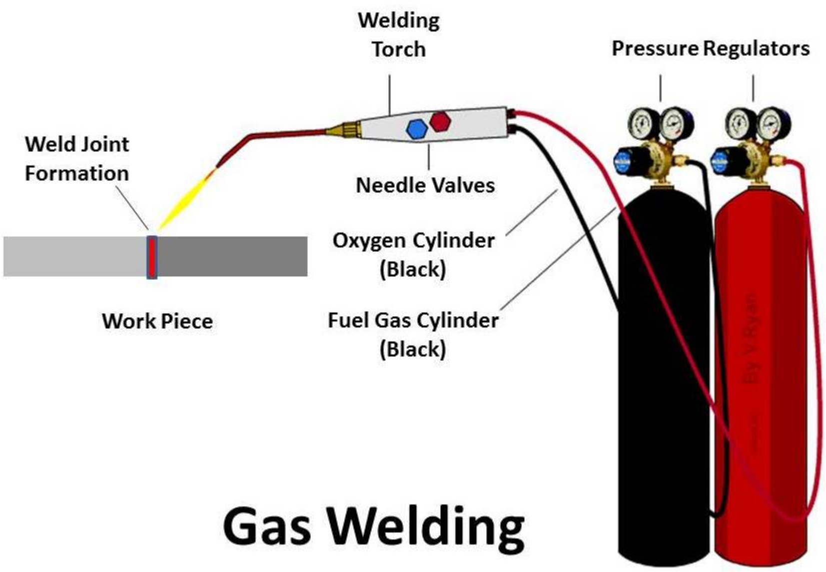

Figure 3.7: Gas welding set (Picture by http://www.mech4study.com).

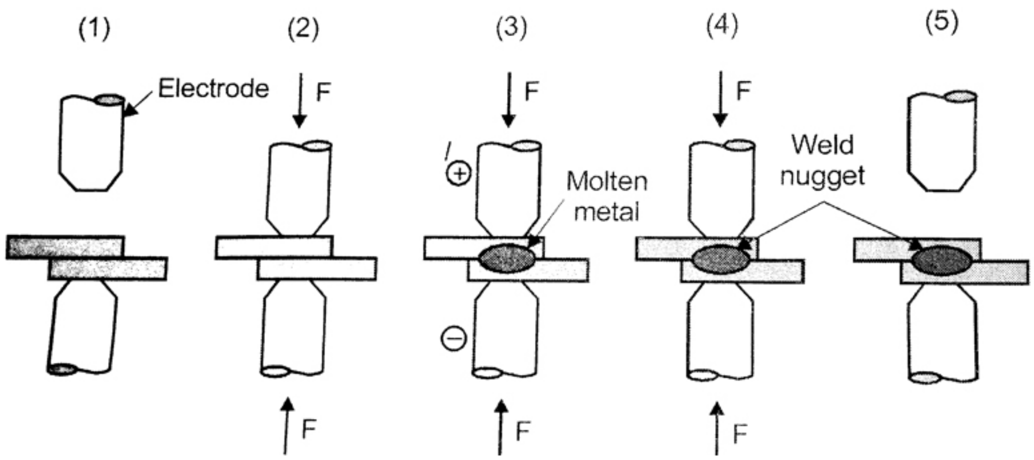

Figure 3.8: Spot weld process (Picture by http://techminy.com).

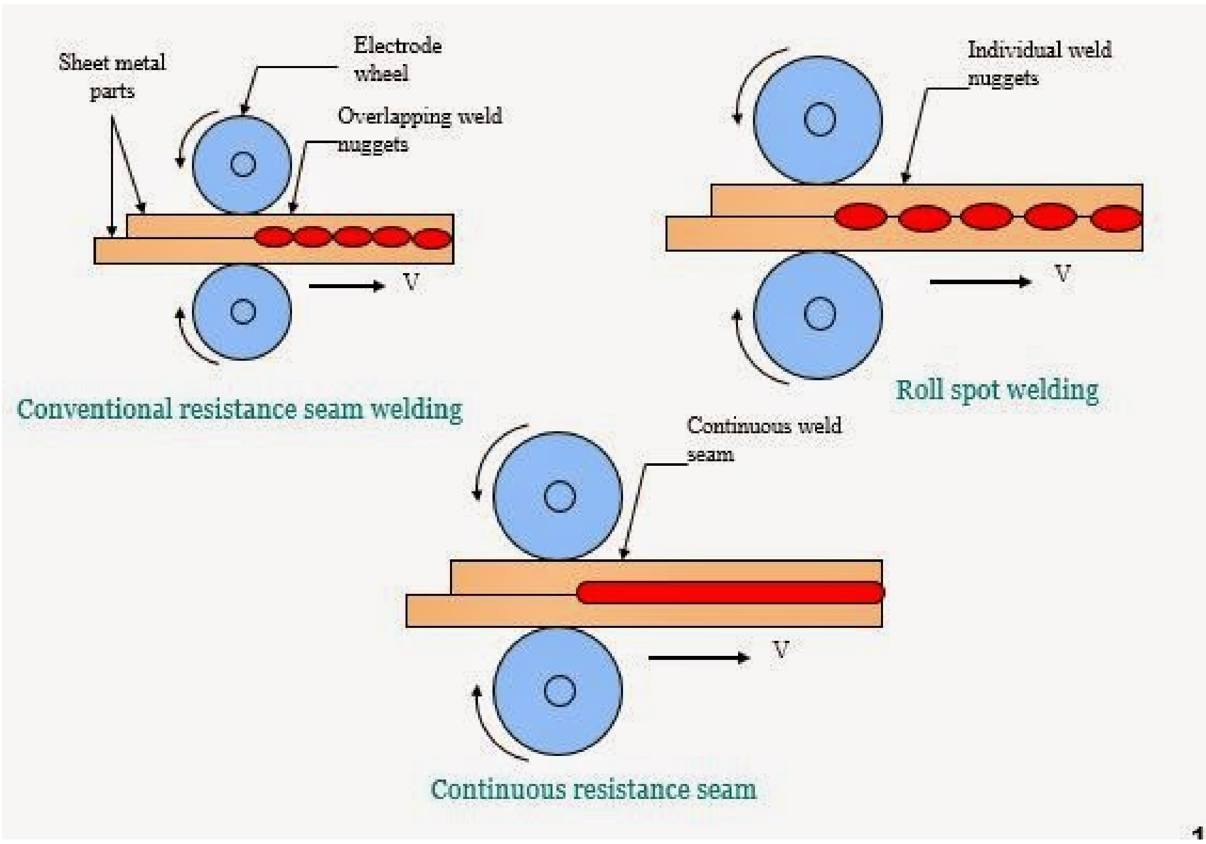

Figure 3.9: Three different types of resistance seam welding process (Picture by http://mechanicalinventions.blogspot.com).

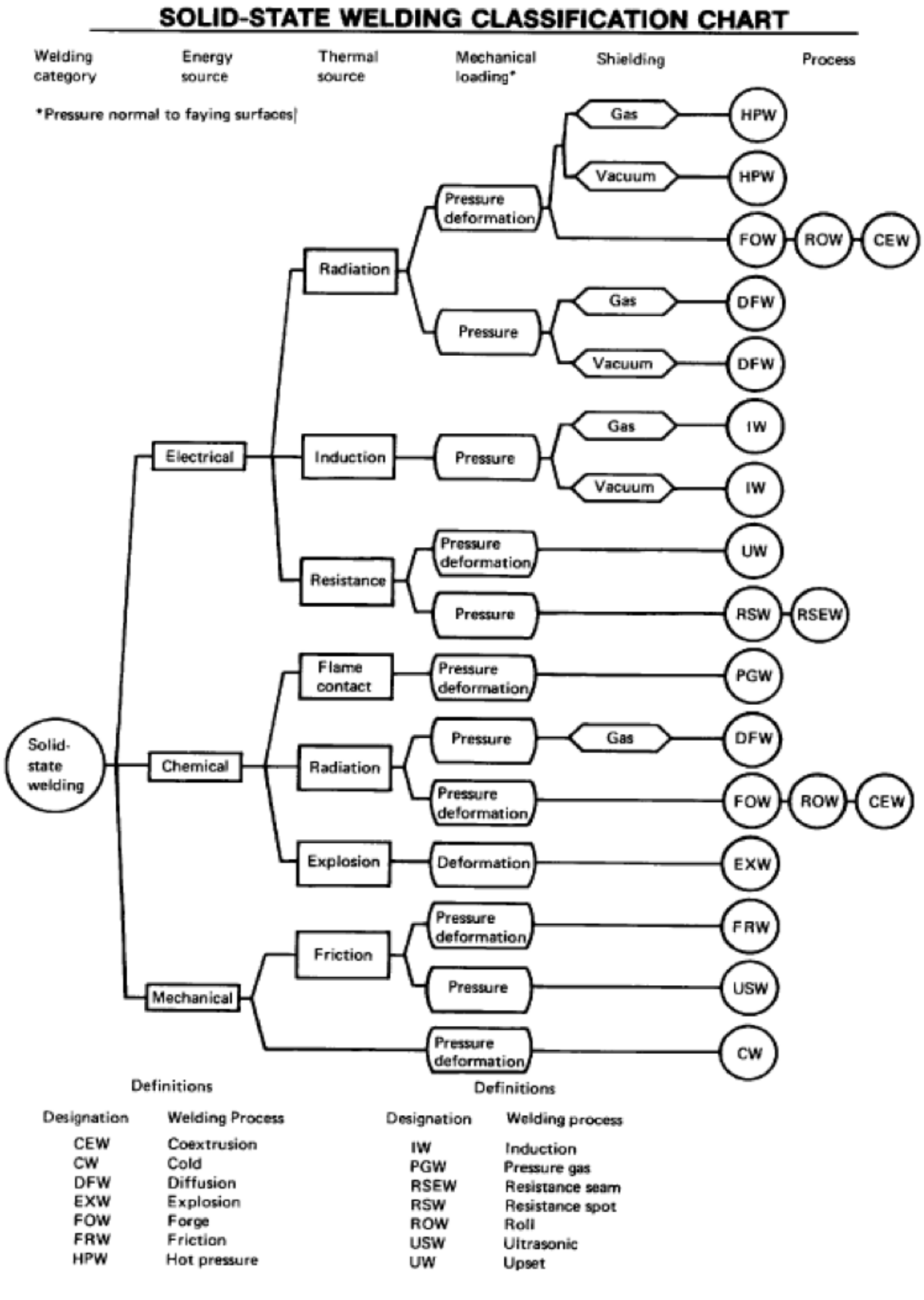

Figure 3.10: Scheme of solid state welding processes [32].

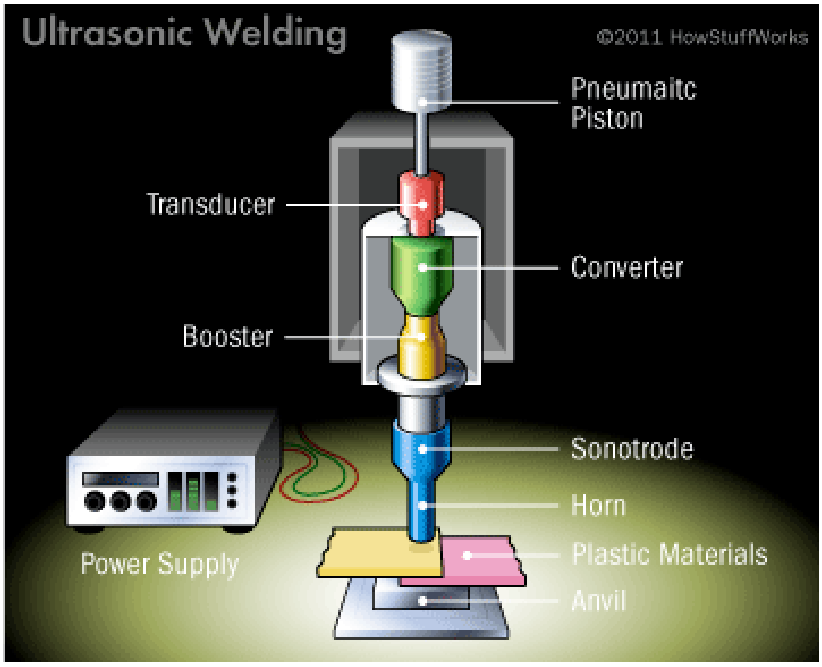

Figure 3.11: Diagram of Ultrasonic welding components (Picture by http://www.mech4study.com).

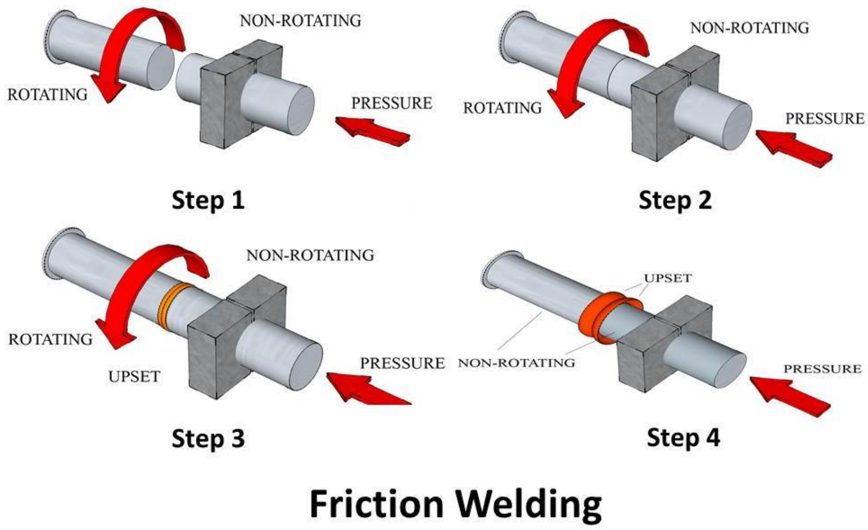

Figure 3.12: The four steps of Rotary Friction Welding (RFW) (Picture by http://www.mech4study.com).

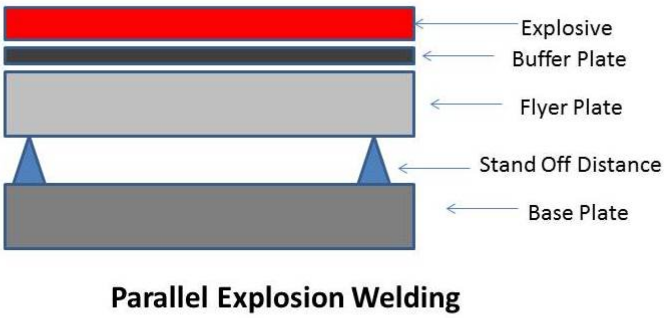

Figure 3.13: Explosive welding setup: in this case the two plates are parallel (Picture by http://www.mech4study.com).

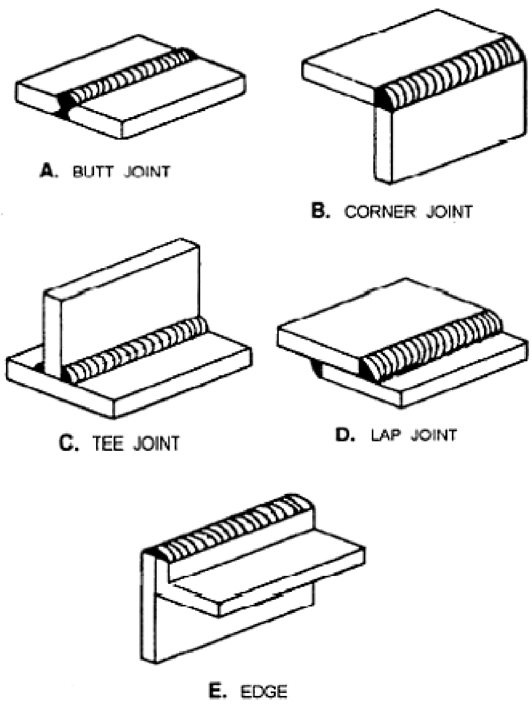

Figure 3.14: Types of welded joints (Picture by https://waybuilder.net).

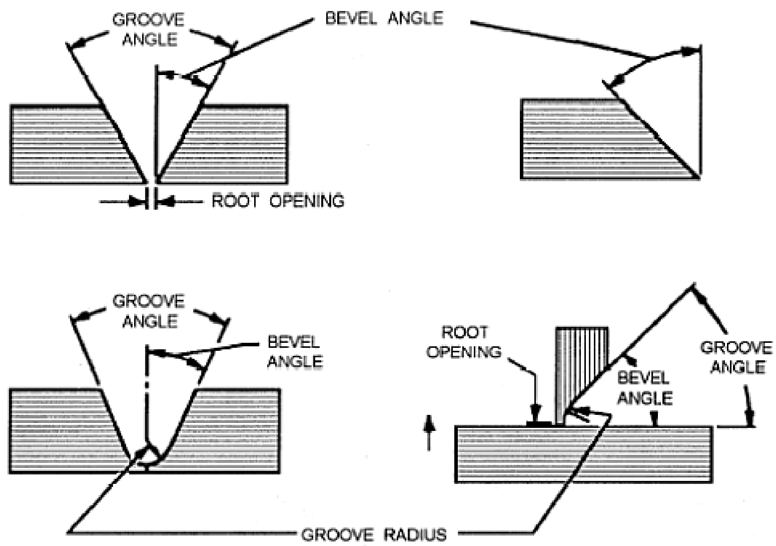

Figure 3.15: Types of welded joints (Picture by https://waybuilder.net).

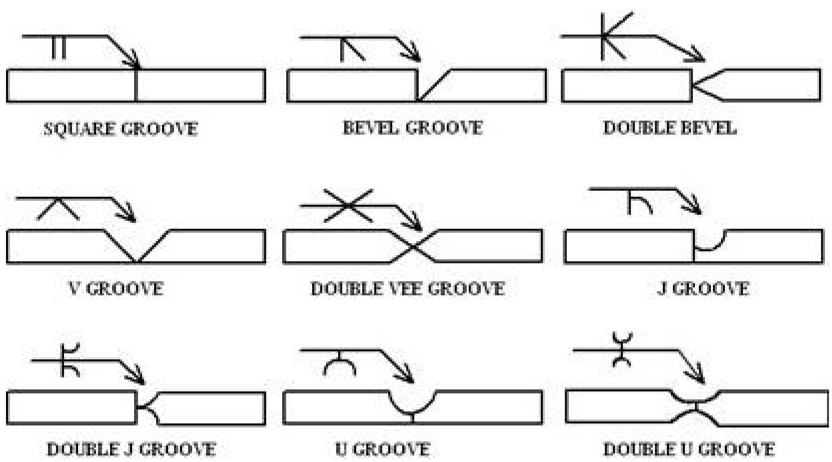

Figure 3.16: Types of butt joints (Picture by https://justinketterer.com).

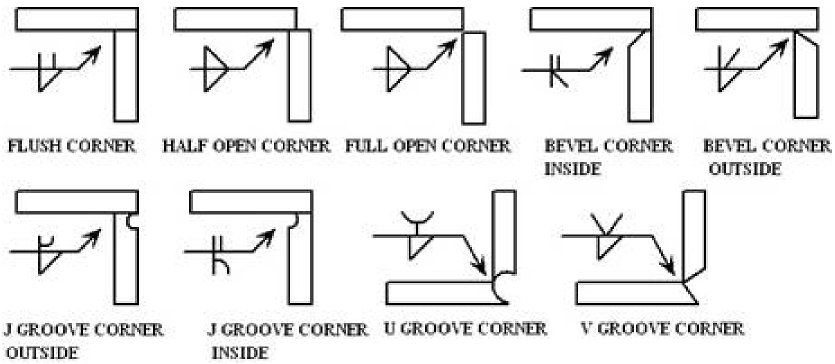

Figure 3.17: Types of corner joints (Picture by https://justinketterer.com).

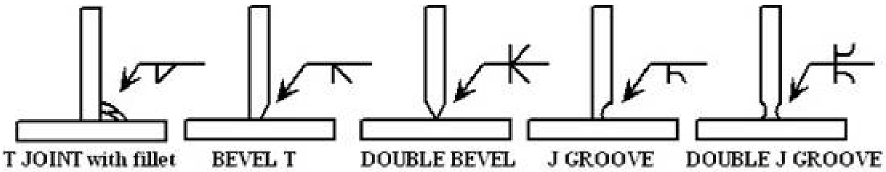

Figure 3.18: Types of tee joints (Picture by https://justinketterer.com).

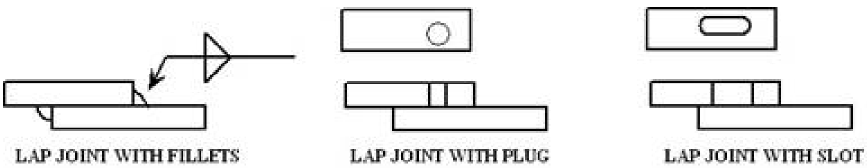

Figure 3.19: Types of lap joints (Picture by https://justinketterer.com).

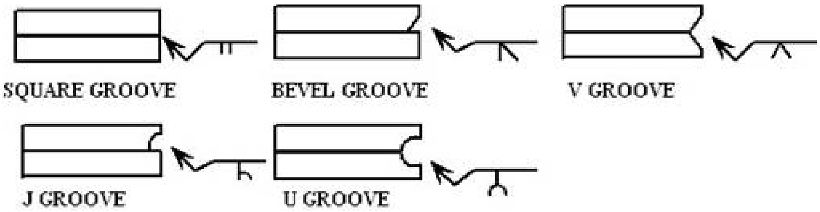

Figure 3.20: Types of edge joints (Picture by https://justinketterer.com).

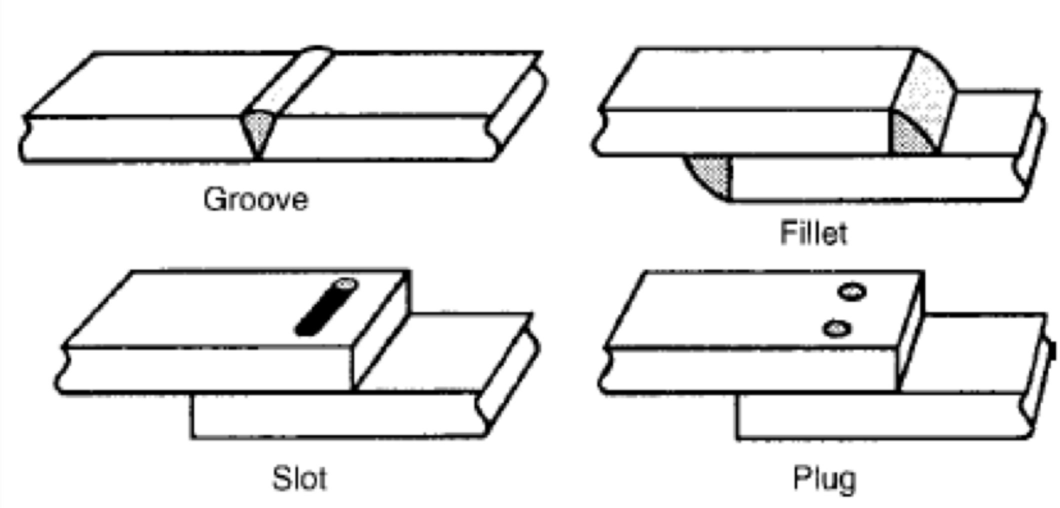

Figure 3.21: Welds' types [15].

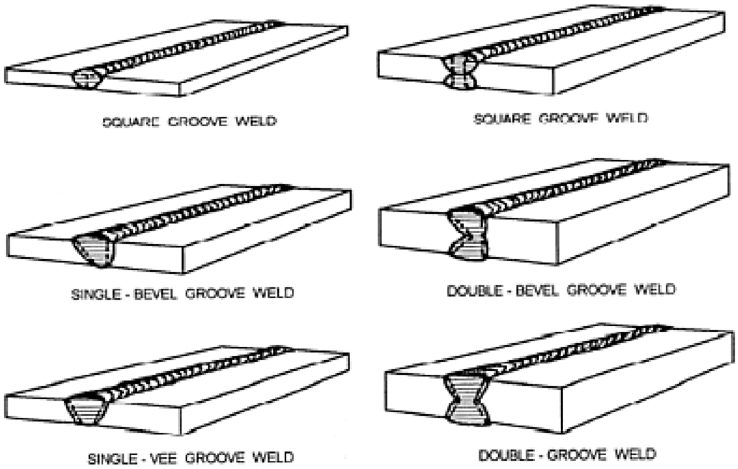

Figure 3.22: Butt joints with different groove's shapes (Picture by https://waybuilder.net).

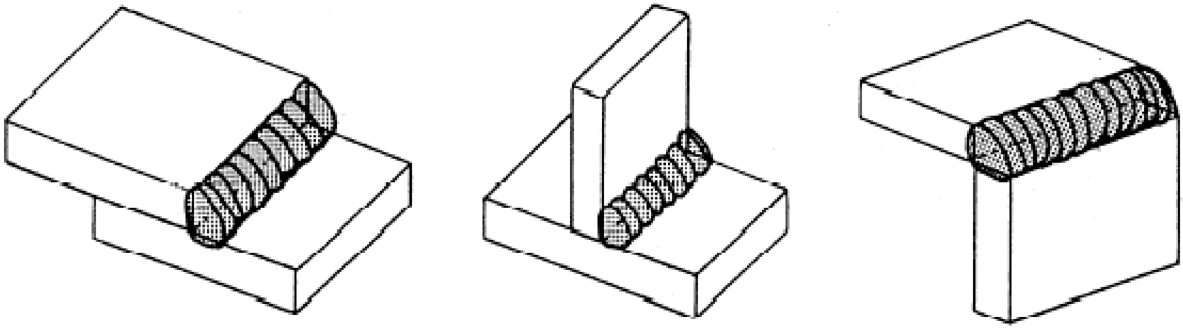

Figure 3.23: Example of fillet welds' applications (Picture by https://waybuilder.net).

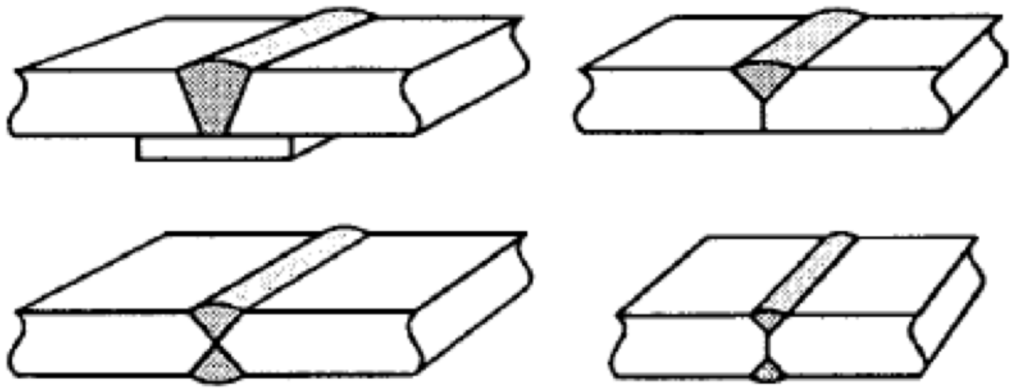

Figure 3.24: Complete vs partial penetration welds [15].

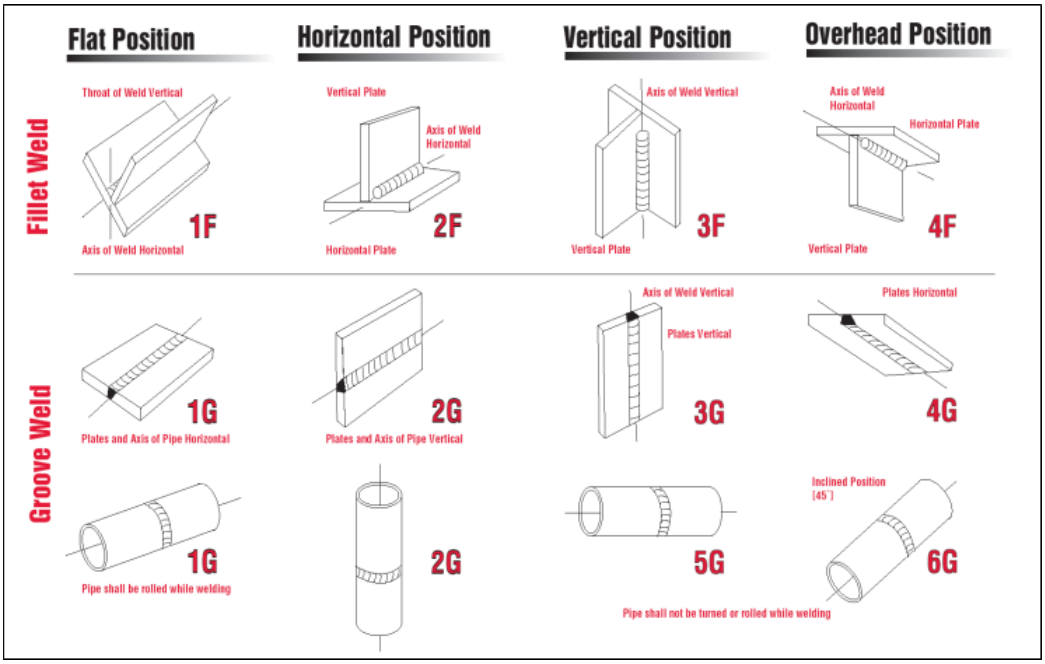

Figure 3.25: Welding positions (Picture by `https://www.pinterest.it/pin/218846863122376583/`).

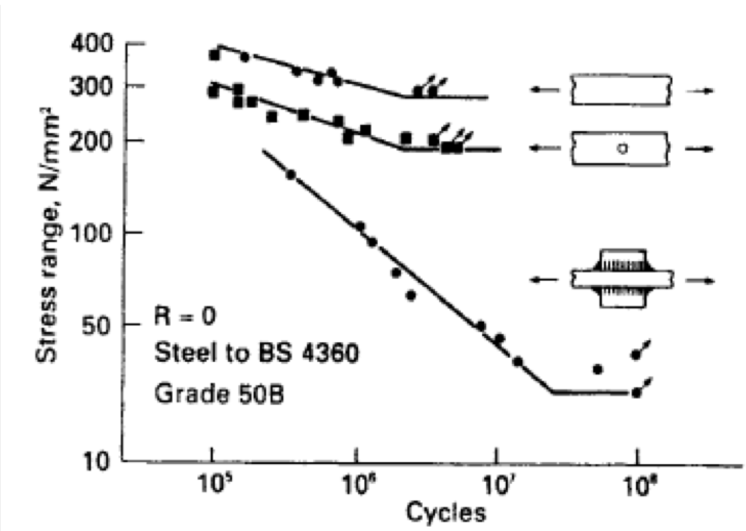

Figure 3.26: Comparison of S-N curves for integer, notched, and welded specimen [28].

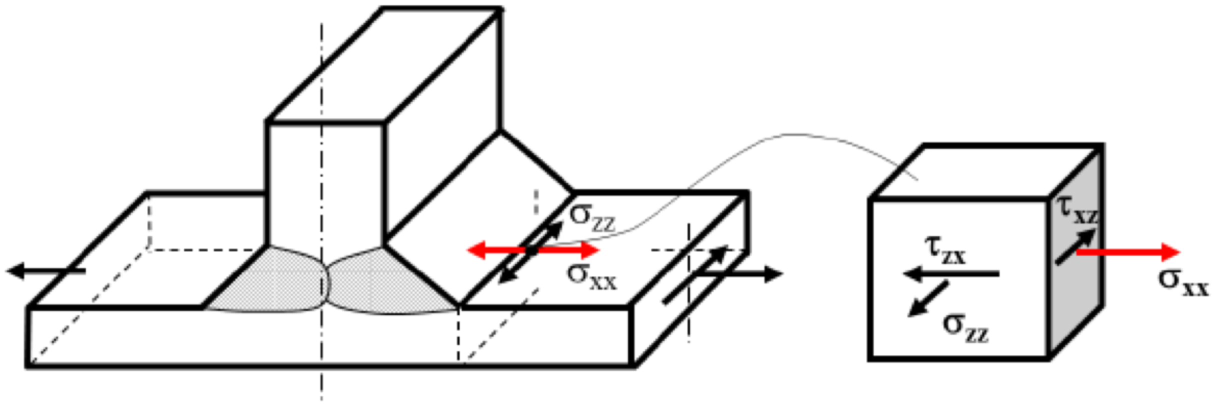

Figure 3.27: Stress state in the toe region of a welded joint [30].

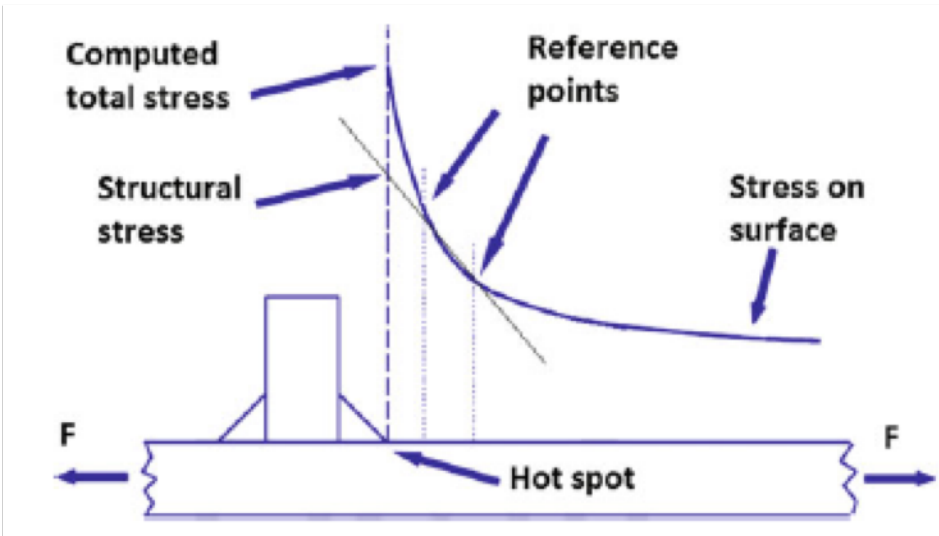

Figure 3.28: Surface stress extrapolation to determine the hot spot stess [31].

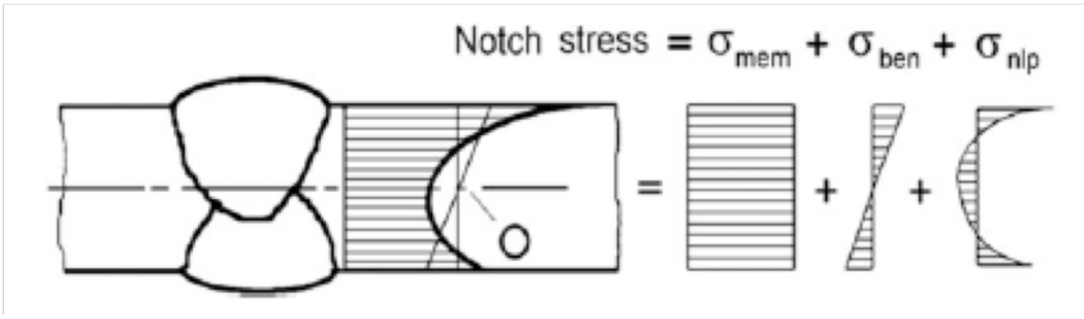

Figure 3.29: Thickness stress profile seen as sum of its three components [31].

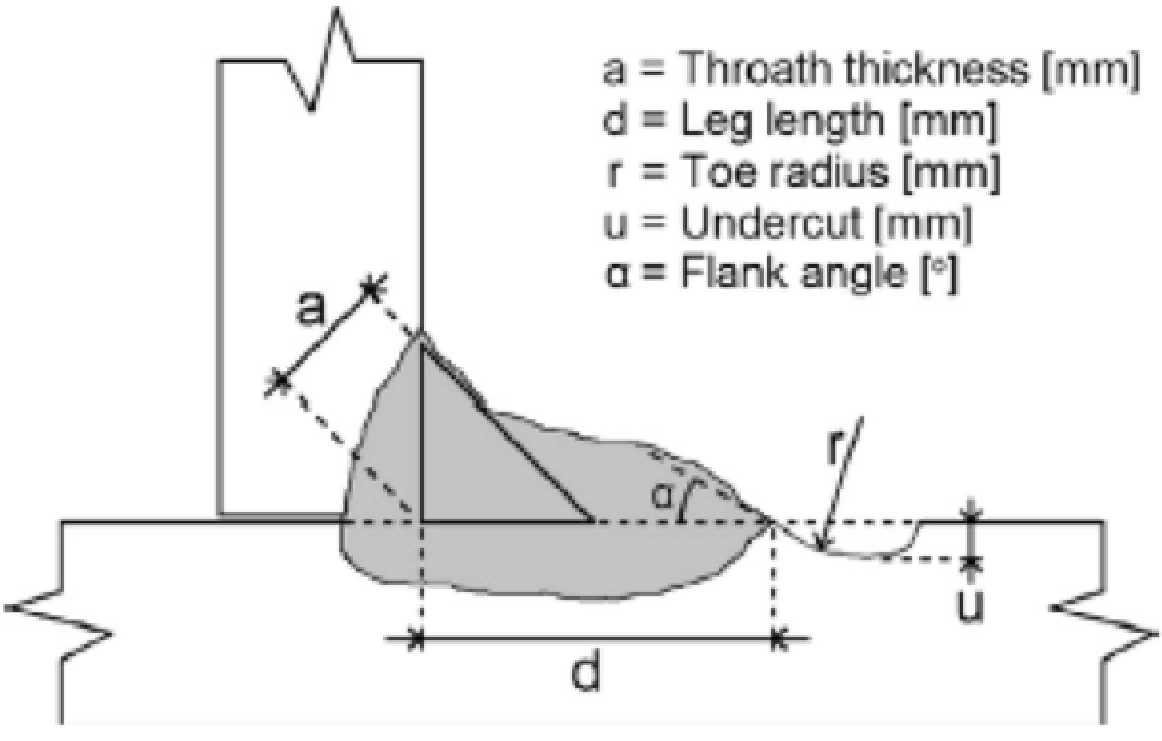

Figure 3.30: Local weld features [35].

Chapter 4

DesignLife

In this chapter, the software used for the analyses will be presented with an introduction to its methods for fatigue analysis of welds.

4.1 Presentation of the software

HBM Prenscia provides two software packages: ReliaSoft which is a union of reliability analysis and management software and nCode which includes signal processing and durability analysis software. The software suite in the nCode package is composed by Aqira, DesignLife, GlyphWorks, VibeSys, and Automation.

"Aqira is a web-based platform for creating, sharing, and running engineering apps and analysis processes", while "nCode Automation is a web-based environment for the automated storage, analysis and reporting of engineering data" [39]. VibeSys, on the other hand, provides solutions not only for vibration and acoustic analysis but also for signal processing.

GlyphWorks and DesignLife are two fatigue analysis software. The difference resides in the fact that, while DesignLife starts from an FE model, GlyphWorks is useful when tests are performed and data processing is needed. In this thesis, only DesignLife will be used.

DesignLife is a design tool for durability analysis that, starting from an FE model, identifies hotspots and calculates fatigue life. The fatigue analysis process is composed by blocks called glyphs. Glyphs are complex functions that can have one or more inputs and outputs of different kinds, so that they can be concatenated to create complete fatigue analysis from FE models and loading histories. Each glyph has one or more option panels that must be configurated properly in order to obtain sensible results. There are numerous analyses possible. Besides classical methods such as Stress-Life, Strain-Life, and Crack Growth, there are specific routines for creep, adhesive bonds, composite materials, and welds.

4.2 Fatigue analysis of welds in DesignLife

For weld analysis, DesignLife provides three glyphs: Spot Weld CAE Fatigue, Seam Weld CAE Fatigue, and WholeLife Weld CAE Analysis. The spot weld method is designed, as the name says, specifically for Spot Welds, while the Seam Weld method is used for continuous welds such as in the case of fillet and overlap joints. Finally, WholeLife combines aspects of Strain-Life analysis and fracture mechanics to perform fatigue analysis and can be used in the same cases as for the Seam Weld glyph.

4.2.1 Spot Weld

The Spot Weld analysis engine was specifically devised for the analysis of spot welds. It is based upon the work of Rupp, Störzel and Grubisic [Rupp A., Störzel K., and Grubisic V., "Computer Aided Dimensioning of Spot-Welded Automotive Structures," SAE Technical Paper 950711, 1995.] [6]. This methodology requires an FE model of the joint, as all the analysis methods in DesignLife. The spot weld can be modeled in different ways, also depending on the FE software used. One possibility is using a "bar" element connecting two sheets of shell elements to model the spot weld. The forces and moments transmitted through this bar are used to calculate stress and make fatigue life predictions. Another way to model the spot weld is to use the "Area Contact Methods", but the principle remains the same. Usually, an equivalent bar element is generated (e.g. taking the midpoint of the top and bottom faces of the hexahedral element that model the weld) and then the calculation goes on in a similar way. For more detailed explanations about the theory and usage of the Spot Weld methodology in DesignLife see the references [6] and [11].

4.2.2 Seam Weld

The Seam Weld fatigue analysis engine is the second method implemented in DesignLife for weld analysis. It is based on the structural stress approach and it may use both shell and solid FE models. One important property of this function is the SeamWeldType which separates welds in different categories. These are Fillet, Overlap, CombinedFilletOverlap, Laser Overlap, Laser Edge Overlap, Solid Weld, and Generic. The difference, besides the geometry, resides in the possible failure modes. In general, the only failure locations are the weld's toes and root, but for laser welds, the throat is a possible failure location by default too. The generic option considers all the surfaces of the shell elements attached to the weld elements as if they were weld toes. Finally, Solid Weld considers the case of a 3D solid FE model of the joint. Each weld can then be modeled in different ways, depending on the FE model. For example, a fillet weld can be represented by one or two rows of shells (see Fig.4.1 and 4.2) and an edge overlap weld in at least 3 ways depending on the number and on the placement of the shell rows (see Fig.4.3, 4.4, and 4.5)

There are three possible inputs from the 2D FE model: stresses, grid point forces and moments, and displacements.
If the stresses are directly used, for weld's toe and root elements the unaveraged nodal stresses or the average stresses at the edges' midpoints are used; while for the weld throat elements, the stresses are averaged at the centroid. A similar procedure is applied to the other two cases, the only difference is that it is necessary to first obtain the stresses from the FE inputs. When

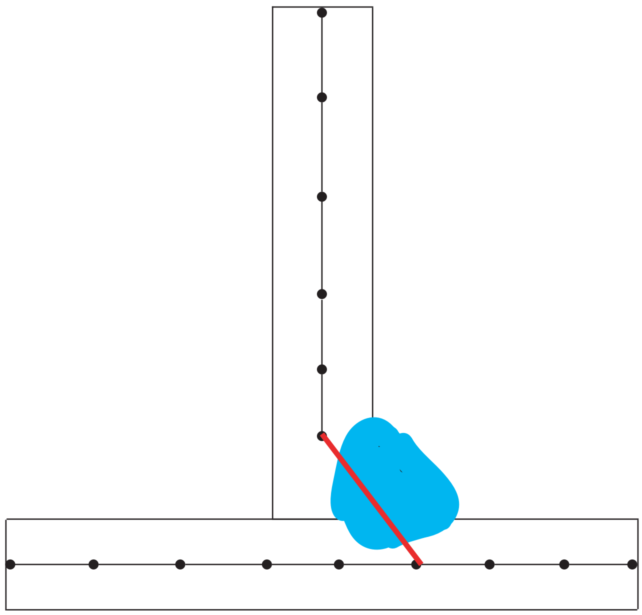

Figure 4.1: Fillet weld modeled by a single row of inclined shells.

the input are the grid point forces and moments, for each node all the components from each weld toe element are summed, for example if node 8 is shared between element 1 and 2:

$$F^8 = F_1^8 + F_2^8 \quad \text{and} \quad M^8 = M_1^8 + M_2^8$$

Then the moments and forces are redistributed between the two adiacent weld toe elements, depending on the length of their toe edge. For example if, when looking at the toe, the element 1 is on the right of the node 8:

$$F^8_{\text{right}} = F^8 \cdot \frac{l_1}{l_1 + l_2} \quad \text{and} \quad M^8_{\text{right}} = M^8 \cdot \frac{l_1}{l_1 + l_2}$$

while for element 2 we have:

$$F^8_{\text{left}} = F^8 \cdot \frac{l_2}{l_1 + l_2} \quad \text{and} \quad M^8_{\text{left}} = M^8 \cdot \frac{l_2}{l_1 + l_2}$$

then, after this procedure has been done for all the nodes of the weld toe's edges, the forces and moments at the middle of the toe's edges are calculated. For example, if the element 1 has the edge at the toe given by the segment

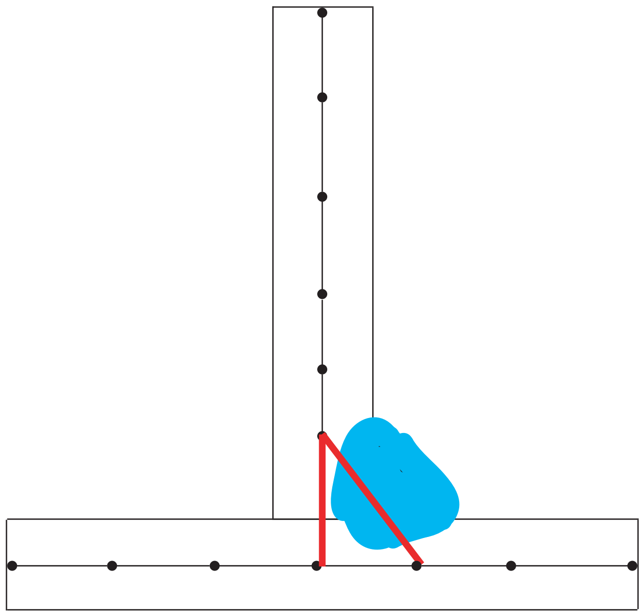

Figure 4.2: Fillet weld modeled by two rows of shells.

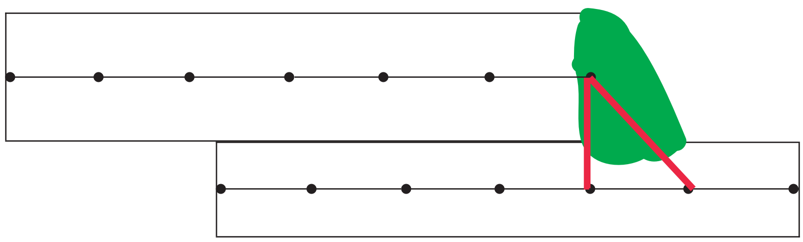

Figure 4.3: Overlap joint modeled by two rows of shells.

between node 8 and 7, with node 7 on the left of the edge when looking at the weld toe (so that the element is on the right with respect to the node 7), we have:

$$f_1 = \frac{F^7_{\text{right}} + F^8_{\text{left}}}{l_1} \quad \text{and} \quad m_1 = \frac{M^7_{\text{right}} + M^8_{\text{left}}}{l_1}$$

The forces and moments are then rewritten in a local coordinate system with z' perpendicular to the weld toe element's surface, y' parallel to the weld toe edge and x' perpendicular to the weld toe edge and to z'. Finally, the structural stress at the top and bottom of the weld are calculated as follow:

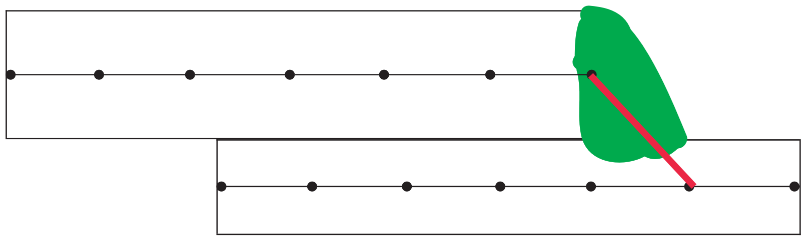

Figure 4.4: Overlap joint modeled by a single row of inclined shells.

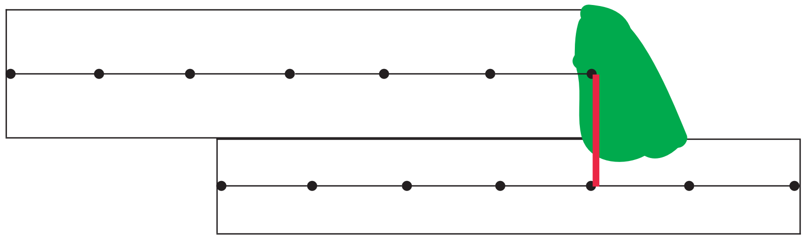

Figure 4.5: Overlap joint modeled by a single row of straight shells.

$$\sigma_{1,\text{struc,top}} = \sigma_{1,\text{membrane}} + \sigma_{1,\text{bending}} = \frac{f_1 \cdot e_{x'}}{t} + \frac{6m_1 \cdot e_{y'}}{t^2} \tag{4.2.1}$$

$$\sigma_{1,\text{struc,bot}} = \sigma_{1,\text{membrane}} - \sigma_{1,\text{bending}} = \frac{f_1 \cdot e_{x'}}{t} - 6\frac{m_1 \cdot e_{y'}}{t^2} \tag{4.2.2}$$

where t is the thickness of the weld toe element and $e_{x'}, e_{y'}, e_{z'}$ are the normalized vectors which form the canonical basis according to the local coordinate system.

When nodal displacements and rotations are used, the strain at each weld toe node is derived from the relative displacement of the other nodes of the element. For each node considered, the three directions along the segments that link it to the other three nodes of the element (quadrilateral element should be used) are analyzed separately. In each direction, the problem is reduced to a one dimensional problem and the strain along that direction is calculated, using the relative displacements and rotations. Doing this for all the three directions, leave us with three strains that can be used to obtain

the strains in the global coordinate system at the node and, from them, the stresses can be calculated following the elastic, isotropic, and homogeneous stress-strain relationship. This method is only valid for small displacements since geometry's nonlinearities are not considered. It also fails to model stress in warped elements and can present numerical issues if the displacements are too small.
In the case of solid element FE modeling, the "through the thickness" procedure explained in the structural stress section is followed. In particular, the membrane and bending stress are obtained from equations (3.2.1), (3.2.2), and (3.2.3) for each stress component σ_{ij} in the plane orthogonal to the direction of the thickness. In the algorithm, the stress tensor is interpolated from the FE results in an equidistant number of points decided by the user. The membrane and bending stresses are then calculated following the discretization of the equations (3.2.1) and (3.2.2) after a change of the coordinate system:

$$\sigma_{ij,m} = \frac{1}{n} \cdot \sum_{k=1}^{n} \sigma_{ij,k} \tag{4.2.3}$$

$$\sigma_{ij,b} = -\frac{6}{t^2} \cdot \sum_{k=1}^{n} (\sigma_{ij,k} - \sigma_{ij,b}) \cdot (k - 0.5) \cdot \left(\frac{t}{n}\right)^2 \tag{4.2.4}$$

where n is the number of the discretization points and t is the thickness. The final step is to define the top and bottom structural stresses as:

$$\sigma_{ij,\text{top}} = \sigma_{ij,m} + \sigma_{ij,b} \quad \text{and} \quad \sigma_{ij,\text{bottom}} = \sigma_{ij,m} - \sigma_{ij,b} \tag{4.2.5}$$

Once the stress tensors at the top and bottom surface are defined, their time histories and their combined stress histories are determined. The degree of bending is then calculated from the top and bottom surface stresses and the bending ratio is used to interpolate between the stiff and flexible SN curves. After the appropriate SN curve is obtained, the weld's top surface's stress history is rainflow counted and the damage calculation is carried out. The bottom surface stress is only useful to assess the need for bending correction in the SN curve. The degree of bending is determined by:

$$r = \frac{|\sigma_{eq,top} - \sigma_{eq,bot}|}{|\sigma_{eq,top} - \sigma_{eq,bot}| + |\sigma_{eq,top} + \sigma_{eq,bot}|} \tag{4.2.6}$$

where σ_{eq} is the equivalent stress. The formula is used to calculate all the useful statistics of the bending ratio in the loading history. The one which is ultimately used is the weighted average:

$$\overline{r} = \frac{\sum_{i=1}^{n} r_i \cdot \sigma^2_{eq,top,i}}{\sum_{i=1}^{n} \sigma^2_{eq,top,i}} \tag{4.2.7}$$

The interpolation factor is then determined:

$$I = \begin{cases} 0 & \text{if} \quad 0 \leq \overline{r} \leq r_{th} \\ \frac{\overline{r} - r_{th}}{1 - r_{th}} & \text{if} \quad r_{th} < \overline{r} \leq 1 \end{cases} \tag{4.2.8}$$

Finally, the SN curve is interpolated from the stiff and the bending curves using I.
For more details on the Seam Weld fatigue analysis engine see [6].

4.2.3 WholeLife

As already illustrated in previous chapters, the crack initiation and growth phases are usually studied separately and with different fatigue models, or just one of them is considered while the other is neglected. In the WholeLife routine, however, the entire life is included in a single fatigue model and in order to do so, the method integrates concepts from both the ε-N and the Crack Growth approaches. The basic idea of the method is to consider a "grain parameter" ρ^* and suppose that the material is composed of grain characterized by such dimension. The crack growth will then be seen as a sequence of crack initiations through each grain.
The WholeLife model is based on [44] and [47] which explain "The Two Parameter Total Driving Forces Model" and modify it (renaming it "The

UniGrow Model"), making it applicable to variable amplitude loading spectra. The two forces are the stress intensity factor (SIF) range ΔK and the maximum stress intensity factor $K_{\max}$. ΔK is well known for being important in the fatigue crack growth process, while $K_{\max}$ has been used widely in order to find one law for all the stress intensity ratios.

The two parameters driving force model

In the presentation, the following assumptions are made [44]:

1° The material is composed of elementary grains of the same dimension ρ^*.

2° The fatigue crack can be analyzed as a sharp notch of radius ρ^*.

3° The Ramberg-Osgood equation is used to relate stresses and strains.

4° The Coffin-Manson law with the Smith-Watson-Topper correction is used to calculate the fatigue life.

5° The fatigue crack growth rate can be calculated from the mean fatigue crack propagation rate through the single grain of size ρ^*. If N_f cycles are necessary to propagate over the elementary material block then:

$$\frac{da}{dN} = \frac{\rho^*}{N_f}. \tag{4.2.9}$$

If the crack has a tip radius ρ^*, a good approximation of the linear elastic stress when ρ^* is small in comparison to the crack size a is the Creager-Paris solution (which is based on the assumption of a type 1 crack opening mode) [5]:

$$\sigma_x(r,\theta) = \frac{K}{\sqrt{2\pi r}}\left[\cos\frac{\theta}{2}\left(1 - \sin\frac{\theta}{2}\sin\frac{3\theta}{2}\right) - \frac{\rho^*}{2r}\cos\frac{3\theta}{2}\right] \tag{4.2.10}$$

$$\sigma_y(r,\theta) = \frac{K}{\sqrt{2\pi r}}\left[\cos\frac{\theta}{2}\left(1+\sin\frac{\theta}{2}\sin\frac{3\theta}{2}\right)+\frac{\rho^*}{2r}\cos\frac{3\theta}{2}\right] \tag{4.2.11}$$

$$\sigma_{xy}(r,\theta) = \frac{K}{\sqrt{2\pi r}}\left[\cos\frac{\theta}{2}\sin\frac{\theta}{2}\sin\frac{3\theta}{2}-\frac{\rho^*}{2r}\sin\frac{3\theta}{2}\right] \tag{4.2.12}$$

if we fix $\theta = 0$, then $r = x$ and we can write:

$$\sigma_{x,\max} = \frac{K_{\max}}{\sqrt{2\pi x}}\left(1-\frac{\rho^*}{2x}\right) \quad \sigma_{y,\max} = \frac{K_{\max}}{\sqrt{2\pi x}}\left(1+\frac{\rho^*}{2x}\right) \tag{4.2.13}$$

$$\Delta\sigma_x = \frac{\Delta K}{\sqrt{2\pi x}}\left(1-\frac{\rho^*}{2x}\right) \quad \Delta\sigma_y = \frac{\Delta K}{\sqrt{2\pi x}}\left(1+\frac{\rho^*}{2x}\right) \tag{4.2.14}$$

Since a blunt crack model is used, the radius ρ^* will be finite and the crack region just behind the tip will be considered open even under compressive stress. Moreover, under compressive loads the crack is treated as a circular notch of radius ρ^* and since its concentration factor is $K_t = 3$, if linear elastic local behavior is supposed:

$$\sigma^e_{\text{min,net}} = 3S_{\text{min,appl}} \tag{4.2.15}$$

where $\sigma^e_{\text{min,net}}$ is the minimum stress in the component, while $S_{\text{min,appl}}$ is the minimum compressive nominal stress applied. From the definition of K in the second chapter (2.2.45), it is possible to write:

$$S_{\text{min,appl}} = \frac{K_{\text{min,appl}}}{Y\sqrt{\pi a}} \tag{4.2.16}$$

where Y is just $f(a/w)$.

If (4.2.15) and (4.2.16) are put together:

$$\sigma^e_{\text{min,net}} = \frac{3K_{\text{min,appl}}}{Y\sqrt{\pi a}} \tag{4.2.17}$$

On the other hand, if we use the Creager-Paris equation (4.2.13) for the minimum stress:

$$\sigma^e_{\text{min,net}} = \frac{2K_{\text{min,net}}}{\sqrt{\pi\rho^*}} \tag{4.2.18}$$

Combining (4.2.17) and (4.2.18):

$$K_{\text{min,net}} = K_{\text{min,appl}} \frac{3\sqrt{\rho^*}}{2Y\sqrt{a}} \tag{4.2.19}$$

Is now possible to obtain ΔK_{net}:

$$\Delta K_{\text{net}} = K_{\text{max,appl}} - K_{\text{min,net}} = K_{\text{max,appl}} - \frac{3\sqrt{\rho^*}}{2Y\sqrt{a}} K_{\text{min,appl}} \tag{4.2.20}$$

and then $\Delta\sigma^e_{\text{net}}$:

$$\Delta\sigma^e_{\text{net}} = \left(K_{\text{max,appl}} - \frac{3\sqrt{\rho^*}}{2Y\sqrt{a}} K_{\text{min,appl}} \right) \frac{1}{\sqrt{2\pi x}} \left(1 + \frac{\rho^*}{2x} \right) \tag{4.2.21}$$

Note again that this correction is only used when the minimum applied stress is compressive.
Another correction was later proposed in [48] to account for the different behavior of short cracks. The main problem is that, following the LEFM theory, a short crack subjected to high loads should behave like a long crack subjected to low loads would since they have similar ΔK, but the stress intensity factor for smaller cracks is being understimated. So the correction factor C_f is introduced:

$$C_f = \left(1 + \frac{1}{2}\sqrt{\frac{\rho^*}{a}} \right) \tag{4.2.22}$$

and the stress intensity factors are corrected accordingly:

$$K_{\text{min,appl}} = C_f \cdot S_{\text{min,appl}} \cdot Y \cdot \sqrt{\pi a} \tag{4.2.23}$$

$$K_{\text{max,appl}} = C_f \cdot S_{\text{max,appl}} \cdot Y \cdot \sqrt{\pi a} \tag{4.2.24}$$

for more details about the short crack size and the derivation of C_f the reader may refer to [48]. Moreover, a correction factor for the plastic zone size C_p has been proposed in [48]. Since the elasto-plastic material won't follow the elastic stress profile after it has reached the yielding stress σ_{ys}, a redistribution of the plastic zone is needed in order to preserve the strain energy:

$$E = \int_{\frac{\rho^*}{2}}^{r_p} \sigma_y(x)dx - \sigma_{ys}\left(r_p - \frac{\rho^*}{2}\right) \tag{4.2.25}$$

where r_p is the dimension of the plastic zone and can be found from the equation:

$$\sigma_y(r_p) = \sigma_{ys} \tag{4.2.26}$$

This method takes a part E of the elastic strain energy which corresponds to the "surplus" of energy given by stresses with values above the threshold σ_{ys} and redistributes it, enlarging the plastic zone by Δr_p:

$$\Delta r_p \cdot \sigma_{ys} = E \Rightarrow \Delta r_p = \frac{(\rho^* - 2r_p)^2}{2(2r_p + \rho^*)} \tag{4.2.27}$$

so that the new plastic zone is in the interval $\left[\frac{\rho^*}{2}, r_p + \Delta r_p\right]$. The correction factor C_p is a function of the distance from the crack tip and its expressions can be found in [48] or [5]. It is important to apply the correction factor to the elastic stress before using the Neuber or the ESED rules.

The following calculations are carried out supposing a plane stress condition at the crack tip and making use of the Neuber rule, but it is possible to use other conditions and rules such as plain strain and the ESED rule (equivalent strain energy density, explained as the Glinka's rule in chapter 2).

Now that the elastic stresses have been obtained, the Neuber rule is used to relate them to the applied elastic-plastic stresses and strains:

$$\sigma^e \varepsilon^e = \sigma^a \varepsilon^a \tag{4.2.28}$$

Since the analysis regards a block of dimension ρ^*, the elastic stresses will be the average along the grain:

$$\overline{\sigma}^e_{y,i} = \frac{1}{x_{i+1} - x_i} \int_{x_i}^{x_{i+1}} \frac{K}{\sqrt{2\pi x}} \left(\frac{\rho^*}{2x} + 1 \right) dx \tag{4.2.29}$$

$$\overline{\sigma}^e_{x,i} = \frac{1}{x_{i+1} - x_i} \int_{x_i}^{x_{i+1}} \frac{K}{\sqrt{2\pi x}} \left(-\frac{\rho^*}{2x} + 1 \right) dx \tag{4.2.30}$$

after integrating the previous expression, the following forms are obtained:

$$\overline{\sigma}^e_{y,i} = \frac{K \cdot \Psi_{y,i}}{\sqrt{2\pi\rho^*}} \tag{4.2.31}$$

$$\overline{\sigma}^e_{x,i} = \frac{K \cdot \Psi_{x,i}}{\sqrt{2\pi\rho^*}} \tag{4.2.32}$$

where for the first four blocks: $\Psi_{y,1} = 1.633$, $\Psi_{y,2} = 0.8967$, $\Psi_{y,3} = 0.6773$, $\Psi_{y,4} = 0.5641$ and $\Psi_{x,1} = 0.4376$, $\Psi_{x,2} = 0.5287$, $\Psi_{x,3} = 0.4814$, $\Psi_{x,4} = 0.4378$ [44].

The calculation of $\Psi_{y,1}$ will now be carried out as an example:

$$\begin{aligned}
\overline{\sigma}^e_{y,1} &= \frac{1}{x_2 - x_1} \int_{x_i}^{x_2} \frac{K}{\sqrt{2\pi x}} \left(\frac{\rho^*}{2x} + 1 \right) dx = \frac{1}{\rho^*} \int_{\rho^*/2}^{3\rho^*/2} \frac{K}{\sqrt{2\pi x}} \left(\frac{\rho^*}{2x} + 1 \right) dx \\
&= \frac{K}{\sqrt{2\pi}} \int_{\rho^*/2}^{3\rho^*/2} \frac{1}{2x\sqrt{x}} dx + \frac{K}{\sqrt{2\pi}\rho^*} \int_{\rho^*/2}^{3\rho^*/2} \frac{1}{\sqrt{x}} dx \\
&= \frac{K}{\sqrt{2\pi}} \cdot \left(\sqrt{\frac{2}{\rho^*}} - \sqrt{\frac{2}{3\rho^*}} \right) + \frac{K}{\sqrt{2\pi}\rho^*} \cdot \left(2\sqrt{\frac{3\rho^*}{2}} - 2\sqrt{\frac{\rho^*}{2}} \right) \\
&= \frac{K}{\sqrt{2\pi\rho^*}} \left(\sqrt{2} - \sqrt{\frac{2}{3}} + 2\sqrt{\frac{3}{2}} - 2\sqrt{\frac{1}{2}} \right) \\
&\simeq \frac{1.633K}{\sqrt{2\pi\rho^*}}
\end{aligned} \tag{4.2.33}$$

One last thing to remember is that all these calculations are based on the linear elastic hypothesis and that's the reason of the "e" superscript in $\overline{\sigma}^e_{y,i}$ and $\overline{\sigma}^e_{x,i}$.

Elastic-plastic stress and strain can then be obtained solving the system:

$$\begin{cases} \overline{\varepsilon}^a_{x,\max} = \frac{1}{E}(\overline{\sigma}^a_{x,\max} - \nu\overline{\sigma}^a_{y,\max}) + \frac{f(\sigma^a_{\text{eq}})}{\sigma^a_{\text{eq}}}\left(\overline{\sigma}^a_{x,\max} - \frac{1}{2}\overline{\sigma}^a_{y,\max}\right) \\ \overline{\varepsilon}^a_{y,\max} = \frac{1}{E}(\overline{\sigma}^a_{y,\max} - \nu\overline{\sigma}^a_{x,\max}) + \frac{f(\sigma^a_{\text{eq}})}{\sigma^a_{\text{eq}}}\left(\overline{\sigma}^a_{y,\max} - \frac{1}{2}\overline{\sigma}^a_{x,\max}\right) \\ \overline{\sigma}^e_{x,\max}\overline{\varepsilon}^e_{x,\max} = \overline{\sigma}^a_{x,\max}\overline{\varepsilon}^a_{x,\max} \\ \overline{\sigma}^e_{y,\max}\overline{\varepsilon}^e_{y,\max} = \overline{\sigma}^a_{y,\max}\overline{\varepsilon}^a_{y,\max} \end{cases} \tag{4.2.34}$$

where $\sigma^a_{\text{eq}} = \sqrt{(\overline{\sigma}^a_{x,\max})^2 - \overline{\sigma}^a_{x,\max}\overline{\sigma}^a_{y,\max} + (\overline{\sigma}^a_{y,\max})^2}$ and $f(\sigma^a_{\text{eq}}) = \left(\frac{\sigma^a_{\text{eq}}}{H_c}\right)^{1/h_c}$.

Elastic-plastic stress and strain ranges can be determined solving a similar system:

$$\begin{cases} \Delta\overline{\varepsilon}^a_x = \frac{1}{E}(\Delta\overline{\sigma}^a_x - \nu\Delta\overline{\sigma}^a_y) + \frac{f(\sigma^a_{\text{eq}})}{\sigma^a_{\text{eq}}}\left(\Delta\overline{\sigma}^a_x - \frac{1}{2}\Delta\overline{\sigma}^a_y\right) \\ \Delta\overline{\varepsilon}^a_y = \frac{1}{E}(\Delta\overline{\sigma}^a_y - \nu\Delta\overline{\sigma}^a_x) + \frac{f(\sigma^a_{\text{eq}})}{\sigma^a_{\text{eq}}}\left(\Delta\overline{\sigma}^a_y - \frac{1}{2}\Delta\overline{\sigma}^a_x\right) \\ \Delta\overline{\sigma}^e_x\Delta\overline{\varepsilon}^e_x = \Delta\overline{\sigma}^a_x\Delta\overline{\varepsilon}^a_x \\ \Delta\overline{\sigma}^e_y\Delta\overline{\varepsilon}^e_y = \Delta\overline{\sigma}^a_y\Delta\overline{\varepsilon}^a_y \end{cases} \tag{4.2.35}$$

where $\sigma^a_{\text{eq}} = \sqrt{(\Delta\overline{\sigma}^a_x)^2 - \Delta\overline{\sigma}^a_x\Delta\overline{\sigma}^a_y + (\Delta\overline{\sigma}^a_y)^2}$ and $f(\sigma^a_{\text{eq}}) = \frac{1}{2}\left(\frac{\sigma^a_{\text{eq}}}{2H_c}\right)^{1/h_c}$.

From (4.2.34) and (4.2.35) it's possible to calculate the residual stress σ_r subtracting the stress range $\Delta\overline{\sigma}^a_y$ to the maximum stress $\overline{\sigma}^a_{y,\max}$ at several locations ahead of the crack tip, obtaining a distribution of the residual stress versus the distance from the crack tip.

It may happen that the stress field ahead of the crack tip is compressive even without nominal compressive stresses (as seen in the section of the Neuber rule in chapter 2). This is especially true for low stress ratio ($R_{\text{appl}} = K_{\text{min,appl}}/K_{\text{max,appl}} < 0.5$). In these cases, since residual compressive stress ahead of the crack tip may have a huge impact on the crack propagation, a residual stress intensity factor K_r is included in the model:

$$K_r = \int_0^a \sigma_r(x)m(x,a)dx \tag{4.2.36}$$

where $m(x,a)$ is the weight function given by the expression:

$$m(x,a) = \frac{2}{\sqrt{2\pi(a-x)}}\left[1 + M_1\left(1-\frac{x}{a}\right)^{\frac{1}{2}} + M_2\left(1-\frac{x}{a}\right) + M_3\left(1-\frac{x}{a}\right)^{\frac{3}{2}}\right] \tag{4.2.37}$$

M_1, M_2, M_3 are geometrical factors which may be found in [43]. It was found out, however, that a good geometry-independent approximation can be given when the width of the residual compressive zone is small in comparison with the crack size a:

$$m(x,a) = \frac{2}{\sqrt{2\pi(a-x)}} \tag{4.2.38}$$

In order to be fully effective, the maximum applied stress intensity factor $K_{\text{max,appl}}$ must overcome the effect of residual stresses. The resultant total fatigue crack driving forces are then defined as:

$$K_{\text{max,tot}} = K_{\text{max,appl}} + K_r \tag{4.2.39}$$

and

$$\Delta K_{\text{tot}} = K_{\text{max,tot}} - K_{\text{min,tot}} = K_{\text{max,appl}} + K_r - K_{\text{min,appl}} = \Delta K_{\text{appl}} + K_r \tag{4.2.40}$$

the careful reader will remember that the compressive residual stress is negative and, for this reason, the effective total maximum stress intensity factor $K_{\text{max,tot}}$ will be smaller than $K_{\text{max,appl}}$ since the first part of the tensile stress will be used to "nullify" the effect of the compressive residual stresses.

Different cases for the calculation of K are now briefly summarized:

- when the applied stress ratios are relatively high ($R_{\text{appl}} > 0.5$) and the stress intensity ranges are relatively small ($\simeq \Delta K_{th}$), usually $K_r \simeq 0$ and so:

$$\begin{aligned} K_{\text{max,tot}} &= K_{\text{max,appl}} \\ K_{\text{min,tot}} &= K_{\text{min,net}} = K_{\text{min,appl}} \\ \Delta K_{\text{tot}} &= \Delta K_{\text{appl}} \end{aligned} \tag{4.2.41}$$

- when the applied stress ratios are not so high ($0 \leq R_{\text{appl}} \leq 0.5$) or when, despite high stress ratios, the stress intensity ranges are also relatively high (in the second phase of the $da/dN \times \Delta K$ plot), the residual stresses at the crack tip may play an important role in slowing the crack growth:

$$\begin{aligned} K_{\text{max,tot}} &= K_{\text{max,appl}} + K_r \\ K_{\text{min,tot}} &= K_{\text{min,net}} = K_{\text{min,appl}} \\ \Delta K_{\text{tot}} &= \Delta K_{\text{appl}} + K_r \end{aligned} \tag{4.2.42}$$

- in the case of negative stress ratios ($R_{\text{appl}} < 0$) the compressive part of the loading cycle is not entirely effective and, thus, the crack has been modeled as a notch resulting in a correction of $K_{\text{min,tot}}$:

$$\begin{aligned} K_{\text{max,tot}} &= K_{\text{max,appl}} + K_r \\ K_{\text{min,tot}} &= K_{\text{min,net}} = \frac{3\sqrt{\rho^*}}{2Y\sqrt{a}} K_{\text{min,appl}} \\ \Delta K_{\text{tot}} &= K_{\text{max,appl}} + K_r - \frac{3\sqrt{\rho^*}}{2Y\sqrt{a}} K_{\text{min,appl}} = \Delta K_{\text{net}} + K_r \end{aligned} \tag{4.2.43}$$

It is now possible to evaluate the actual stress and strain in the first elementary material block ahead of the crack tip. In the case of plane stress the stress field in the first block is uni-axial [46] (only σ_y is considered). The Neuber rule for the first block in this case may be written in the following form:

$$\overline{\sigma}^a \overline{\varepsilon}^a = \overline{\sigma}^e \overline{\varepsilon}^e = \frac{(\overline{\sigma}^e)^2}{E} = \frac{1}{E} \left(\frac{K \cdot \Psi_{y,1}}{\sqrt{2\pi\rho^*}} \right)^2 \tag{4.2.44}$$

adding the Ramberg-Osgood relation, the following systems are obtained:

$$\begin{cases} \overline{\varepsilon}^a_{\text{max}} = \frac{\overline{\sigma}^a_{\text{max}}}{E} + \left(\frac{\overline{\sigma}^a_{\text{max}}}{H_c} \right)^{\frac{1}{h_c}} \\ \frac{1}{E} \left(\frac{K_{\text{max,tot}} \cdot \Psi_{y,1}}{\sqrt{2\pi\rho^*}} \right)^2 = \frac{(\overline{\sigma}^a_{\text{max}})^2}{E} + \overline{\sigma}^a_{\text{max}} \cdot \left(\frac{\overline{\sigma}^a_{\text{max}}}{H_c} \right)^{\frac{1}{h_c}} \end{cases} \tag{4.2.45}$$

$$\begin{cases} \Delta\overline{\varepsilon}^a = \frac{\Delta\overline{\sigma}^a}{E} + 2\left(\frac{\Delta\overline{\sigma}^a}{2H_c}\right)^{\frac{1}{h_c}} \\ \frac{1}{E}\left(\frac{\Delta K_{\text{tot}}\cdot\Psi_{y,1}}{\sqrt{2\pi\rho^*}}\right)^2 = \frac{(\Delta\overline{\sigma}^a)^2}{E} + 2(\Delta\overline{\sigma}^a)\cdot\left(\frac{\Delta\overline{\sigma}^a}{2H_c}\right)^{\frac{1}{h_c}} \end{cases} \tag{4.2.46}$$

Applying the Coffin-Manson law with the Smith-Watson-Topper correction (2.2.41) to $\overline{\sigma}^a_{\max}$ and $\Delta\overline{\varepsilon}^a$ it is possible to find the number of cycles N_f which the crack necessitates to propagate through the first block:

$$\overline{\sigma}^a_{\max}\cdot\frac{\Delta\overline{\varepsilon}^a}{2} = \frac{\sigma_c^2}{E}\cdot(2N_f)^{2b} + \varepsilon_c\cdot\sigma_c\cdot(2N_f)^{b+c} \tag{4.2.47}$$

Once N_f is calculated, the equation (4.2.9) is used to determine the fatigue crack growth rate. Unfortunately, it's not possible to find a closed form for the solution of (4.2.9), (4.2.47), (4.2.45), and (4.2.46), but it is possible to find approximate closed form solutions if the plastic or the elastic terms can be neglected [44]. In both cases the solutions have the same form:

$$\frac{da}{dN} = C[(K_{\text{max,tot}})^p(\Delta K_{\text{tot}})^{1-p}]^\gamma \tag{4.2.48}$$

where in the predominantly plastic case (away from the ΔK_{th} region):

$$C = 2\rho^*\left(\frac{\Psi_{y,1}^2}{2^{\frac{h_c+3}{h_c+1}}\sigma_c\varepsilon_c\pi E\rho^*}\right)^{-\left(\frac{1}{b+c}\right)};\quad p = \frac{h_c}{h_c+1};\quad \gamma = -\frac{2}{b+c} \tag{4.2.49}$$

while in the predominantly elastic case (near to the ΔK_{th} region):

$$C = 2\rho^*\left(\frac{(\Psi_{y,1})^2}{4\pi\rho^*\sigma_c^2}\right)^{-\frac{1}{2b}};\quad p = 0.5;\quad \gamma = -\frac{1}{b}$$

It is interesting to perform a simple check of the units of measurement:

$$\begin{cases} \frac{da}{dN} \to \left[\frac{\text{m}}{\text{cycle}}\right] \Rightarrow C[(K_{\text{max,tot}})^p(\Delta K_{\text{tot}})^{1-p}]^\gamma \to \left[\frac{\text{m}}{\text{cycle}}\right] \\ K_{\text{max,tot}}, \Delta K_{\text{tot}} \to [\text{Pa} * \sqrt{\text{m}}] \\ \sigma_c, E \to [\text{Pa}] \\ ro^* \to [\text{m}] \end{cases} \tag{4.2.50}$$

$$\begin{cases} [(K_{\text{max,tot}})^p(\Delta K_{\text{tot}})^{1-p}]^\gamma \rightarrow ([\text{Pa} * \sqrt{\text{m}}]^{1-p} * [\text{Pa} * \sqrt{\text{m}}]^p)^\gamma = [\text{Pa} * \sqrt{\text{m}}]^\gamma \\ \text{plastic case: } C \rightarrow [\text{m}] * \left[\frac{1}{\text{m}*\text{Pa}^2}\right]^{-\left(\frac{1}{b+c}\right)} = [\text{m}]^{1+\frac{1}{b+c}} * [\text{Pa}]^{\frac{2}{b+c}} \\ \text{elastic case: } C \rightarrow [\text{m}] * \left[\frac{1}{\text{m}*\text{Pa}^2}\right]^{-\frac{1}{2b}} = [\text{m}]^{1+\frac{1}{2b}} * [\text{Pa}]^{\frac{1}{b}} \end{cases} \tag{4.2.51}$$

$$\begin{cases} \text{plastic case: } C[(K_{\text{max,tot}})^p(\Delta K_{\text{tot}})^{1-p}]^\gamma \rightarrow [\text{m}]^{1+\frac{1}{b+c}} * [\text{Pa}]^{\frac{2}{b+c}} * [\text{Pa} * \sqrt{\text{m}}]^{-\frac{2}{b+c}} = \left[\frac{\text{m}}{\text{cycle}}\right] \\ \text{elastic case: } C[(K_{\text{max,tot}})^p(\Delta K_{\text{tot}})^{1-p}]^\gamma \rightarrow [\text{m}]^{1+\frac{1}{2b}} * [\ \text{Pa}]^{\frac{1}{b}} * [\text{Pa} * \sqrt{\text{m}}]^{-\frac{1}{b}} = \left[\frac{\text{m}}{\text{cycle}}\right] \end{cases} \tag{4.2.52}$$

which shows that the formulae are, if not correct, at least sensible.

Variable amplitude spectra: the UniGrow model

The model described so far includes only the effect of the residual stress of the cycle which precedes the current cycle, not considering the other previous cycles. This procedure is valid for constant amplitude loading, but, in the case of variable amplitude loading, it must be corrected. In [44], it is underlined as the last cycle is not the only one influencing the current cycle. In order to determine the residual stress field at the crack tip four rules have been derived (the pictures that represent the first three rules refer to the loading in 4.6):

- The first rule states that only the compressive part of the minimum stress distribution affects the fatigue crack growth rate and should be considered when estimating the crack tip residual stress field (see Fig.4.7).
- The second rule states that if the compressive part of the minimum stress distribution of the current cycle is smaller in magnitude than the previous resultant minimum stress field, the current cycle's stress distribution does not contribute to the calculation of the residual stress field (see Fig.4.8).

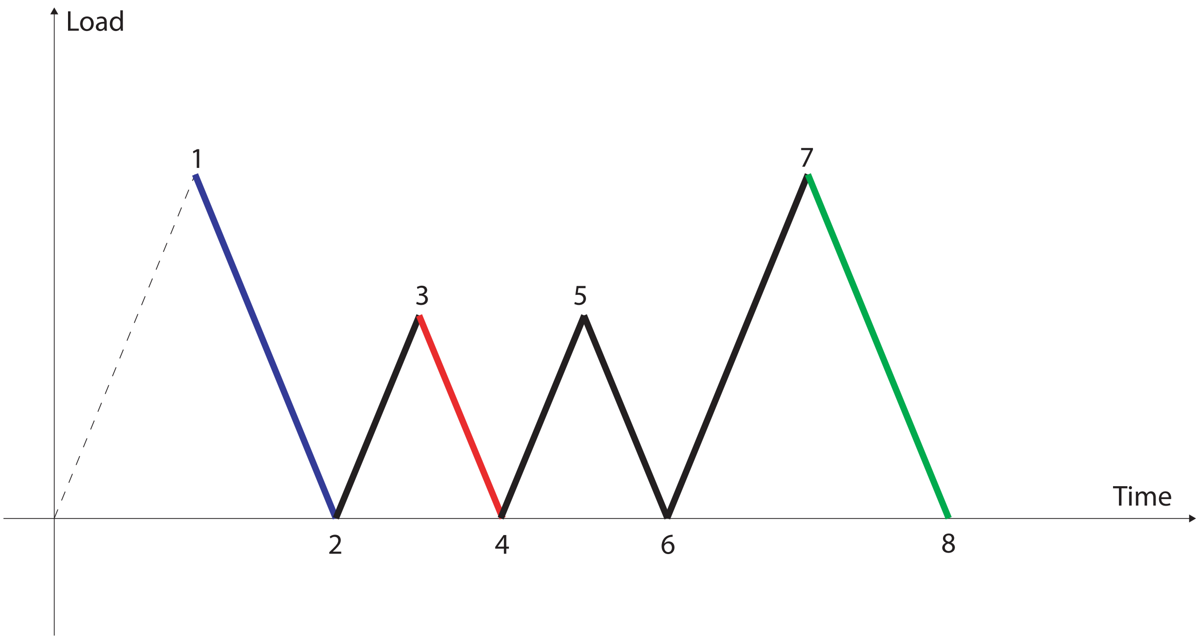

Figure 4.6: Simple loading history.

- The third rule states that if the compressive part of the minimum stress distribution of the current loading cycle is not inside of the previous resultant minimum stress field, the resultant stress field should be equal in each point to the minimum of the two (see Fig.4.9).

- The fourth rule states that each minimum stress distribution must be considered as long as the crack tip is inside its compressive stress region. When the crack tip has propagated across the compressive stress zone of a given minimum field, it should not be considered anymore (see Fig.4.10).

It should be also noted that, while overloads are important factors in the retardation of the fatigue crack growth, underloads are not. Actually, underloads can even induce a slight acceleration of the fatigue crack growth [51]. Referring to Fig.4.11, in the UniGrow model, the residual stress field associated with the underload affects only the fatigue crack growth caused by the next reversal (from point 2 to point 3). The next minimum stress dis-

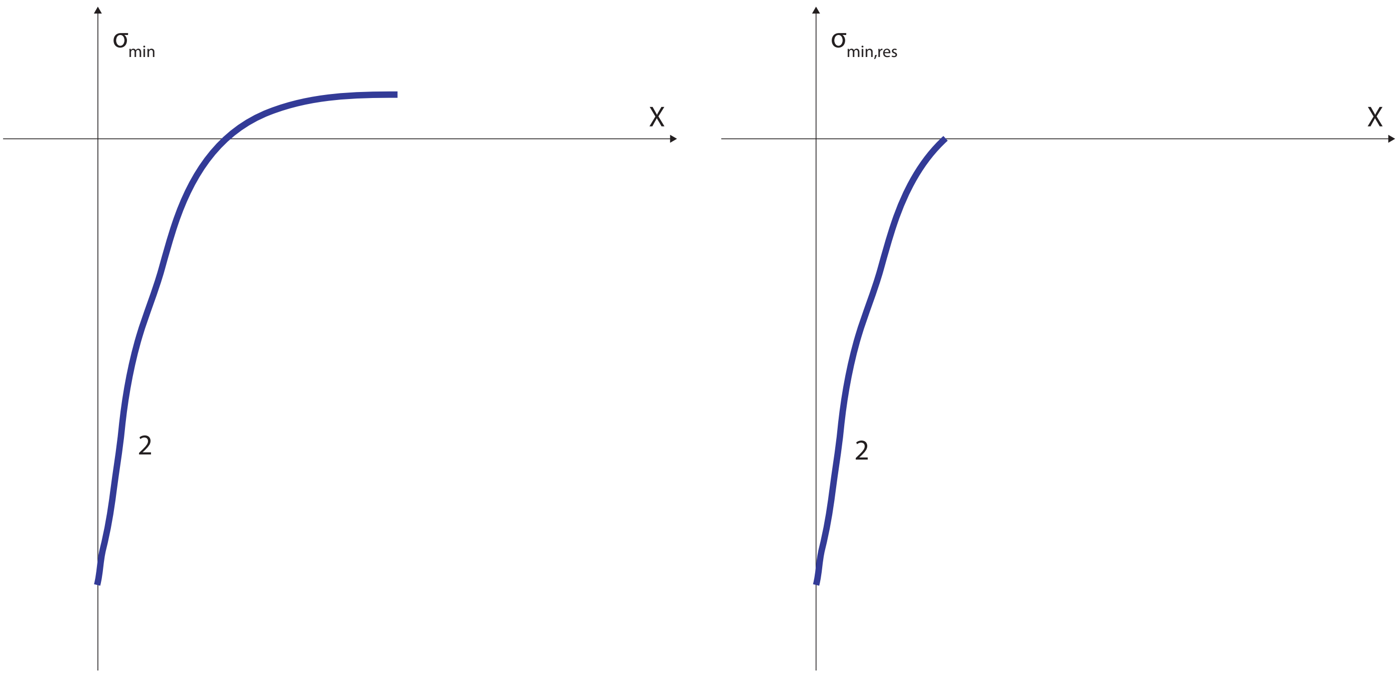

Figure 4.7: First rule: the tensile part of the minimum stress distribution doesn't affect the residual stress.

tribution (point 4) is calculated starting from the minimum stress generated by the underload (point 2), but following the cyclic stress-strain curve. After that, the compressive minimum stress distribution of the current cycle (point 4) will be used for the determination of K_r for the following calculations of crack growth increments.

Estimation of ρ^*

The most important parameter in the model, if we know the Coffin-Manson and the Ramberg-Osgood parameters, is ρ^*. Three methods are described in [44] for its estimation.

- The first method requires the knowledge of the fatigue limit and the threshold stress intensity range. This method hypothesizes that the fatigue crack can't grow if the stress intensity range is equal to or less than the threshold stress intensity range i.e. $\Delta K_{\text{appl}} \leq \Delta K_{th}$, therefore

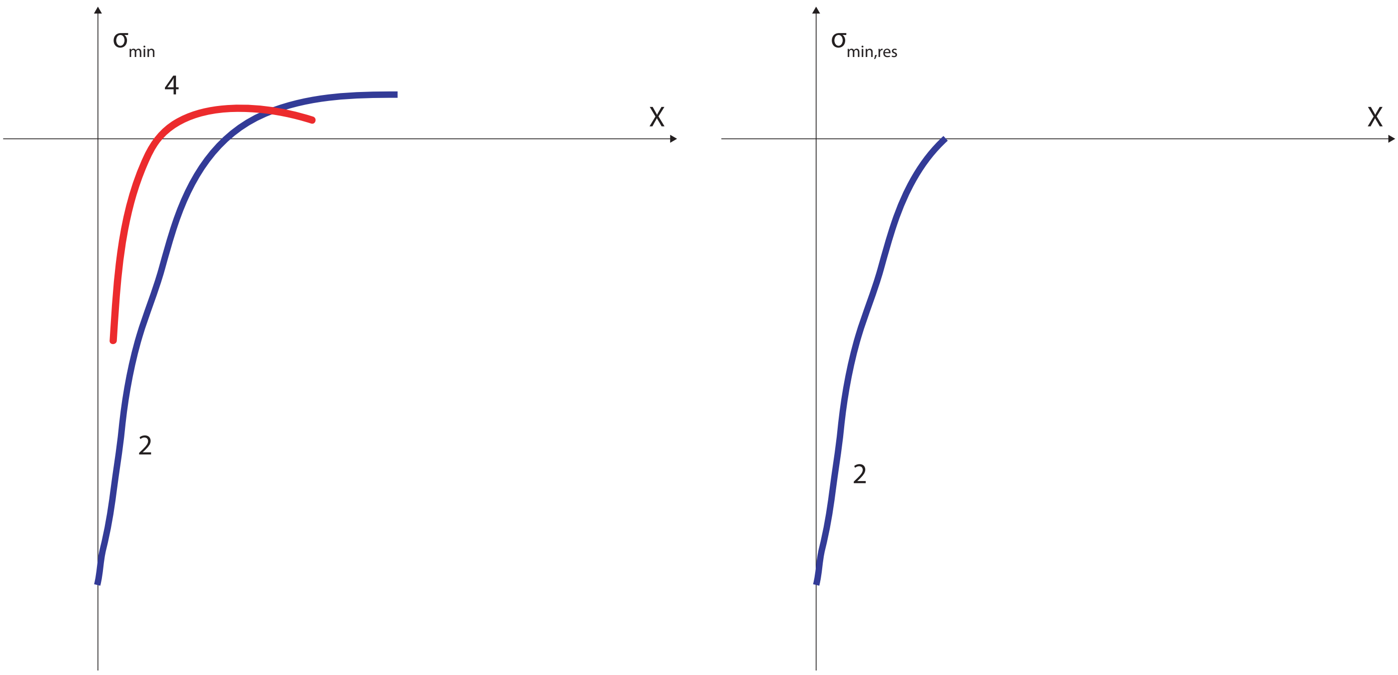

Figure 4.8: Second rule: if the current loading cycle has the minimum stress compressive part inside of the previous resultant minimum stress field, the current cycle's effects should be neglected.

in these cases the stress range in the first material block at the crack tip must be equal to or smaller than the fatigue limit, i.e. $\Delta\sigma_{\mathrm{appl}} \leq \Delta\sigma_{th}$. Since the fatigue limit is less than the yield limit, the analysis can be performed in the linear elastic case. Using equation (4.2.31) is possible to obtain:

$$\Delta\sigma_{th} = \frac{\Psi_{y,1} \cdot \Delta K_{th}}{\sqrt{2\pi\rho^*}} \tag{4.2.53}$$

rewriting the equation, is possible to estimate ρ^* as:

$$\rho^* = \frac{(\Psi_{y,1} \cdot \Delta K_{th})^2}{2\pi(\Delta\sigma_{th})^2} \tag{4.2.54}$$

The equation above provides a useful method to calculate ρ^*, but it also has some flaws. In fact, it is not always easy to have precise information

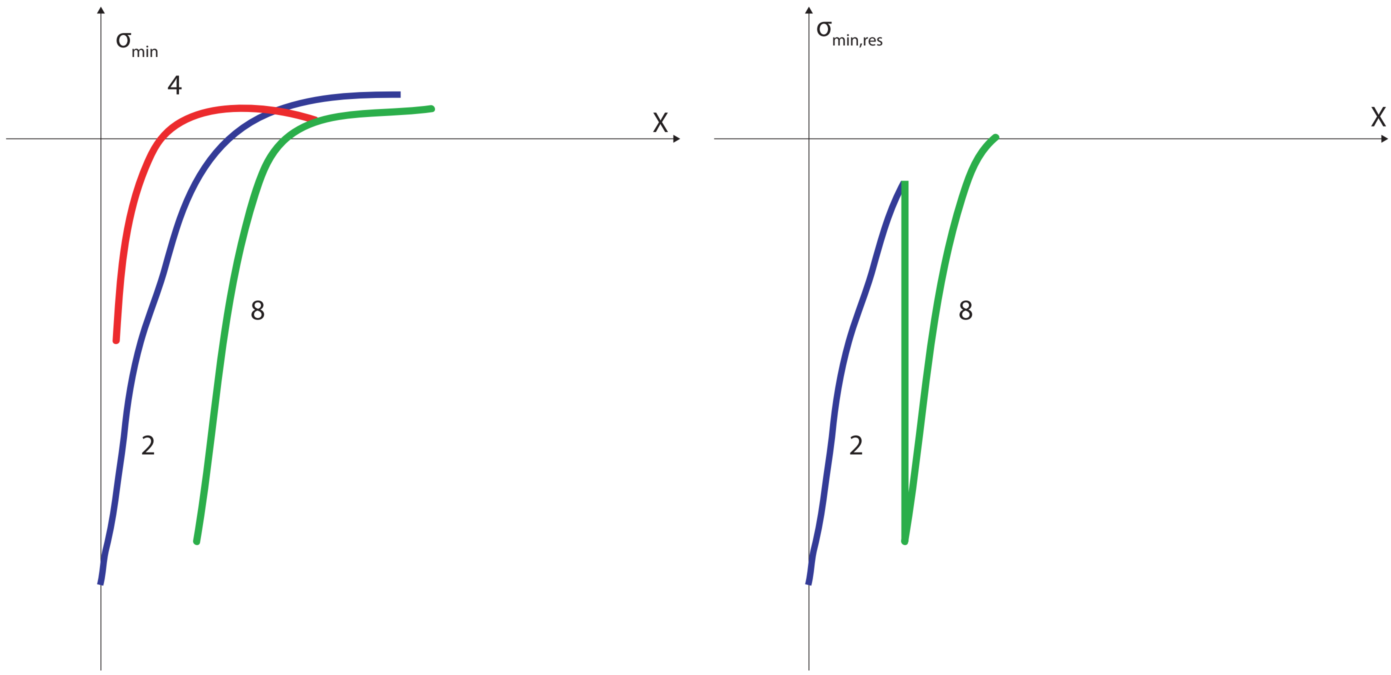

Figure 4.9: Third rule: when rule two doesn't apply the residual stress is equal in each point to the minimum between the two stress fields.

about ΔK_{th} and $\Delta\sigma_{th}$ (some materials don't even have a fatigue limit as in 2.1). It's also fundamental to have those two values for the same stress ratio R! Moreover, from a theoretical point of view, it doesn't seem correct to estimate ρ^* based only on the stress intensity range and not on the maximum stress intensity factor. It has been seen as both of them contribute to the growth of the crack and for this reason, both the maximum threshold stress intensity factor and the threshold stress intensity range should be exceeded for the crack to grow. It is also not clear whether ρ^* depends only on the material, as it should be, or also on the load and/or on the geometry. Finally, it should also be verified that ρ^* doesn't depend on the stress ratio at which ΔK_{th} and $\Delta\sigma_{th}$ have been determined.

- The second method is based on fatigue crack growth data obtained at various stress ratios. Since the mean stress effect has been already

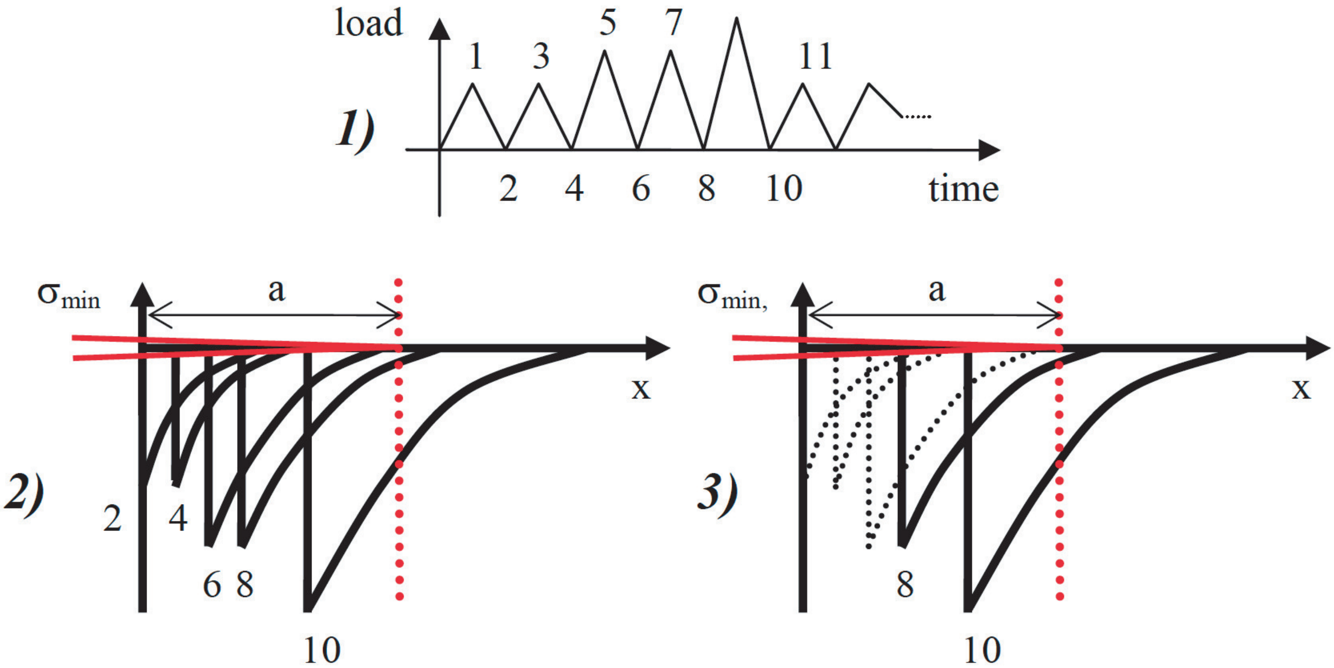

Figure 4.10: Fourth rule: once the crack tip is outside the compressive stress zone, its compressive field should be neglected (Picture by [44]).

accounted for using the SWT correction, all the experimental curves when plotted as functions of $\Delta k = K^p_{\text{max,tot}} \Delta K^{(1-p)}_{\text{tot}}$ should collapse onto one curve. On the other hand, it is possible to write Δk as:

$$
\begin{aligned}
\Delta k = K^p_{\text{max,tot}} \Delta K^{(1-p)}_{\text{tot}} &= (K_{\text{max,appl}} + K_r)^p (\Delta K_{\text{appl}} + K_r)^{1-p} \qquad (4.2.55)\\
&= \left(K_{\text{max,appl}} + \int_0^a \sigma_r(x, \rho^*) \cdot m(a, x) dx \right)^p \Bigg(\Delta K_{\text{appl}} \\
&+ \int_0^a \sigma_r(x, \rho^*) \cdot m(a, x) dx \Bigg)^{1-p} = \Delta k(\rho^*)
\end{aligned}
$$

where the only unknown parameter is ρ^*. It is then possible, solving an optimization problem, to find the best ρ^* such that the experimental curves for different ratios, plotted against $\Delta k(\rho^*)$ in a da/dN vs $\Delta k(\rho^*)$, are as close as possible one to the other. The problem, in this case, is the

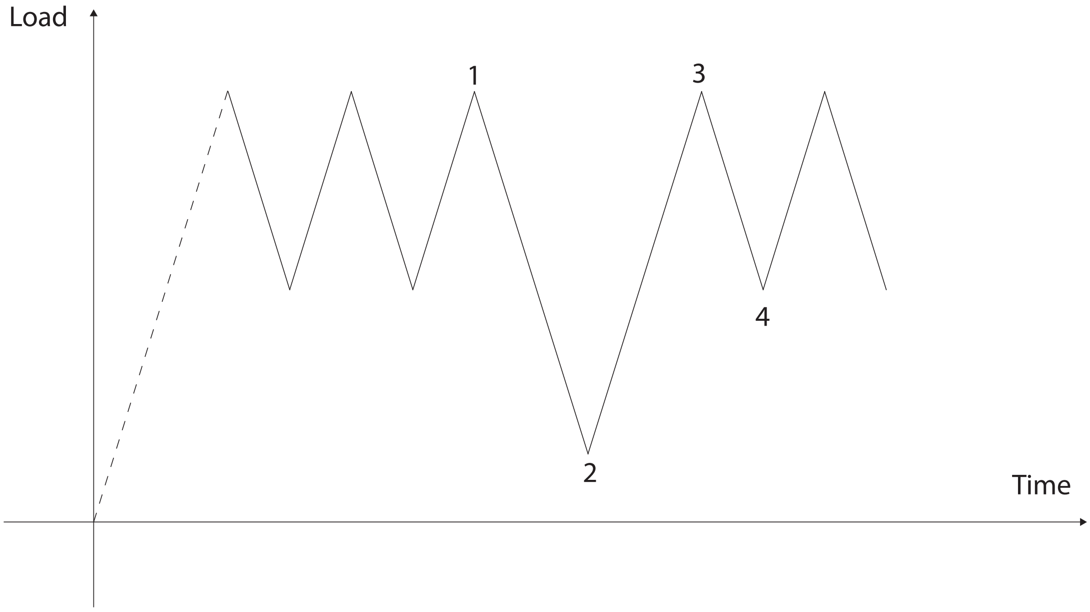

Figure 4.11: Constant amplitude loading history interrupted by a single underload.

need of a good amount of experimental fatigue crack growth data (at least three constant amplitude da/dN experimental curves for different ratios are needed) and the fact that ρ^* could not be unique in principle. However, the method provides good results since the parameters C and γ are based on experimental data fitting and can be also transformed in a set of (C_i, γ_i) for more precise fitting. Note, however, that the set of coefficients will depend on the ρ^* chosen as shown in [48].

- The third method requires experimental fatigue crack growth data as well. For each point in the $da/dN \times \Delta K$, both the parameters ΔK_{appl} and $K_{\text{max,appl}}$ are known. Following the Ramberg-Osgood equation and the Neuber rule the following expressions are obtained:

$$\frac{1}{E}\left(\frac{K_{\text{max,tot}} \cdot \Psi_{y,1}}{\sqrt{2\pi\rho^*}}\right)^2 = \frac{(\overline{\sigma}^a_{\text{max}})^2}{E} + \overline{\sigma}^a_{\text{max}} \cdot \left(\frac{\overline{\sigma}^a_{\text{max}}}{H_c}\right)^{\frac{1}{h_c}} \tag{4.2.56}$$

$$\frac{1}{E}\left(\frac{\Delta K_{\text{tot}} \cdot \Psi_{y,1}}{\sqrt{2\pi\rho^*}}\right)^2 = \frac{(\Delta\overline{\sigma}^a)^2}{E} + 2(\Delta\overline{\sigma}^a) \cdot \left(\frac{\Delta\overline{\sigma}^a}{2H_c}\right)^{\frac{1}{h_c}} \tag{4.2.57}$$

The elastic-plastic range can then be calculated:

$$\Delta\overline{\varepsilon}^a = \frac{\Delta\overline{\sigma}^a}{E} + 2\left(\frac{\Delta\overline{\sigma}^a}{2H_c}\right)^{\frac{1}{h_c}} \tag{4.2.58}$$

Considering the SWT equation:

$$\overline{\sigma}^a_{\max} \cdot \frac{\Delta\overline{\varepsilon}^a}{2} = \frac{\sigma_c^2}{E} \cdot (2N_f)^{2b} + \varepsilon_c \cdot \sigma_c \cdot (2N_f)^{b+c} \tag{4.2.59}$$

and the crack growth equation:

$$\frac{da}{dN} = \frac{\rho^*}{N} \tag{4.2.60}$$

Putting all together, there are 5 equations in 5 unknown variables, so it is possible to calculate ρ^* for each point in the $da/dN \times \Delta K$ plot. It should be noted that the total stress intensity range and intensity factor are required in the equations, but it's not possible to determine those since ρ^* is still unknown. The solution is to use the applied stress intensity range and intensity factor to get an initial estimation of ρ^* for each point, then those value will be iteratively used to obtain a more and more precise estimation of ρ^*. After few iterations (5-10 according to [44]), the method will converge and the calculated ρ^*s for each point of the $da/dN \times \Delta K$ plot will be similar to their average. An advantage of this method is that it only requires few data points (more than three is enough according to [44]). Moreover, the result doesn't depend on the stress ratio R [44], meaning that using data with different stress ratio would bring to the same estimation of ρ^*.

Chapter 5

Fatigue Analyses

In this chapter, the experimental set-ups will be illustrated. It will follow the description of the FE models used and then the results will be presented.

5.1 Experimental Set-ups

In order to evaluate the performance of the aforementioned methods, three sets of experimental data have been selected from the literature. The data are taken from [52], [53], and [55]. The first and the second article's tests have been performed on cruciform joints, while the third article's tests have been carried out on butt welded specimens. The experimental conditions for each case will now be briefly illustrated.

5.1.1 First case

The first set-up is described in [53]. The projection of the specimens' geometry in the xy-plane is shown in Fig.5.1 (all the measures are given in millimeters), while their width (dimension along the z-axis) is equal to 50 mm. As can it be seen from Fig.5.1, the load carrying cruciform joint is composed of four fillet welds. A traction loading was applied to the vertical plates.

The plates are made of Q345qD grade steel, a common steel in China, and have been welded using metal-cored arc welding. Tests have been carried out with load ratio $R = \sigma_{\min}/\sigma_{\max} = 0.1$.

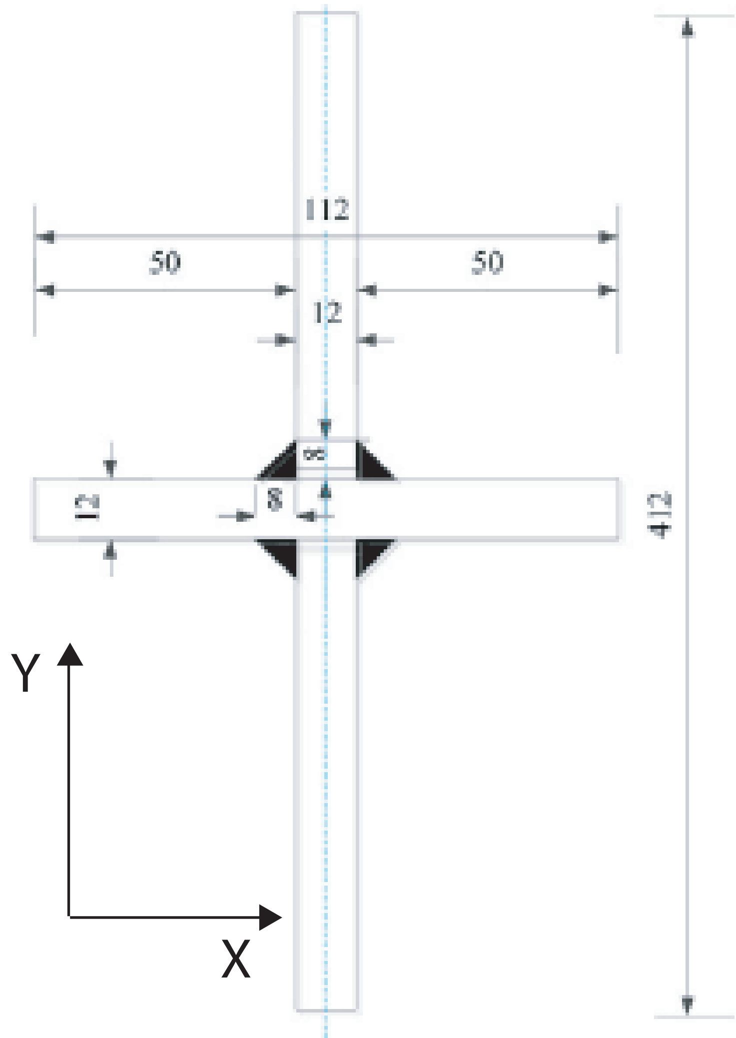

Figure 5.1: Geometry and nominal measures (mm) of the cruciform joints (Picture by [53]).

The authors of [53] also explained that the real geometry's measures differ from the nominal ones illustrated in 5.1. After measuring all the specimens, they calculated the true mean values which are shown in Tab.5.1 (see Fig.5.2 for the meaning of each variable). In particular, they noticed a mean misalignment $e = 1.96$ mm.

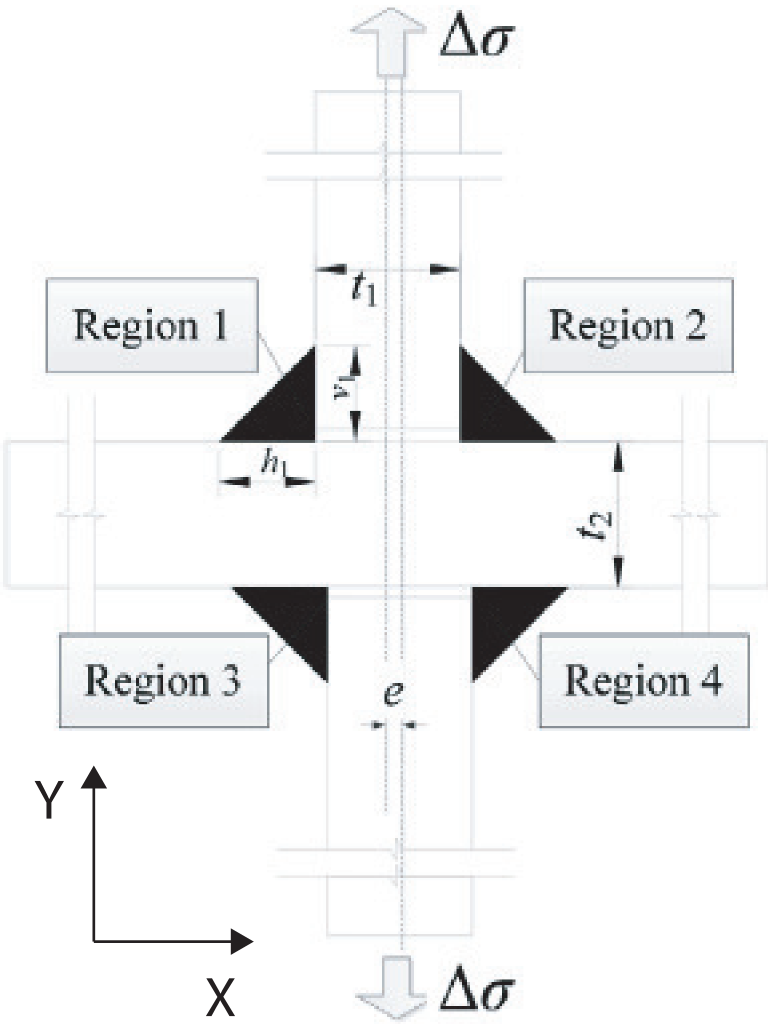

Figure 5.2: Actual mean geometry of the cruciform joints. See table 5.1 for the values (Picture by [53]).

5.1.2 Second case

The second set-up is described in [52]. The projection of the specimens' geometry in the xy-plane is shown in Fig.5.3 (all the measures are given in millimeters), while their width (dimension along the z-axis) is equal to

Table 5.1: Mean values table (mm).

t_1	t_2	h_1	v_1	h_2	v_2	h_3	v_3	h_4	v_4	e
11.85	11.83	9.57	9.58	9.45	9.45	9.89	9.76	9.79	9.84	1.96

100 mm. As it can be seen from Fig.5.3, the load carrying cruciform joint is composed of four fillet welds. The traction loading was applied to the horizontal plates.
The plates, made of duplex stainless steel (grade 2205), have been welded using gas tungsten arc welding. Tests have been carried out with load ratio $R = \sigma_{\min}/\sigma_{\max}$ equal to both 0.5 and 0.05.

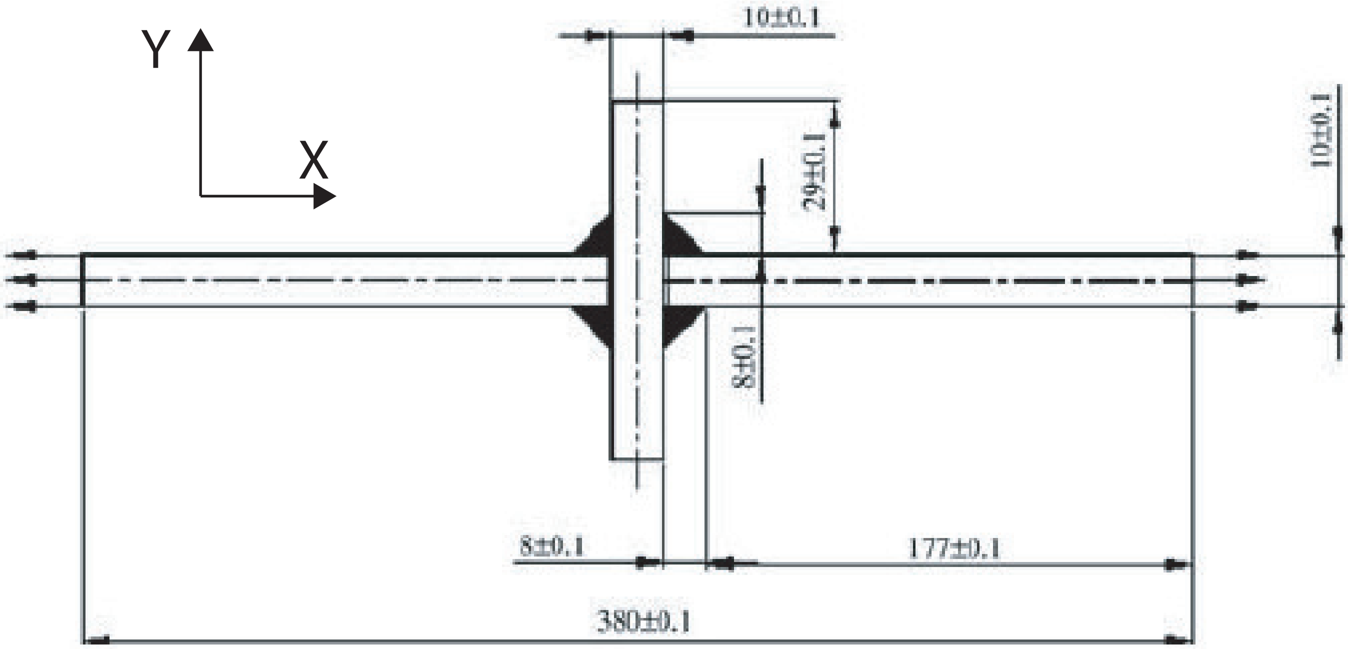

Figure 5.3: Geometry and measures (mm) of the cruciform joints (Picture by [52]).

5.1.3 Third case

The third set-up is described in [55]. The geometry of the specimens is shown in Fig.5.4 (all the measures are given in millimeters). As it can be seen from Fig.5.4, the two plates are connected by a single V-groove butt weld. The traction loading was applied in the longitudinal direction.
The specimens, made of ASTM A36 structural steel, have been welded using tungsten inert arc welding. Tests have been carried out with load ratio $R = \sigma_{\min}/\sigma_{\max} = 0.1$.

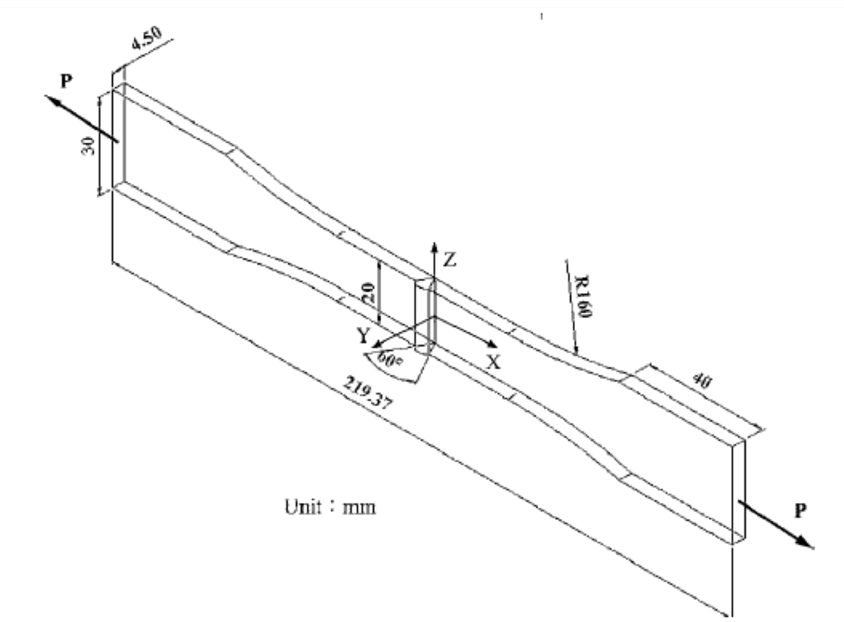

Figure 5.4: Geometry and measures (mm) of the butt welded specimens (Picture by [55]).

5.1.4 FE Models

For each experimental set-up, different FE models have been made. It has been shown in the previous chapter how joints can be modeled using both shell and solid elements. Moreover, fillet joints can be modeled by a single row or two rows of shell elements (see Fig.4.1 and Fig.4.2).

The following FE models have been used:

- case 1 (with misalignment):

  1º quadrilateral shell elements, single row, 1898 elements (see Fig.8.1 and 8.2);

  2º quadrilateral shell elements, two rows, 2002 elements (see Fig.8.3 and 8.4);

  3º tetrahedron solid elements, coarse mesh, 38392 elements (see Fig.8.9 and 8.10);

  4º tetrahedron solid elements, fine mesh, 275902 elements (see Fig.8.11 and 8.12).

- case 1 (with nominal geometry):

  1º quadrilateral shell elements, single row, 1937 elements (see Fig.8.5 and 8.6);

  2º quadrilateral shell elements, two rows, 2041 elements (see Fig.8.7 and 8.8);

  3º tetrahedron solid elements, coarse mesh, 38392 elements (see Fig.8.13 and 8.14);

  4º tetrahedron solid elements, fine mesh, 275902 elements (see Fig.8.15 and 8.16).

- case 2:

  1º quadrilateral shell elements, single row, 3100 elements (see Fig.8.17 and 8.18);

  2º quadrilateral shell elements, two rows, 3275 elements (see Fig.8.19 and 8.20);

  3º tetrahedron solid elements, 394988 elements (see Fig.8.21, and 8.22,).

- case 3:

  1° quadrilateral shell elements, 456 elements (see Fig.8.23 and 8.24);

  2° tetrahedron solid elements, 3358 elements (see Fig.8.31 and 8.32).

In case 1 with misalignment, which will be called the actual geometry's case from now on, the only variation from the nominal geometry's model is the offset, while the other minor variations in the measures (see Tab.5.1) are not considered. All the geometries and results of the FE analyses are in "Appendix: FE models".

5.2 Case 1

5.2.1 2D analyses

For the first case, four FE analyses have been carried out. Each FE result has been given as input to the Seam Weld glyph in nCode DesignLife. The results are plotted in Fig.5.5.

The first factor to notice in Fig.5.5 is that there isn't a meaningful difference between the one-row and two-rows type of modeling. On the other hand, there is a dissimilarity between the results with the nominal and actual geometry. In the last case, the predictions are more conservative. The experimental data fall between the two geometries' outputs. However, the curves give sensible predictions, which is good considering the simple modeling and the remarkable uncertainty typical of the fatigue phenomenon and confirmed by the sparsity of the data. The method seems to be a good solution if it is necessary to obtain a first estimation of the fatigue life at a minimum cost.

5.2.2 3D analyses

For the 3D FE models both Seam Weld and WholeLife have been used.
It has been seen that the Seam Weld function calculates the needed stresses from the FE results at a certain number of points through the thickness of

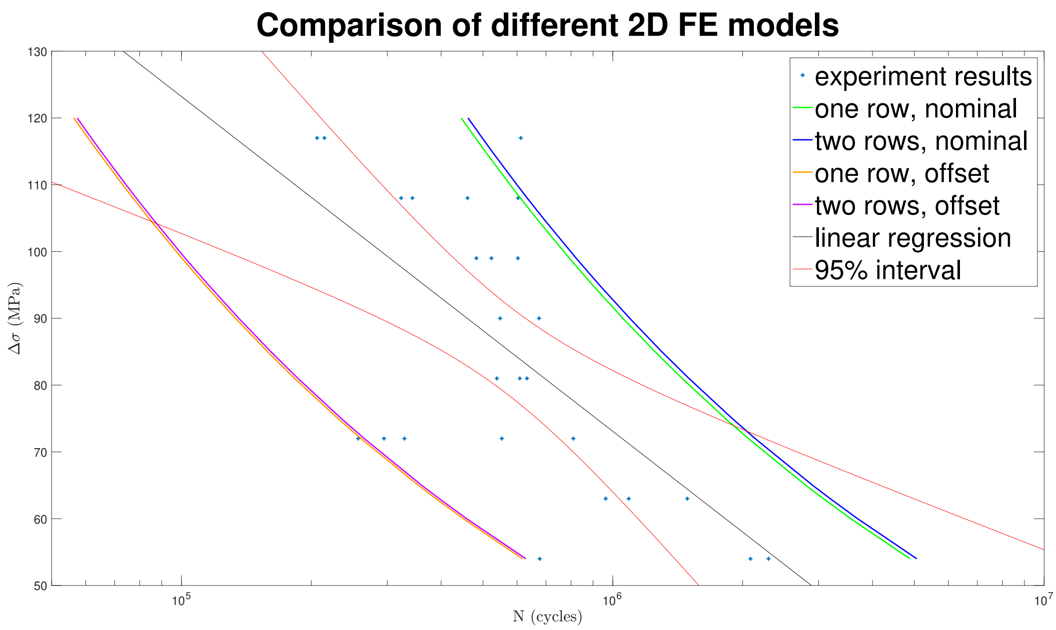

Figure 5.5: Case 1: Seam Weld analyses results for the four shell models.

the specimen. Because of this, it is necessary to specify both the number of points (layers) and the maximum depth at which they can be taken from the thickness of the specimen. Analyses have been carried out for both input parameters and the results are displayed in Fig.5.6 and Fig.5.7.

As it can be seen from Fig.5.6, the number of layers doesn't seem to make a big difference in the results as long as we take at least eight layers. The outputs seem to converge to a limit curve when the number of layers is increased. Since the performance of the method are not heavily conditioned by the number of layers, the parameter has been set to 15.
If for the first parameter we can't really make a wrong choice (even just three layers still give decent results), the same can't be said for the depth choice. Looking at Fig.5.7, it is possible to see important differences between the curves. The general advice from the literature is to use the whole plate's thickness to perform the calculations, but in the case of a cruciform joint, it is suggested to use only half of the plate's thickness. The plot confirms

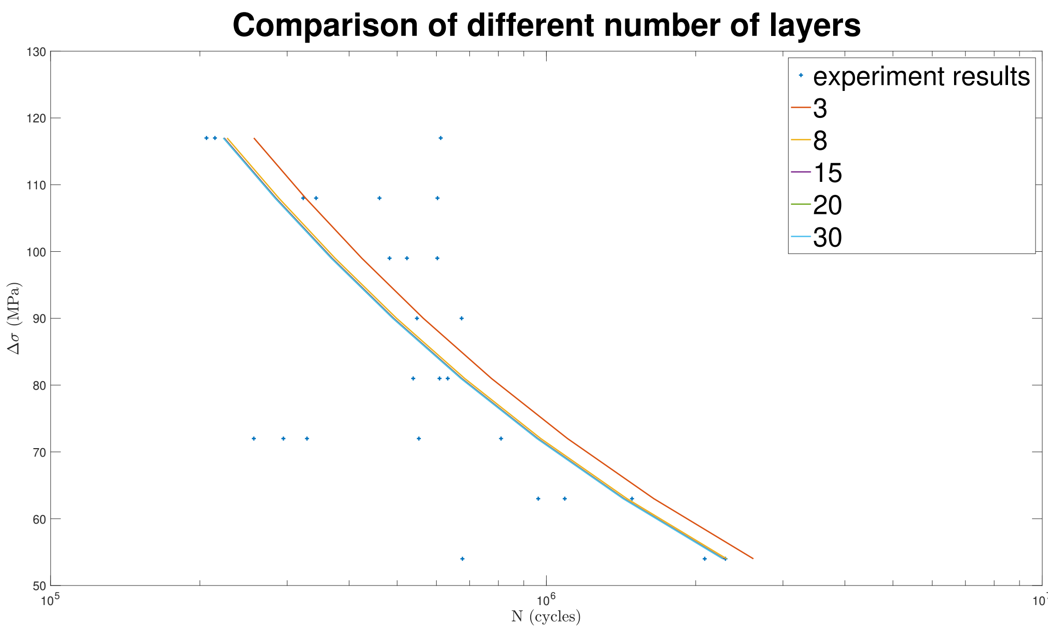

Figure 5.6: Case 1: comparison of the Seam Weld results for different number of layers.

this advice since the $t = 12$ mm's curve heavily overestimates the fatigue life. In the following analyses, $t = 6$ mm has been chosen since it is both the suggested and a good fitting value.

The Seam Weld analyses have been carried out for the four models and the results have been plotted in Fig.5.8.

Comparing the 3D results with the previous curves, it is possible to see a significative improvement in the output. All the curves fit better the data and the nominal geometry's curves give pretty good predictions overall. Again, the results for the actual mean geometry are more conservative than the ones for the nominal geometry, as well as the finer meshes give more conservative output when compared to the coarser ones. Actually, the mesh size should not influence the outputs of methods based on the structural stress, however, there are noticeable differences in the curves. Another interesting fact to

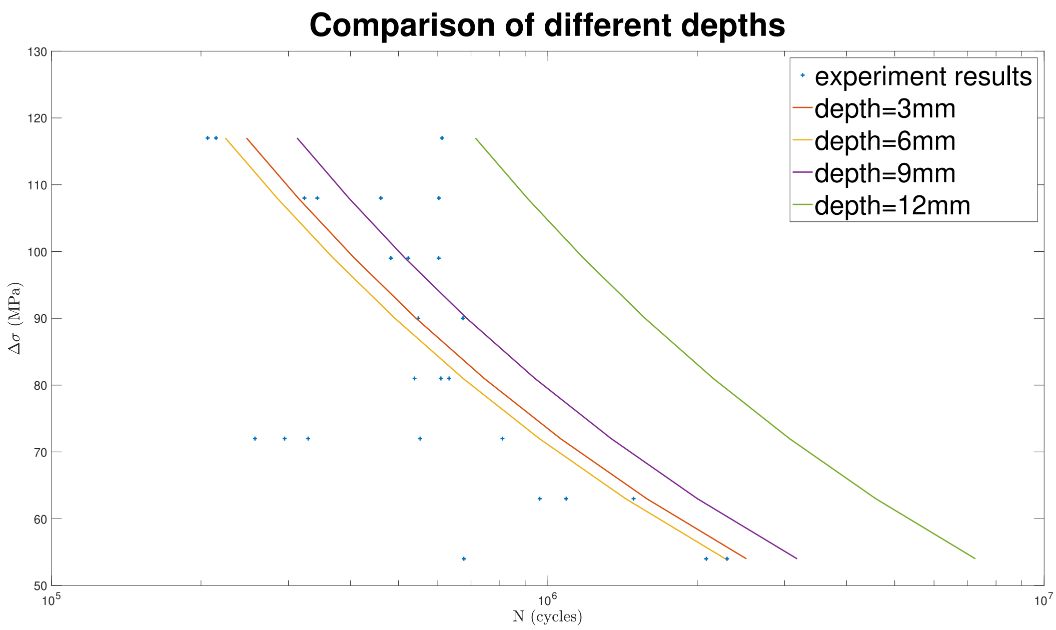

Figure 5.7: Case 1: comparison of the Seam Weld results for different depths.

notice is that the nominal geometry's curves tend to fit better the data for high $\Delta\sigma$, while the actual geometry's curves fit better the low $\Delta\sigma$ points. This could be because of many reasons:

1° Since only the mean value of the offset is known it could be that, by chance, the majority of the specimens tested with high $\Delta\sigma$ have a low or even negligible offset, while the specimens tested under lower stresses have an offset bigger than the mean one. This would also explain the strange trend of the data e.g. for $\Delta\sigma = 70$MPa (however, it is also true that it could just be the effect of the uncertainty of the fatigue phenomenon).

2° The effect of the offset is more important for lower stresses. While this could be true, it can't really be the only reason since the offset curves fit well data for low stresses which correspond to lifes that are equal or even lower than in the case of higher stresses. This reasoning would be more plausible if the low-stress data would correspond to slightly higher

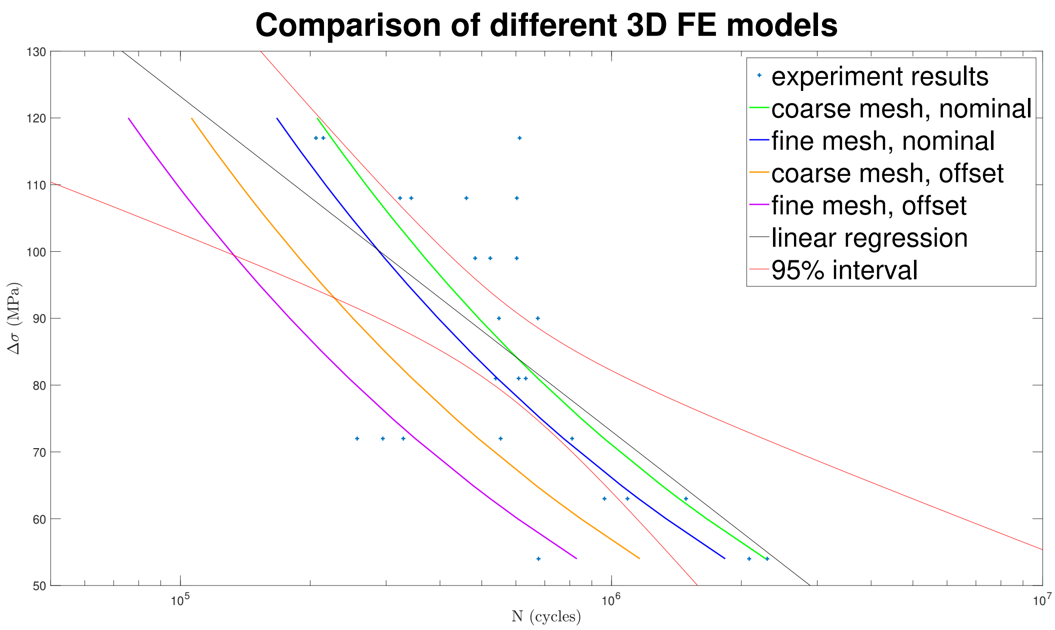

Figure 5.8: Case 1: comparison of the Seam Weld results with 3D modeling.

lifes than the high-stress data, which could represent a gradual change of the fatigue line's slope. However, considering the small amount of data, it is not unreasonable to think that the distribution of points for high stresses is biased. In that case, this hypothesis would become reasonable, but additional experiments are required in order to assess the veridicality of this statement.

3° The third hypothesis is that the low-stress data (especially the $\Delta\sigma =$ 70MPa) are biased because lower than their "true" averages. This would lead us to conclude that the method is just a little more conservative than it should be. Again, this hypothesis should be checked by further experiments.

The four models have been used as input for the WholeLife glyph as well. Missing the parameters for the Q345qD grade steel, values from similar steels have been taken for the Coffin-Manson curve [57]. One key parameter for WholeLife is ρ^*. In the previous chapter, various methods for the estimation of ρ^* have been presented, but probably the more interesting is the first one for its simplicity (see 4.2.54). σ^a_{th} has been estimated with half the ultimate tensile strength, which is a well-known procedure for steels (even if it is risky to take such an approach, sometimes it is inevitable) $\sigma^a_{th} \simeq 0.5 \cdot S_U$. ΔK_{th} has been instead calculated from the formula in [54]: $\Delta K_{th} = 11.54 \cdot (1 + 0.365) = 15.7521$. After ρ^* has been estimated, the other parameters have been obtained from 4.2.49.

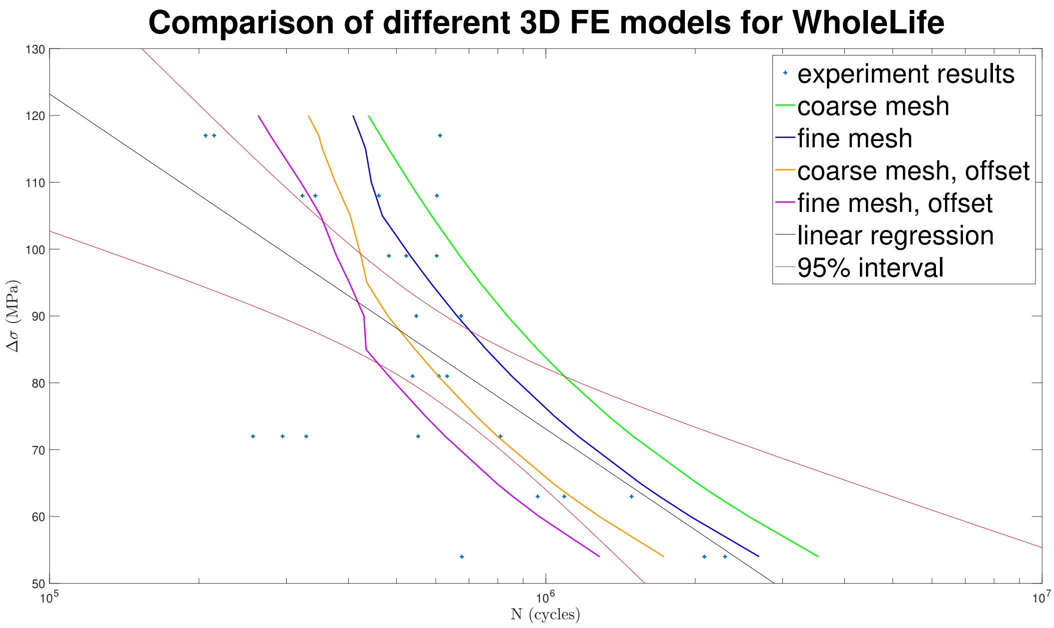

Figure 5.9: Case 1: comparison of the WholeLife results.

The results of Fig.5.9 are even better than in the Seam Weld 3D case. In particular, the actual geometry's curves seem to fit almost perfectly the data. The authors' estimation of ρ^* gave good results, but we have seen in the previous chapter that this estimation has some flaws. In particular, it is not always easy to find the values of ΔK_{th} and $\Delta\sigma_{th}$ for the same ratio and it is not clear if the estimation depends only on the material or if it also depends on the load type, ratio, and geometry. For this reason, ρ^* has been estimated with the mean grain size of the weld material. This estimation is free from all the flaws of the previous one.

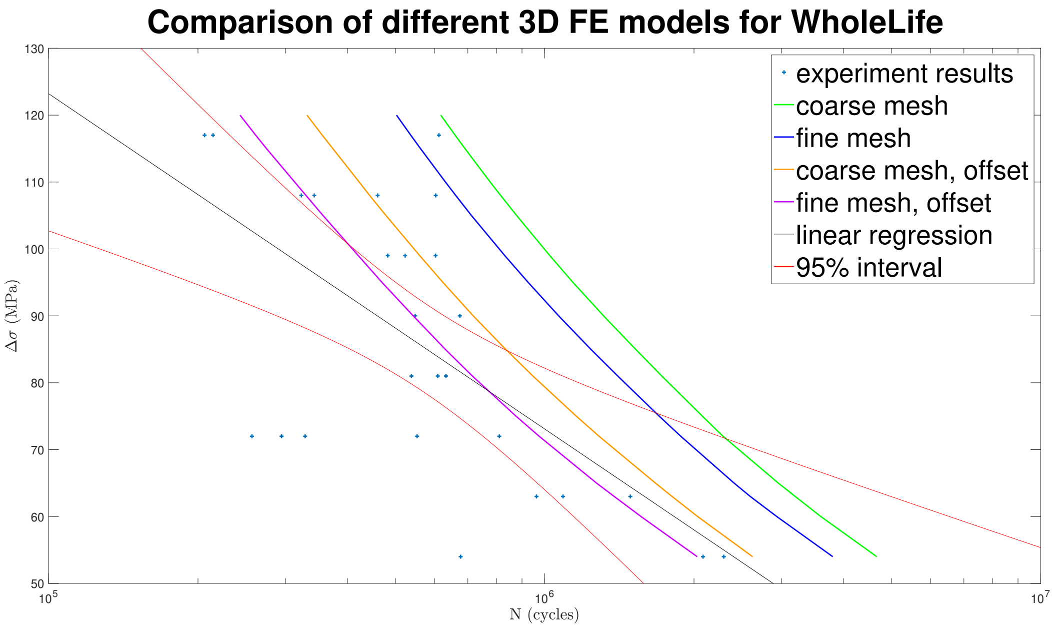

Figure 5.10: Case 1: comparison of the WholeLife results for ρ^* equal to the mean grain size.

The curves have been plotted in Fig.5.10. Again, the actual geometry's results are better than the nominal geometry's ones, which is what should theoretically happen, even if the best curve slightly overestimates the fatigue life for higher stresses. Still, this new estimation seems to be a possible solution when the other estimations are not possible.

5.2.3 Comparison with the Eurocode standard

"The EN Eurocodes are a series of 10 European Standards, EN 1990 - EN 1999, providing a common approach for the design of buildings and other civil engineering works and construction products" [60]. Among those standards, there are important guidelines for fatigue design (see [49]). In particular, the standard uses the nominal approach to provide the user with appropriate design curves. As the authors wrote, "According to Eurocode3 the cruciform joints with fillet welds are classified as FAT63 and FAT36 with respect to weld toe failure and weld root failure, respectively" [53]. The Eurocode's curves have been plotted in Fig.5.11.

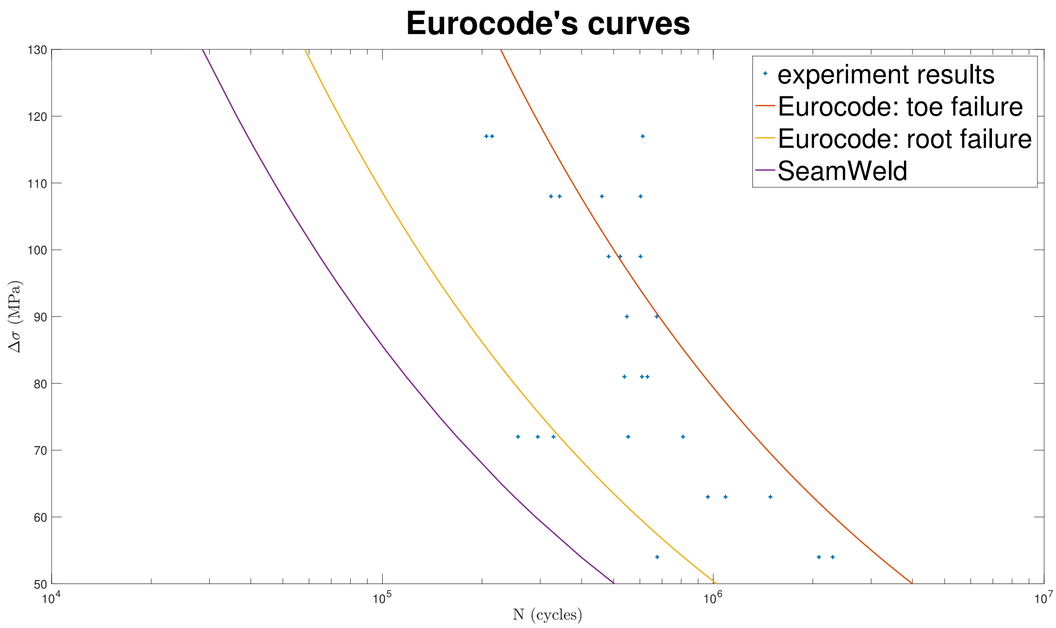

Figure 5.11: Case 1: Eurocode's curves vs the Seam Weld curve for 95% probability of survival.

Looking at Fig.5.11 the reader could think that the Eurocode's curves are useful since they fit well the data, however, that would neglect an important factor. The curves presented in the Eurocode standard are design curves. This means that they should already incorporate some safety factors because they should be used without too many modifications. In particular, these curve "were calculated for a 75% confidence level of 95% probability of survival for log N" [49] and for this reason, the 95% probability of survival curve calculated using Seam Weld with solid elements are plotted as well. The Eurocode's design curves should be conservative, but they clearly fail to do so. This is because the maximum offset allowed in the standard is $e = 0.15 \cdot t$, where t is the thickness of the intermediate plate. However, in this case the mean offset is $e \simeq 0.163 \cdot t$ and this is probably the main reason for the inadequacy of the Eurocode's design curves. However, the Seam Weld method provides an adequate design curve and it proves to be an important design tool in this situation.

5.3 Case 2

5.3.1 2D analyses

The second case comprehends experiment results with ratios $R = 0.05$ and $R = 0.5$. As in the previous case, both the single-row and the two-rows shell models have been analyzed.

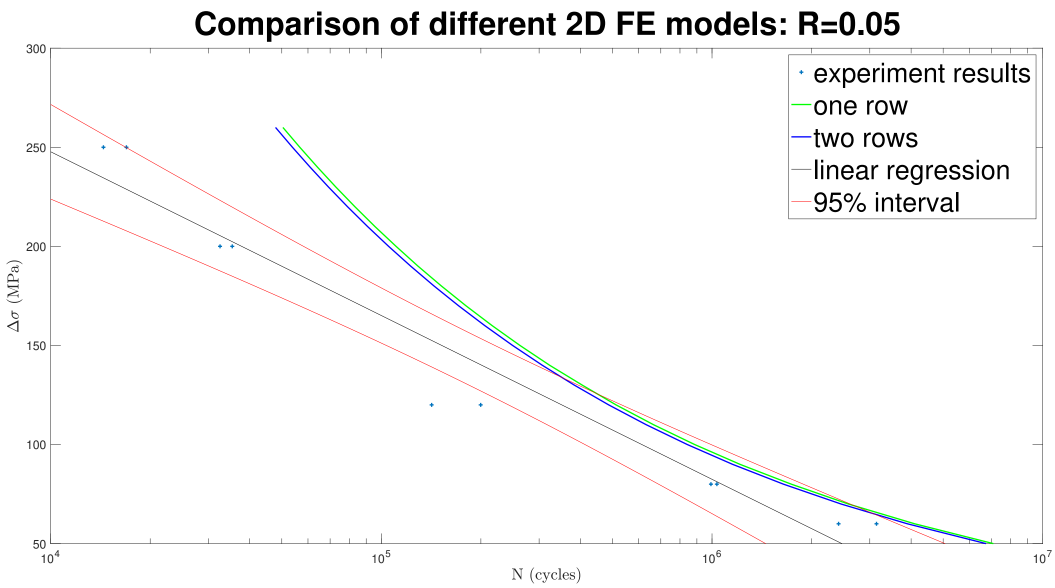

Figure 5.12: Case 2: Seam Weld analyses results for the two shell models, R=0.05.

From Fig.5.12 and 5.13 we can confirm that the difference between the two ways of modeling the weld is negligible and conclude that both provide similar results and seem, at least for tensile loads, interchangeable. The results are non-conservative, but they are overall acceptable considering the simplicity

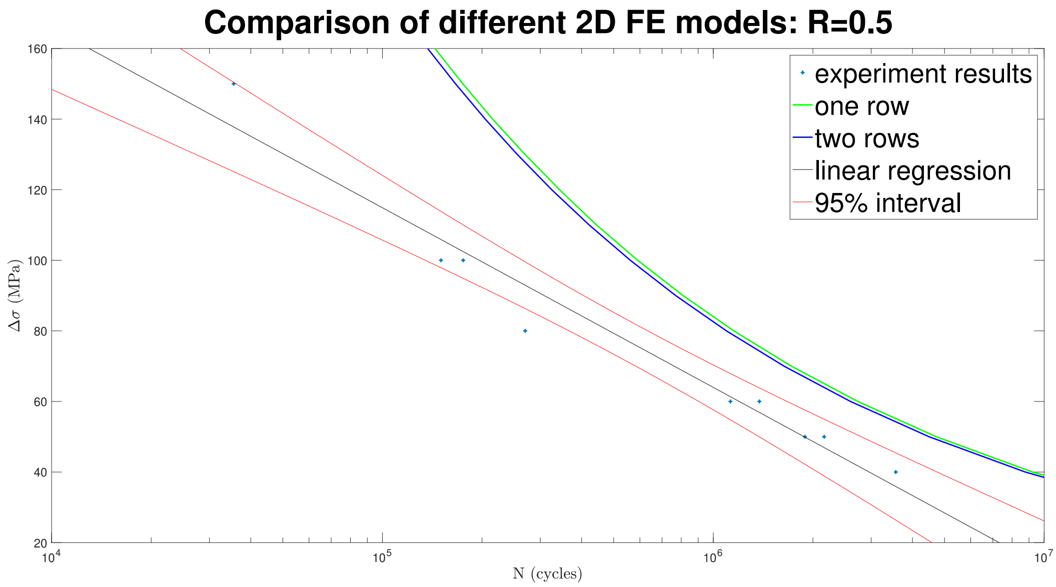

Figure 5.13: Case 2: Seam Weld analyses results for the two shell models, R=0.5.

of the shell models. It is possible to notice that the results are qualitatively similar in both cases, which proves the consistency of the method for different ratios.

5.3.2 3D analyses

For the 3D analyses, only one FE model has been used. However, since the specimens of [52] suffered from failure at the throat, both throat and toe failure have been considered. In order to do so, the weld configuration file of Seam Weld for the solid case has been modified accordingly.

In Fig.5.14 and 5.15, once again, the reliability of the solid models is shown. The "toe failure" line seems to overestimate the life for higher stresses, but has a better fit overall, while the "throat failure" line tends to be more conservative. However, there isn't a huge difference between the two curves.

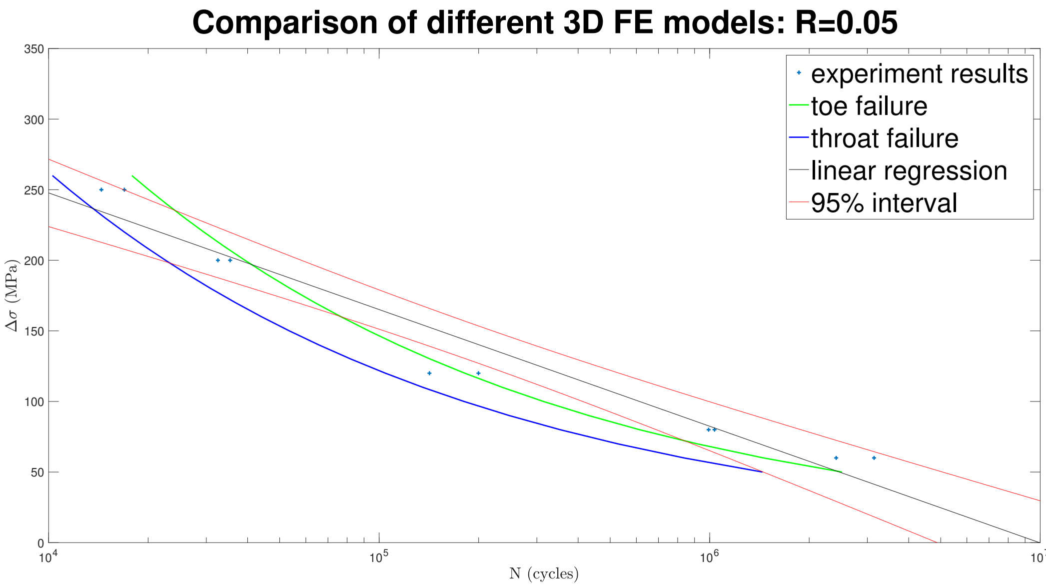

Figure 5.14: Case 2: comparison of the Seam Weld results with 3D modeling, R=0.05.

For the WholeLife setup, as before, two values of ρ^* have been chosen: one calculated from 4.2.54 and one based on the mean grain size of the material. Missing specific data, the grain size has been taken from another duplex steel. In the absence of the ΔK_{th} data at $R = -1$, the estimation of σ^a_{th} for $R = -1$ has been converted to different ratios as needed (remember that 4.2.54 is valid only for ΔK_{th} and $\Delta\sigma_{th}$ measured at the same ratio!). For this purpose, the Gerber and Goodman formulae were used (see 2.2.13 and 2.2.14). Since in the previous case the mean grain size estimation of ρ^* gave good results, the estimated ρ^* chosen was the one most similar to the mean grain size (after looking at the output, it was indeed the right choice since the other values of ρ^* gave even more non-conservative results).

From Fig. 5.16 and 5.17 it is possible to see how the mean grain size estimation of ρ^* gave better results than the estimation based on ΔK_{th}. Even if the results may be considered acceptable, the curves are overestimating the experimental results a bit too much. This is due to the fact that the specimens had initial cracks already present before the tests. The authors of

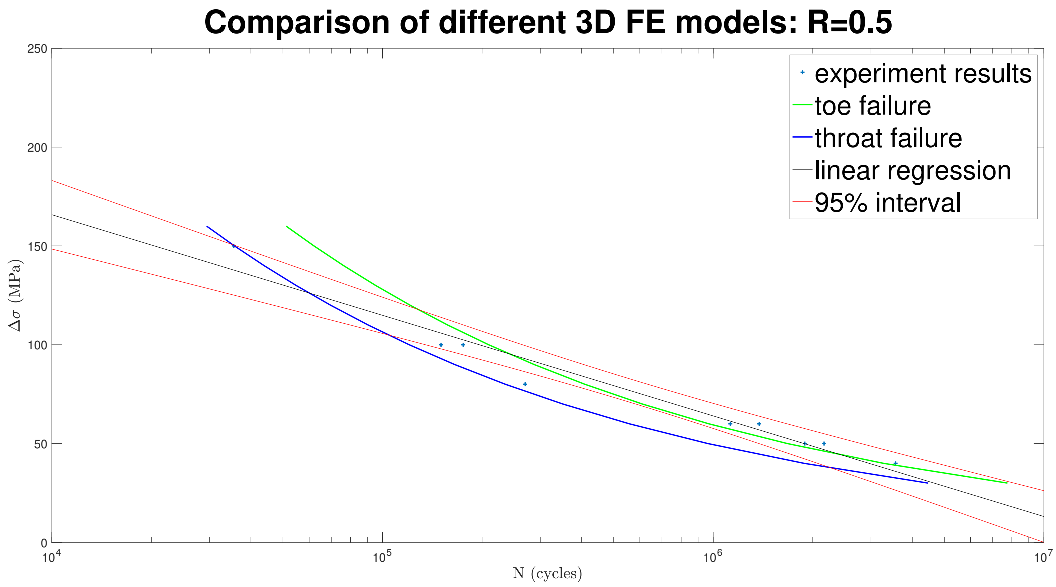

Figure 5.15: Case 2: comparison of the Seam Weld results with 3D modeling, R=0.5.

[52] made analyses for the mean initial crack size of some of the specimens and obtained values not far from 1 millimeter. The simulations have been performed considering this information and the results are plotted in Fig.5.18 and 5.19.

The results in Fig.5.18 and 5.19 are much better and there is a good fit for both the two curves at each ratio. The estimation based on the mean grain size seems to be at least as good as the estimation based on 4.2.54. However, this doesn't imply that the grain size is a better estimation for several reasons. First of all the mean grain size has been taken from another, similar, material and the σ_{th}^{a} has been both estimated from the ultimate tensile strength and transformed to its equivalent at another ratio R. It is also necessary to consider that this is only one case and that the data are really not enough to support this conclusion.

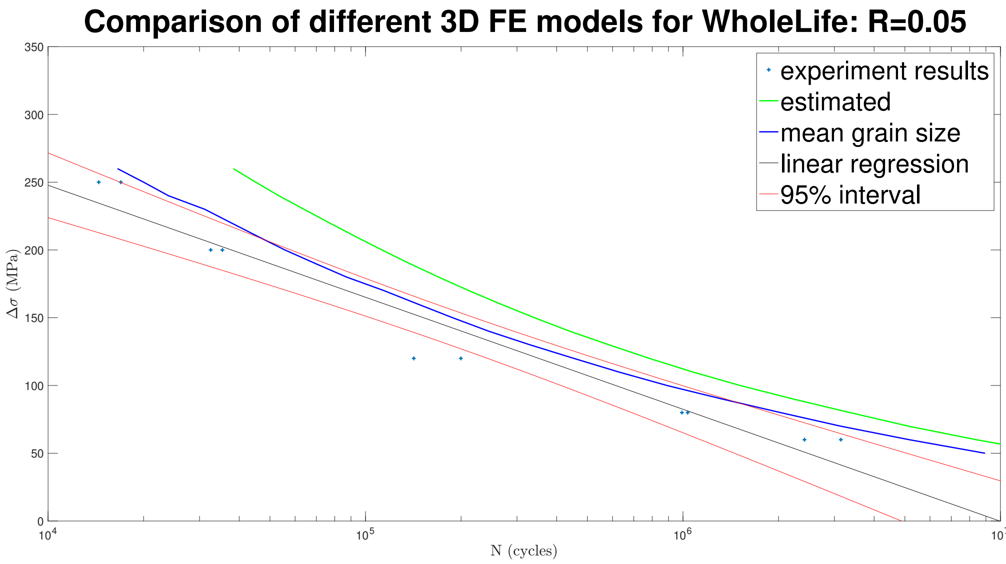

Figure 5.16: Case 2: comparison of the WholeLife results with 3D modeling, R=0.05.

5.3.3 Comparison with the Eurocode standard

As for the first case, the Eurocode's curve has been plotted against the data. In this case, only the FAT36 curve has been considered since all the failures started from the root. The data have been plotted for the nominal stress at the weld throat.

Looking at Fig.5.20, the results are in good agreement with the Eurocode's curve. Only one specimen out of nineteen falls under the design curve which results in a 94.74% rate of survival. However, the small amount of data means that the curve could be a little too much non-conservative and it is always dangerous to use such a curve in the design process. On the other hand, the 95% probability of survival curves calculated using Seam Weld are more on the safe side. Moreover, another advantage of using Seam Weld is the possibility of calculating curves for different ratios, improving predictions.

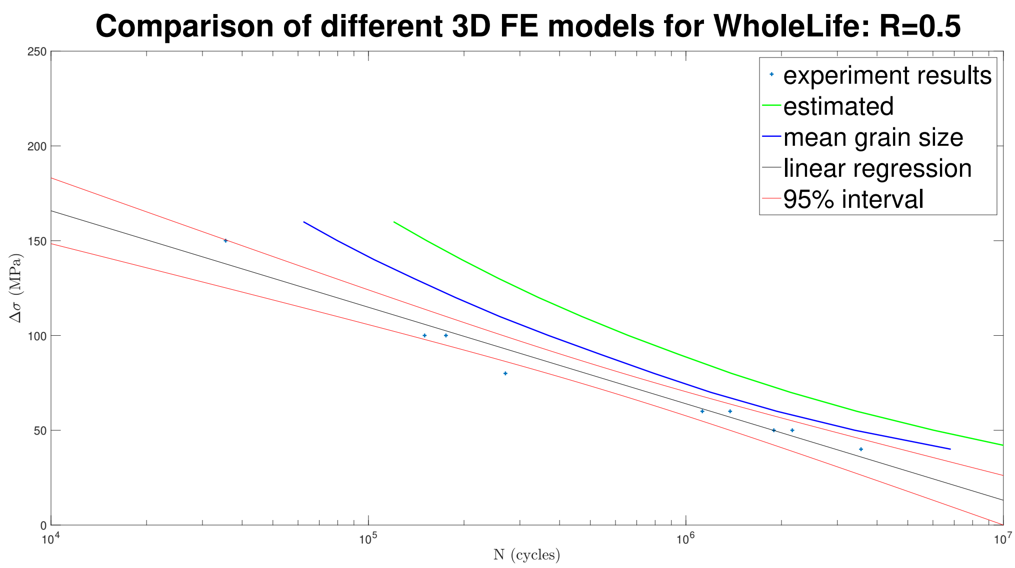

Figure 5.17: Case 2: comparison of the WholeLife results with 3D modeling, R=0.5.

5.4 Case 3

As in the first two cases, the Eurocode's curves have been plotted against the data. In this case, the appropriate curves are the FAT71 for full penetration butt welds and FAT36 for partial penetration butt welds. The authors say that "magnetic particle inspection was used to detect possible weld defects", but they don't mention a specific control of the penetration of the joint. For this reason, both curves have been considered.

Fig.5.21 shows that the joints are of great quality. The partial penetration curve FAT36 is definitively too much conservative, which means that there wasn't any defect due to partial penetration. All the data fall above the FAT71 design curve and even if it seems to be a little too much conservative, it is overall a good design tool. Unfortunately, in this case it was not possible to calculate the 95% probability of survival curves using Seam Weld since the standard error of the material fatigue curve was missing.

For the third case, solid and shell Seam Weld analyses have been per-

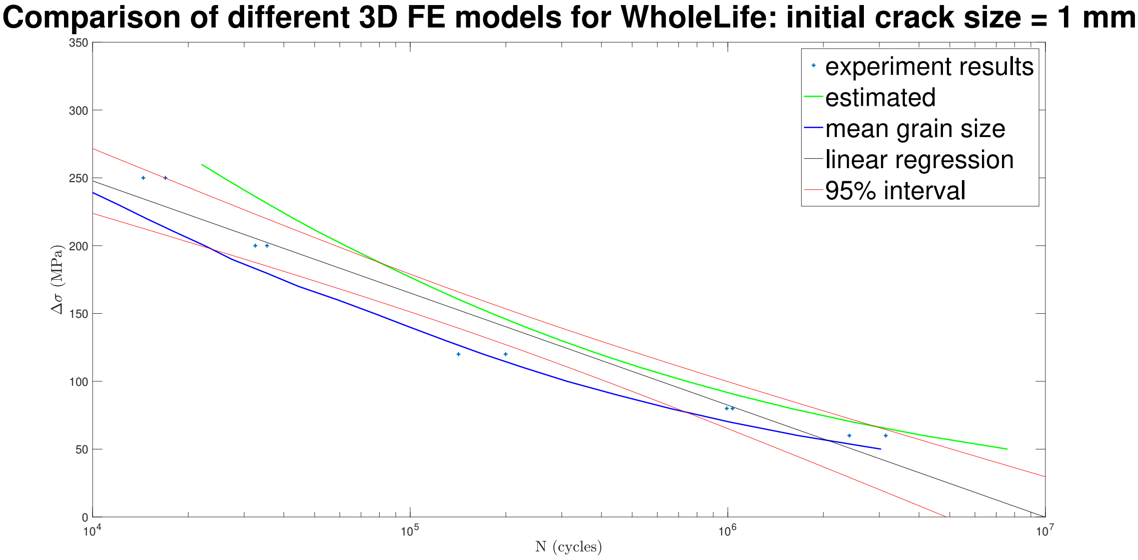

Figure 5.18: Case 2: comparison of the WholeLife results with 3D modeling, R=0.05.

formed. Starting with the solid modeling, as in case one, an analysis on the number of layers and on the depth has been done.

Looking at 5.22, it is possible to confirm that the number of layers is not too relevant, at least in these simple loading cases, and that the outputs seem to converge to a limit curve when the number of layers is increased. The same can't be said for the depth choice as shown in 5.23, where there are some differences. The 4 mm depth's curve seems to be the best one. In the literature, it is suggested to take the depth equal to the whole thickness of the plate, which is 4.5 mm, but in this case it clearly isn't the best choice. This could be happening because of strange numerical discontinuities on the back of the weld (see Fig.5.24).

For this reason, a new FE model with finer mesh has been used to perform further analyses. The results for different depths are plotted in Fig.5.25.

The output, in this case, is better and the curves for 4mm and 4.5mm almost coincide (actually, the 4.5mm curve is still slightly worse). However, looking at the model in Fig.5.26 the numerical discontinuities on the back of

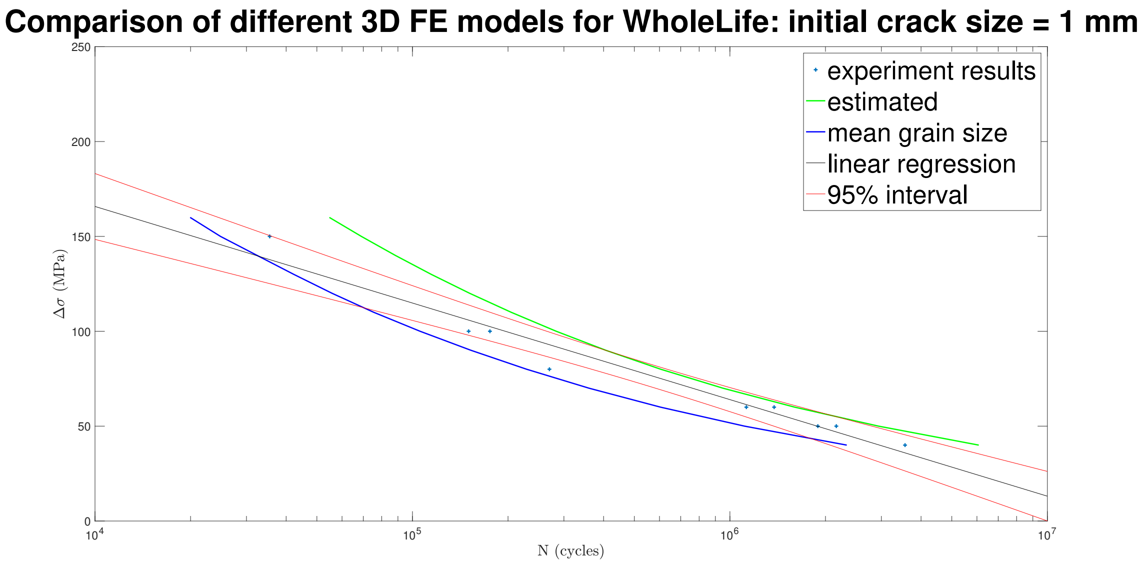

Figure 5.19: Case 2: comparison of the WholeLife results with 3D modeling, R=0.5.

the joint are still present, even if they are smaller than before.

Since improving the quality of the mesh resulted in just reducing the dimension of the numerical discontinuities, the joint has been modeled with a different approach. In these first two models, the connection between the base material and the weld has been modeled artificially, imposing zero relative displacements between the weld and the base material. In the following models, the joint has been modeled as one piece made of two different materials. This means that the nodes between the weld and the base material are shared among the two parts. Two models with different mesh size have been used for this approach as well. The results of the depths comparison are displayed in Fig.5.27 and 5.28, while the back of the joints are shown in Fig.5.29 and 5.30.

In these cases, there aren't strange numerical discontinuities on the back of the joint and both outputs show that the best curve is the 4.5mm's one. Finally, the 4.5mm's curves for each model are displayed in Fig.5.31.

From the plot, we can see that the best approach for modeling butt joints

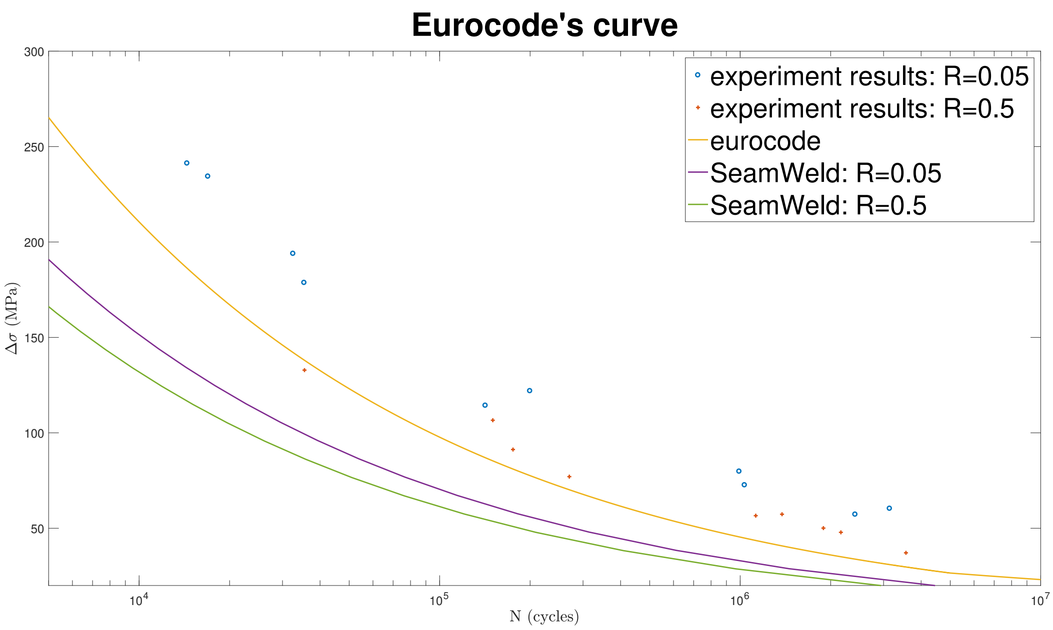

Figure 5.20: Case 2: Eurocode's curve vs the Seam Weld curves for 95% probability of survival.

is by far the second, since it provides better results with a coarse mesh and clearly retains the mesh independence of the structural stress method.
The analyses carried out in this section show not only that the literature's suggestion was right, but also how it is important to properly assess the quality of the mesh and stress profile in the critical points. Moreover, the weld should be modeled as in the second case in order to avoid strange behavior of the outputs and to retain the mesh independence of the method. In conclusion, it is better to follow the guidelines given in the literature but, in the presence of strange numerical discontinuities, it is reasonable to choose a more shallow depth if further analyses can't be done.

The shell and solid results are compared against the experimental data in Fig.5.32. The solid results are satisfactory, but the shell curve is not bad as well. Indeed, it is surprisingly good for a simple two-dimensional model. This is due to the fact that the plate's thickness is only 4.5mm versus the

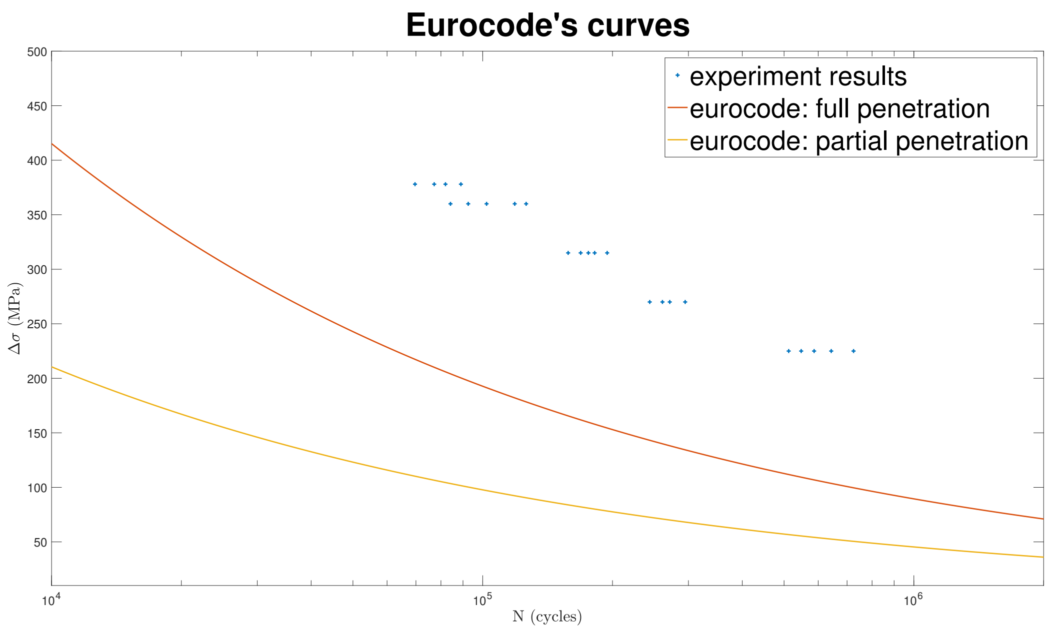

Figure 5.21: Case 3: Eurocode's curve.

12mm and 10mm thicknesses of the previous cases. For this reason, the shell model should be used whenever the thickness of the specimen is not too big in order to improve the speed of both the FE and the fatigue analyses.

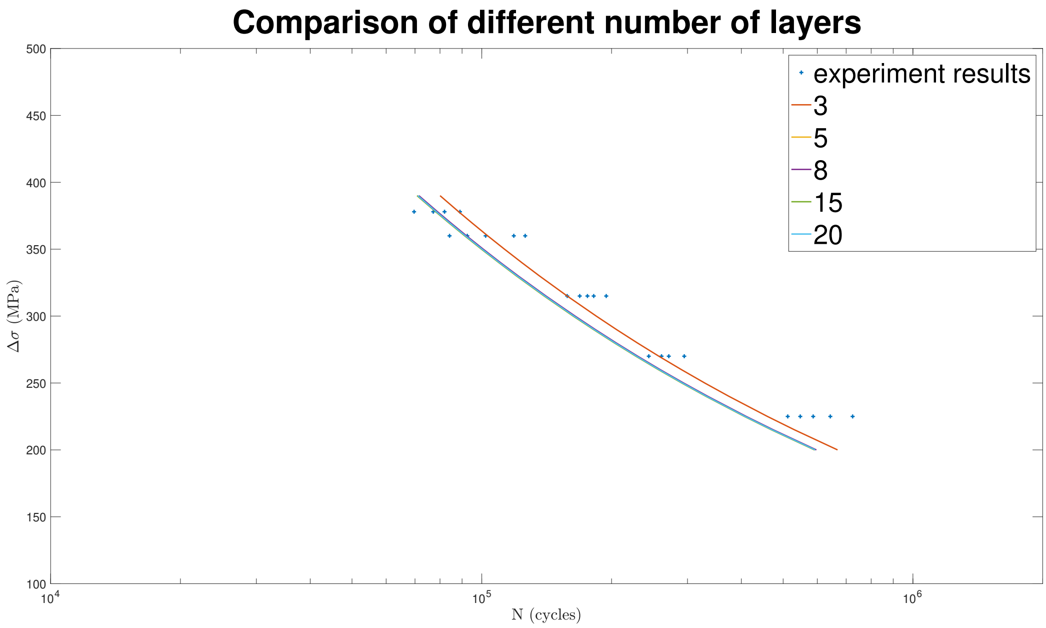

Figure 5.22: Case 3: comparison of the Seam Weld results for different number of layers.

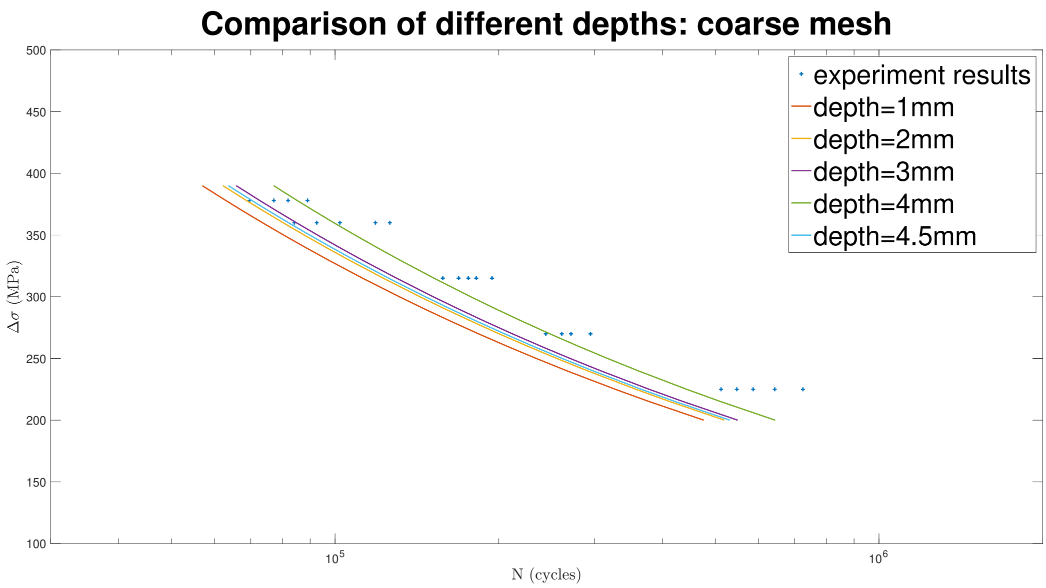

Figure 5.23: Case 3: comparison of the Seam Weld results for different depths.

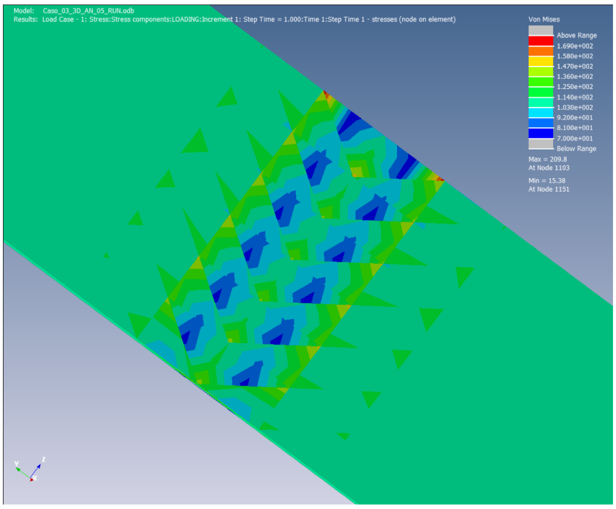

Figure 5.24: Case 3: strange numerical discontinuities on the mesh.

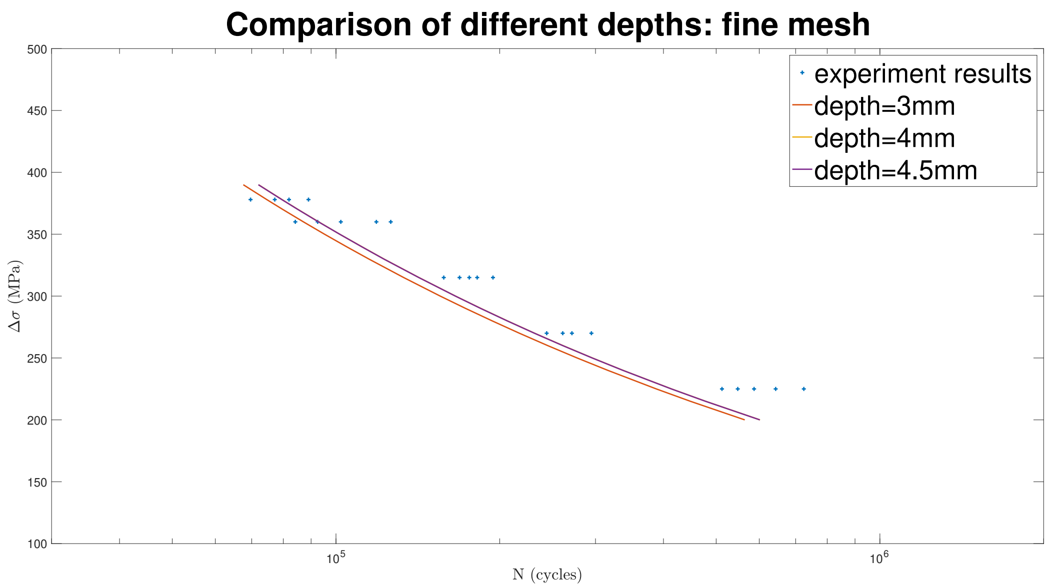

Figure 5.25: Case 3: comparison of the Seam Weld results for different depths, finer mesh.

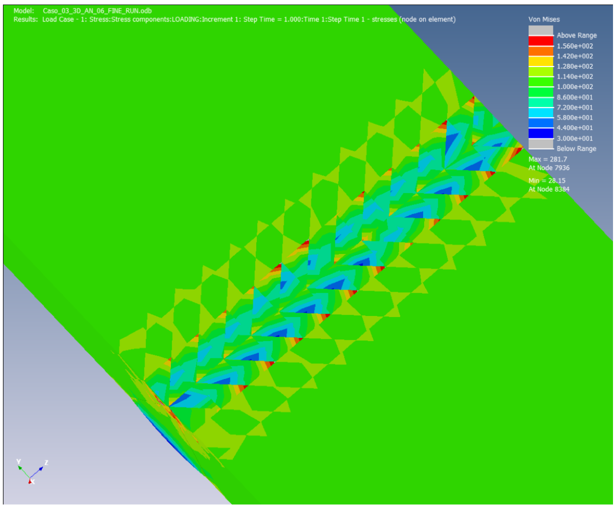

Figure 5.26: Case 3: numerical discontinuities on the mesh, fine mesh.

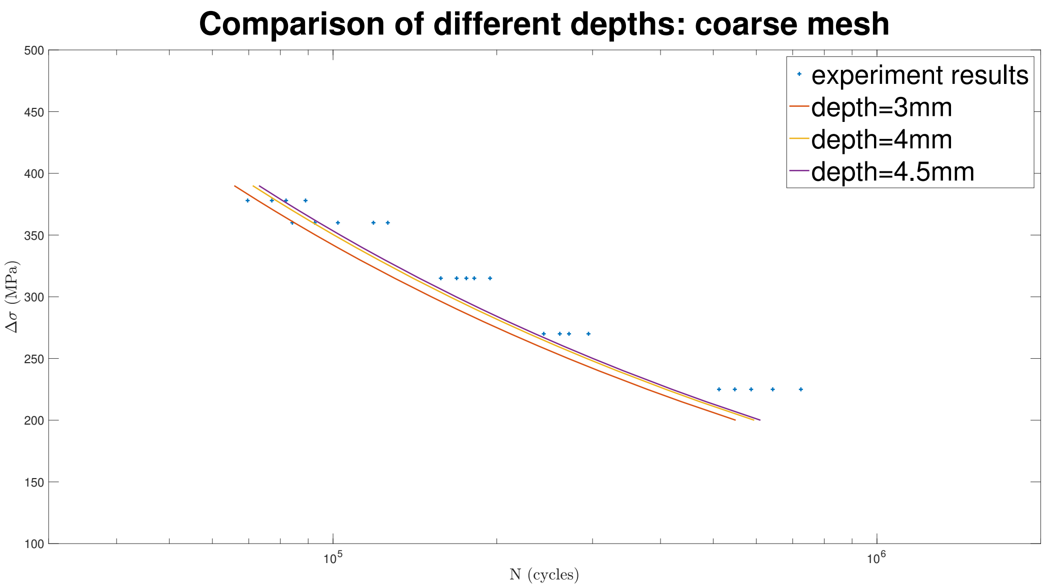

Figure 5.27: Case 3: comparison of the Seam Weld results for different depths, second approach, coarse mesh.

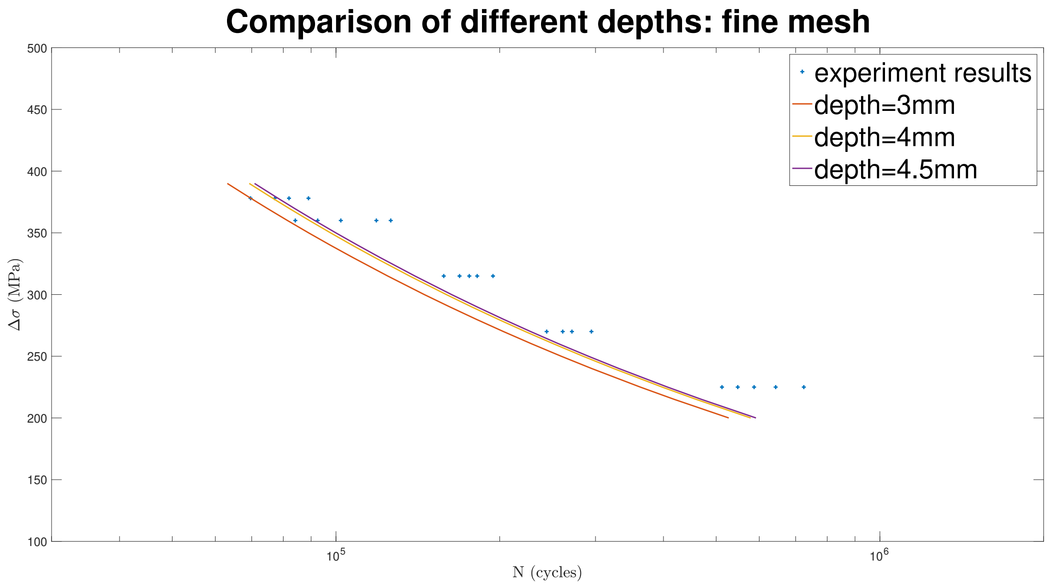

Figure 5.28: Case 3: comparison of the Seam Weld results for different depths, second approach, fine mesh.

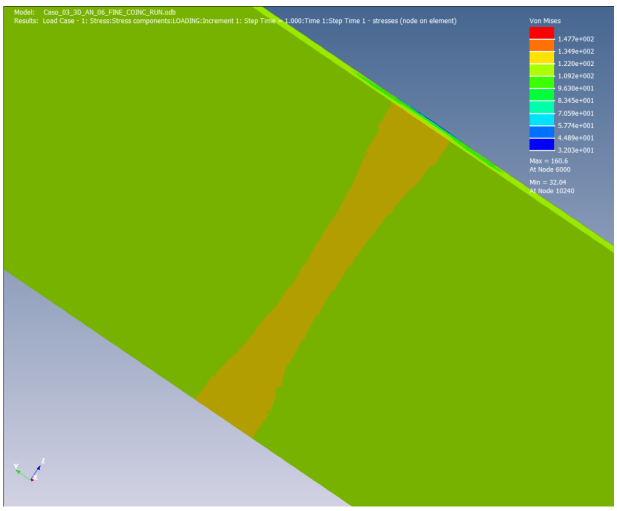

Figure 5.29: Case 3: absence of numerical discontinuities on the mesh, second approach, coarse mesh.

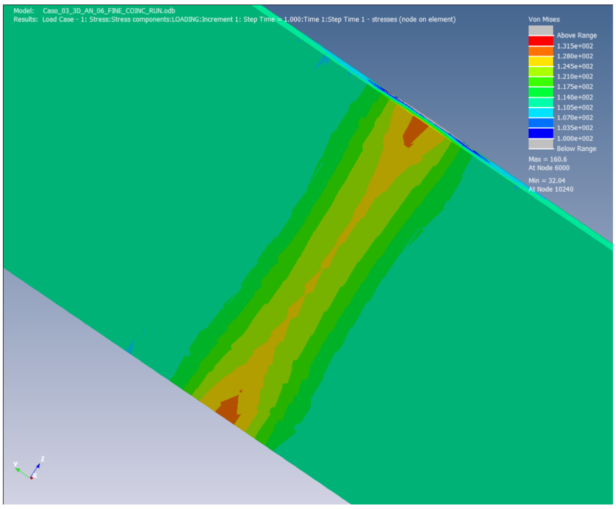

Figure 5.30: Case 3: absence of numerical discontinuities on the mesh, second approach, fine mesh.

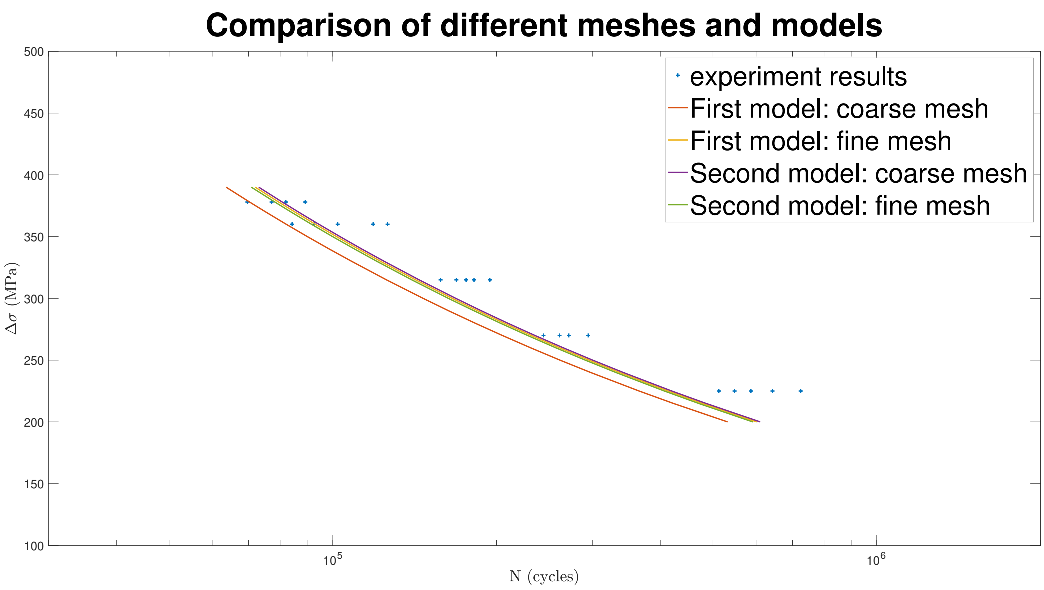

Figure 5.31: Case 3: comparison of different models.

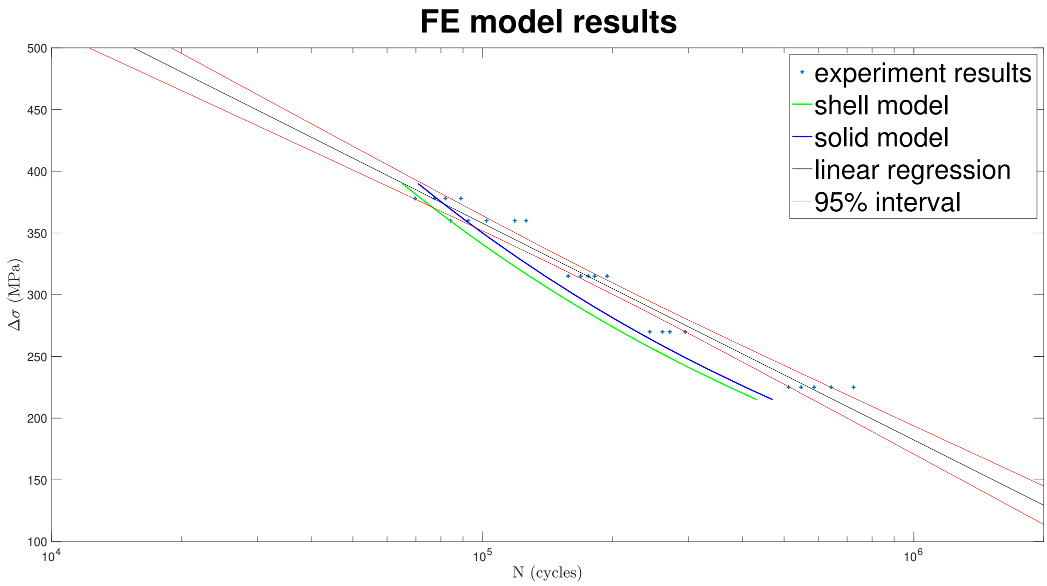

Figure 5.32: Case 3: shell and solid modeling results.

Chapter 6

Conclusions

Fatigue is a complex, though fascinating, phenomenon and there are still a lot of concepts that are not entirely clear and understood. Many models exist in literature and most of them are based on the methods illustrated in chapter two. There aren't many well-known and diffused commercial software in this field as for Finite Elements or Finite Volumes analysis and many companies have their "home-made" fatigue routines. These facts are linked to the complexity of the phenomenon and to the variety of possible approaches to it.
Welds retain a particular spot in the fatigue field for their peculiar characteristics due to the welding process and for their wide application in industry. For these reasons, particular methodologies have been developed for the fatigue analysis of weld joints and special guidelines are given in the literature (e.g. Eurocode 3 [49] and IIW [4], [31]).
In this thesis, DesignLife, provided in the nCode software suite, has been used to perform predictions for welded joints with different approaches. It has been seen that, at least for simple tensile stress, there are various possible solutions. The first one is to use a "structural stress-based" approach implemented in a glyph called Seam Weld. Following this idea, the FE model can be made of both shell and solid elements. It has been shown that the solid models always give better results than the shell ones, but also that the shell models are a good compromise between a fast analysis and an accurate

one, especially when the joint is thin.
From the analyses carried out, there seems to be no difference between modeling the cruciform joint using one or two rows of shell elements, but it would be interesting to see if this is true for bending loading as well.
Since the structural stress methods should not be so much mesh dependent, an analysis with two different meshes has also been carried out. In the first case, the solid Seam Weld method has shown similar results for coarse and fine meshes, but it is still possible to notice some differences between the two models, with the finer grid model being always more conservative. The ratio between the number of elements in the two cases is $r_e \simeq 7.2$ while the mean ratio between the coarse and fine mesh results are $r_n \simeq 1.24$ and $r_o \simeq 1.40$ respectively for the nominal and the offset case. However, in the third case, it has been shown that the mesh independence is lost because of the improper modeling of the joint and that the joint should be modeled as one piece made of two different materials.
Analyses on the possible set-ups for the Seam Weld glyph in the solid case have been performed. In particular, a study on the number of layers and on the depth in the plate thickness used for the calculation of the structural stress has been made. The outputs converge to a limit curve as the number of layers is increased and in both the first and the third case, a good convergence is reached for more than three layers. Regarding the depth choice, literature's suggestions should be followed in general. Again, the joint should be modeled as one piece in order to avoid numerical discontinuities in the FE results. Whenever this isn't possible, the mesh should be at least properly refined.
The new WholeLife method, implemented recently in DesignLife, has been used for making fatigue life's predictions. It requires three dimensional FE modeling of the component and it's in many ways similar to a crack growth model. It is though very slow, at least compared to Seam Weld, so it needs preliminary individuation of the hot spots which can be done through Seam Weld. This method has shown to have impressive capabilities, but at the

same time some liabilities. If properly set up, it is capable of giving better output than Seam Weld. However, being a more complex model, it isn't that easy to find a good estimation of the parameters and it requires more knowledge of both geometry and material's properties. This isn't really anything new, it is the old compromise between a simple model, with few parameters and easier to calibrate, and a complex model, with many parameters and greater capabilities.

In this thesis, a new estimation of ρ^* has been proposed. In particular, besides one of the methods proposed in [44], the mean grain size of the material was taken as the ρ^* estimation. This new estimation is free from the flaws of the previous estimation and it seems to give results at least as good as 4.2.54. In general, WholeLife always gave results comparable to or better than the solid Seam Weld case. Since the inputs were all based on similar materials' properties or on empirical formulae, it is reasonable to think that, using more precise information, the method could reveal itself to be much better than Seam Weld.

To summarize, the Seam Weld model requires little effort to be set up (especially for the shell case), while the WholeLife method requires a lot more variables to be calibrated. As in these cases it is always suggested, the more complex method should be used only when it's possible to properly estimate its parameters, otherwise it is better to use a simpler model.

Overall the methods always gave good results, even in the first case, where the Eurocode's curves couldn't be used because of the offset of the joint and, for this reason, are important design tools.

To conclude the dissertation I would like to suggest some possible further studies. It would be interesting to analyze cruciform weld joints under bending conditions in order to check the importance of the choice between one or two rows modeling and of the layers' number. It would also be important to assess the capability of the models for more complicated geometries and loading conditions (e.g. with duty cycles and/or with multiaxial loading conditions). Regarding the first case, an interesting analysis would be the

comparison of the fatigue life's curves for different offsets. This study could also bring some clarity to the reason for the data's sparsity.
Finally, since in this thesis the mean grain size has been proposed as an estimation of ρ^* with moderate success, it would be important to understand how much this estimation is reliable when compared to the methods proposed in [44].

Chapter 7

Appendix: the meaning of $\frac{da}{dN}$

The main equation of each Crack Growth model is a law of the type:

$$\frac{da}{dN} = f(K) \tag{7.0.1}$$

where f is a function of the stress intensity factor and $\frac{da}{dN}$ represents the velocity at which the crack propagates. However, from a mathematical perspective, the expression $\frac{da}{dN}$ makes no sense since $N \in \mathbb{N}$. In order to understand the meaning of $\frac{da}{dN}$ we have to look at how the crack growth plots are generated. In fact, the results from the tests are usually plotted in a $N \times a$ plot. The data are fitted with a regression curve and the derivative of that curve is called $\frac{da}{dN}$ 7.1 (there are many numerical approaches for obtaining $\frac{da}{dN}$ such as the spline fitting method and the incremental polynomial method [24]).

The expression "$\frac{da}{dN}$" should not be thought of as the derivative of the crack length a with respect to the number of cycles N, but just as a measure of the velocity at which the crack propagates: "the crack growth rate". The notation is not rigorous from a mathematical point of view, but it is rooted in the crack growth theory and all the books and the articles I've seen so far utilize it. For this reason, I utilized it as well.

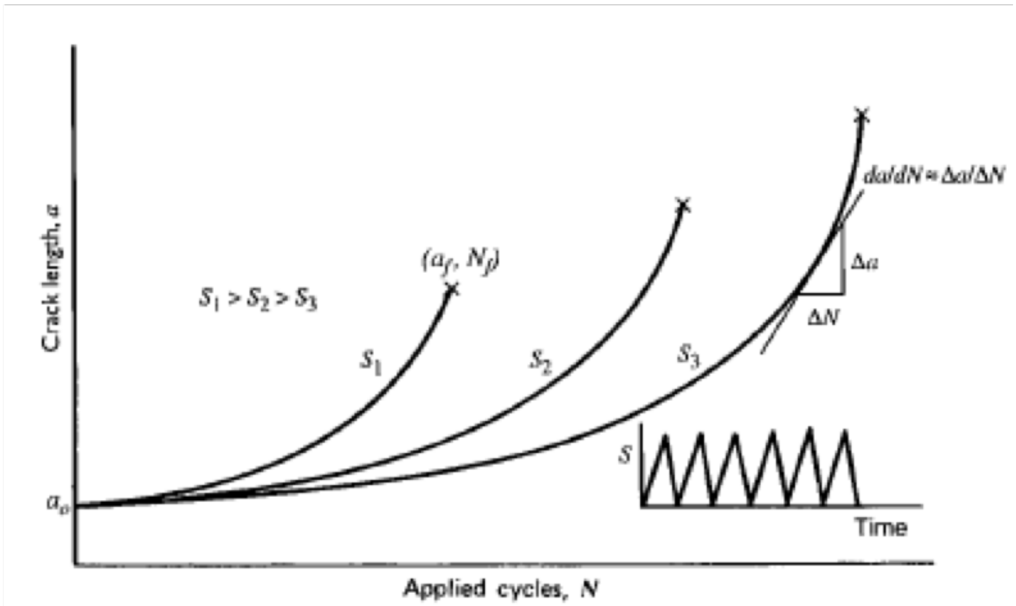

Figure 7.1: Fatigue crack length versus applied cycles. Fracture is indicated by the x (Picture by [10]).

Chapter 8

Appendix: FE models

In this appendix, all the FE models are summarized. For each case, both the geometry and the grid are shown. In addition, the results of the linear elastic analyses are included. All the analyses have been carried out by Simone Ferrero (Nova Analysis).

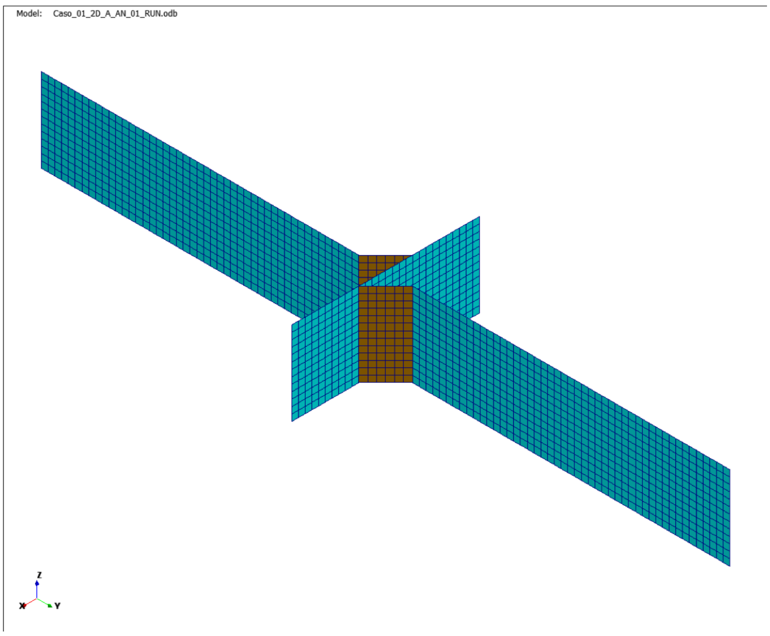

Figure 8.1: case 1, shell elements, nominal geometry, single row: mesh.

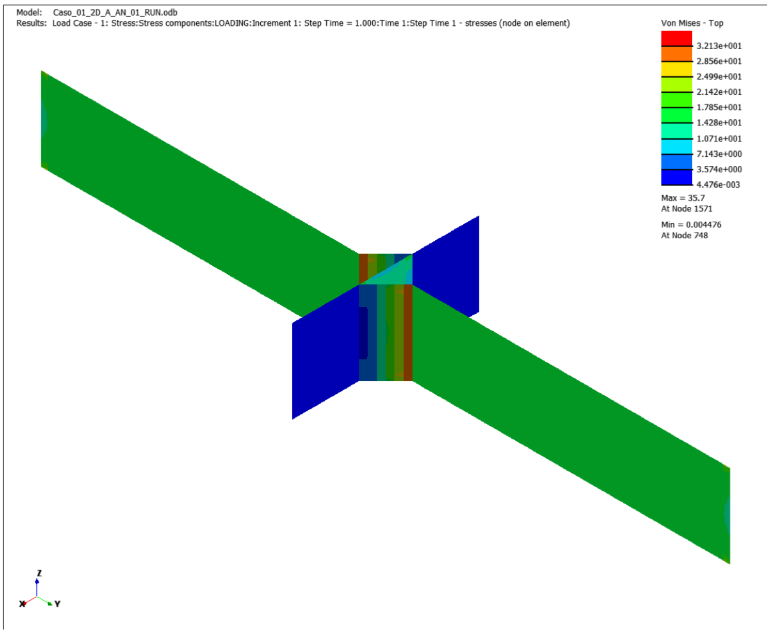

Figure 8.2: case 1, shell elements, nominal geometry, single row: FE analysis results (Von Mises stress).

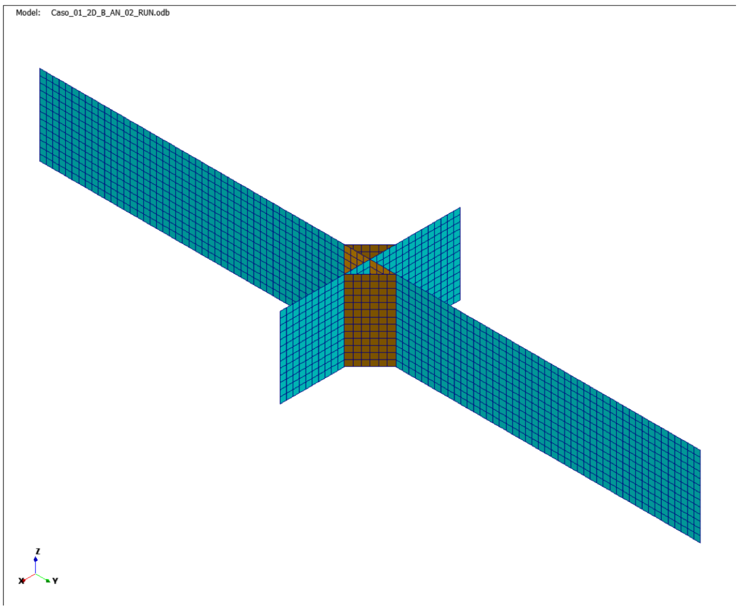

Figure 8.3: case 1, shell elements, nominal geometry, two rows: mesh.

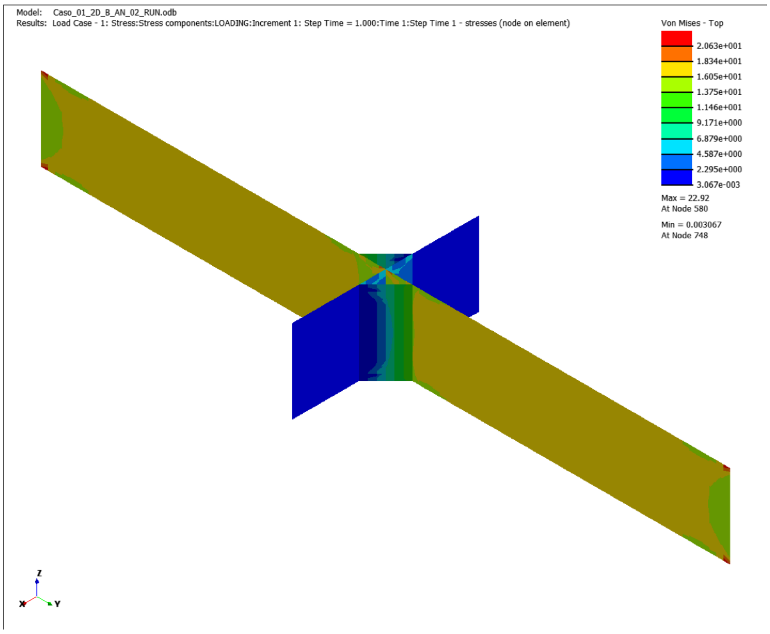

Figure 8.4: case 1, shell elements, nominal geometry, two rows: FE analysis results (Von Mises stress).

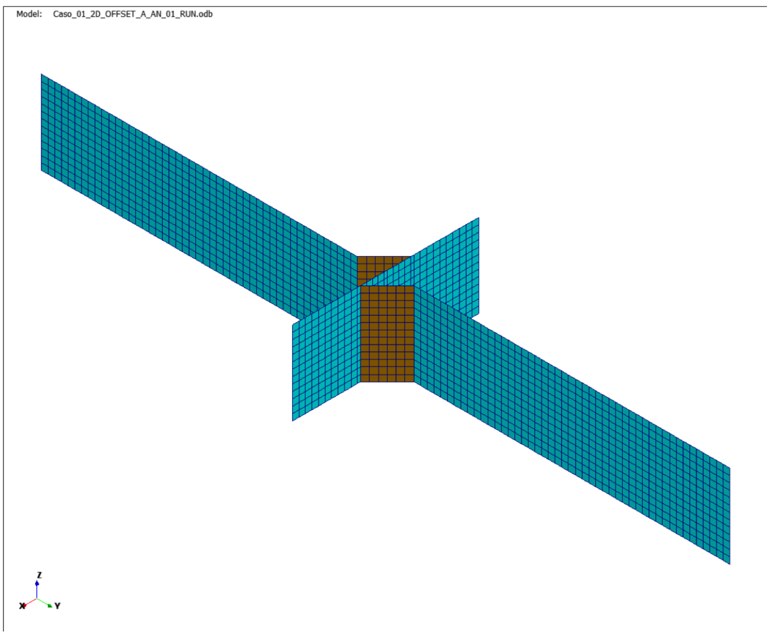

Figure 8.5: case 1, shell elements, actual mean geometry, single row: mesh.

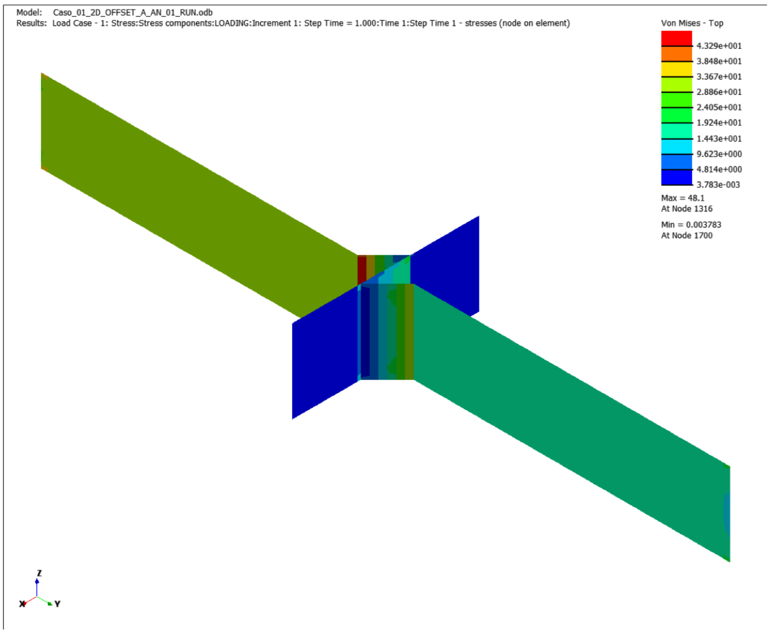

Figure 8.6: case 1, shell elements, actual mean geometry, single row: FE analysis results (Von Mises stress).

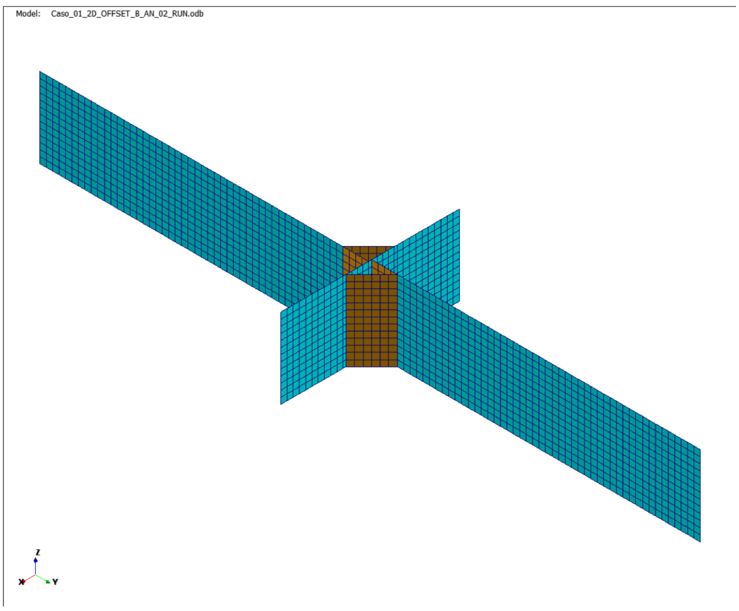

Figure 8.7: case 1, shell elements, actual mean geometry, two rows: mesh.

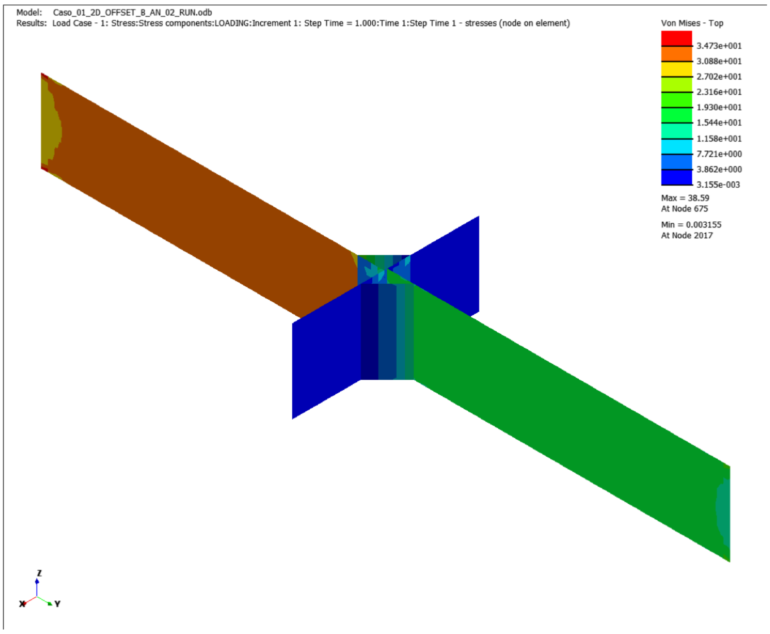

Figure 8.8: case 1, shell elements, actual mean geometry, two rows: FE analysis results (Von Mises stress).

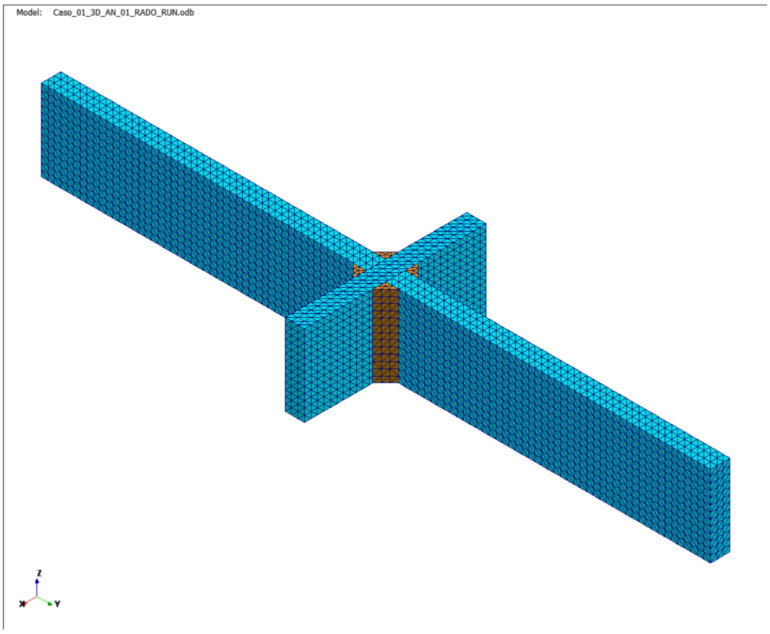

Figure 8.9: case 1, solid elements, nominal geometry, coarse mesh: mesh.

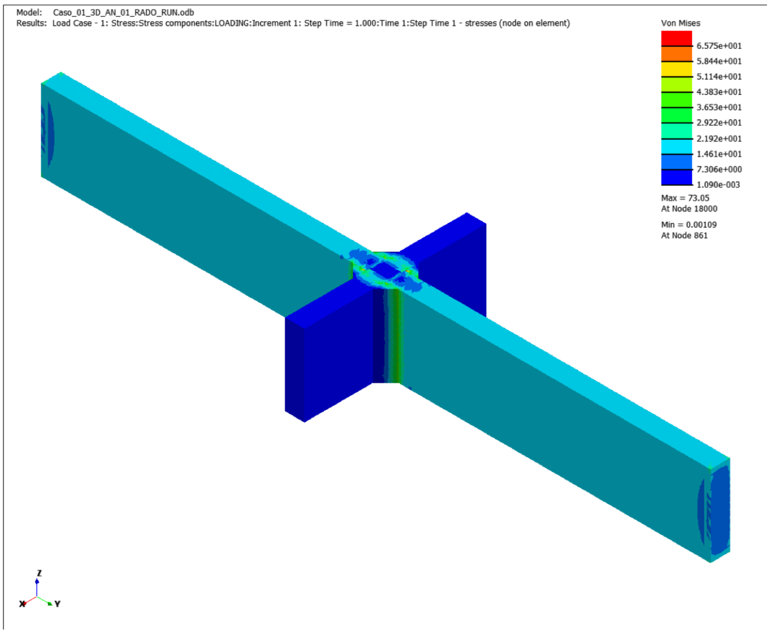

Figure 8.10: case 1, solid elements, nominal geometry, coarse mesh: FE analysis results (Von Mises stress).

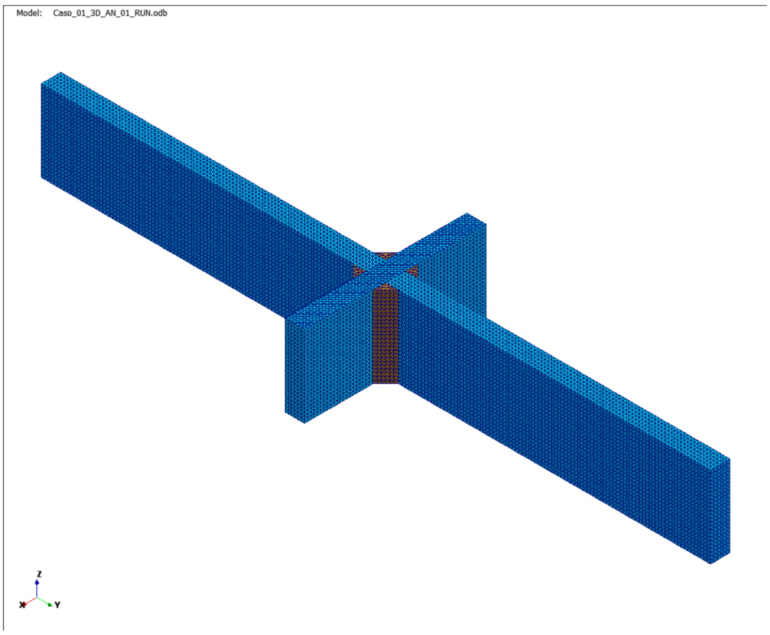

Figure 8.11: case 1, solid elements, nominal geometry, fine mesh: mesh.

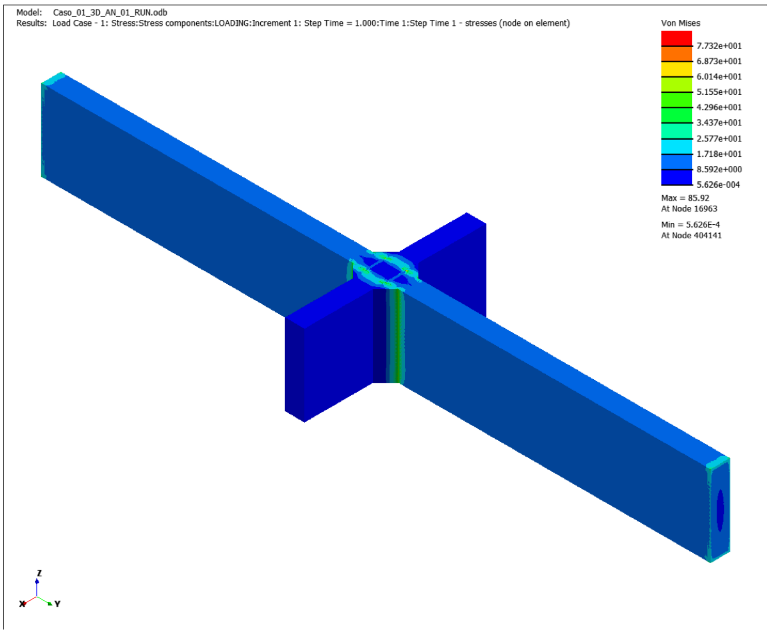

Figure 8.12: case 1, solid elements, nominal geometry, fine mesh: FE analysis results (Von Mises stress).

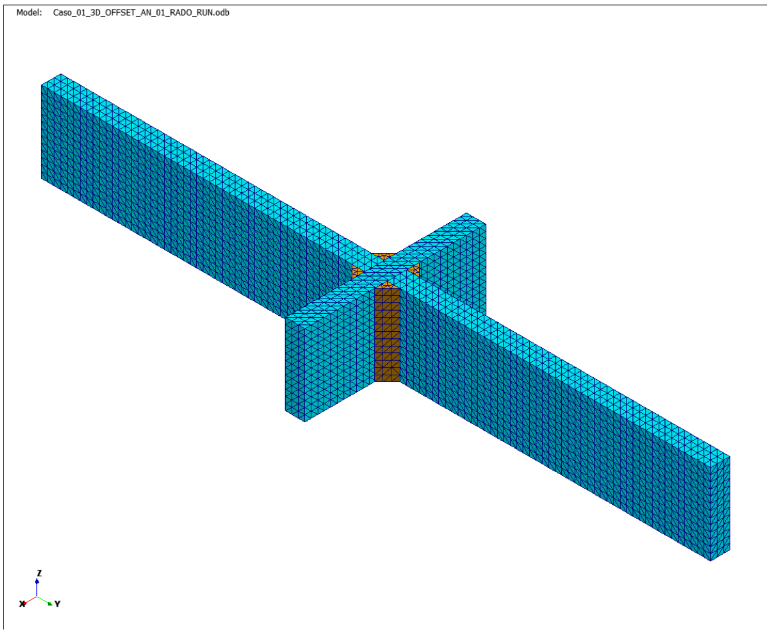

Figure 8.13: case 1, solid elements, actual mean geometry, coarse mesh: mesh.

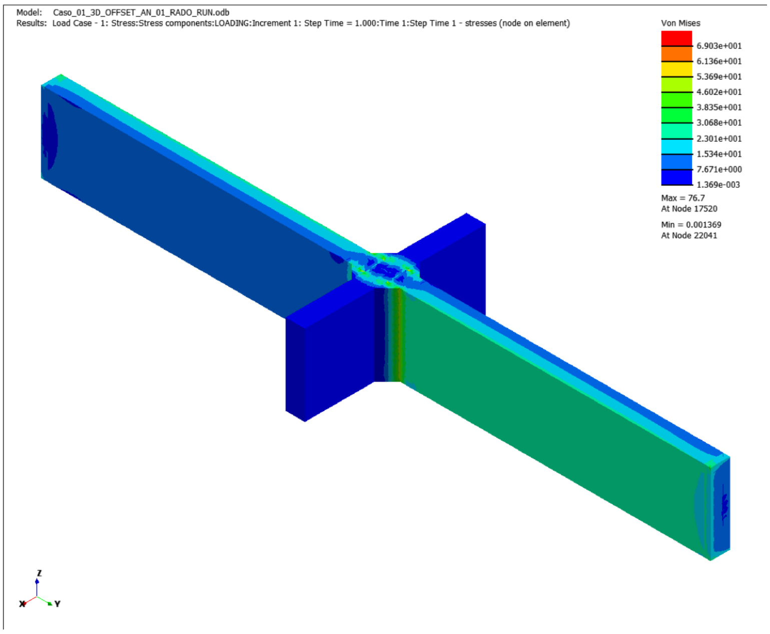

Figure 8.14: case 1, solid elements, actual mean geometry, coarse mesh: FE analysis results (Von Mises stress).

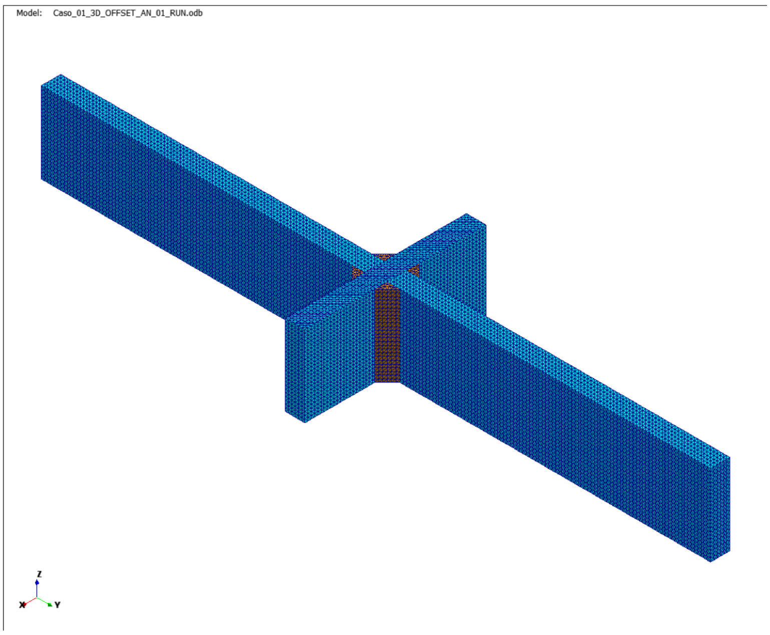

Figure 8.15: case 1, solid elements, actual mean geometry, fine mesh: mesh.

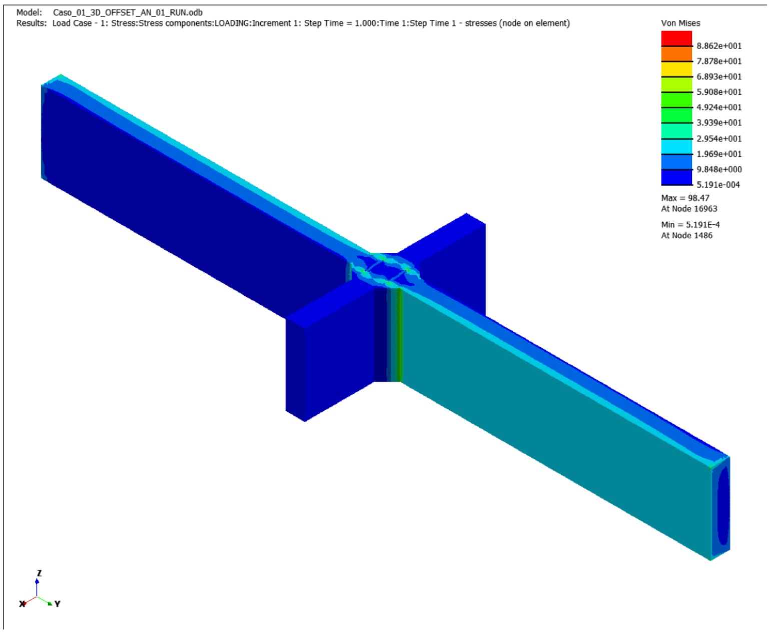

Figure 8.16: case 1, solid elements, actual mean geometry, fine mesh: FE analysis results (Von Mises stress).

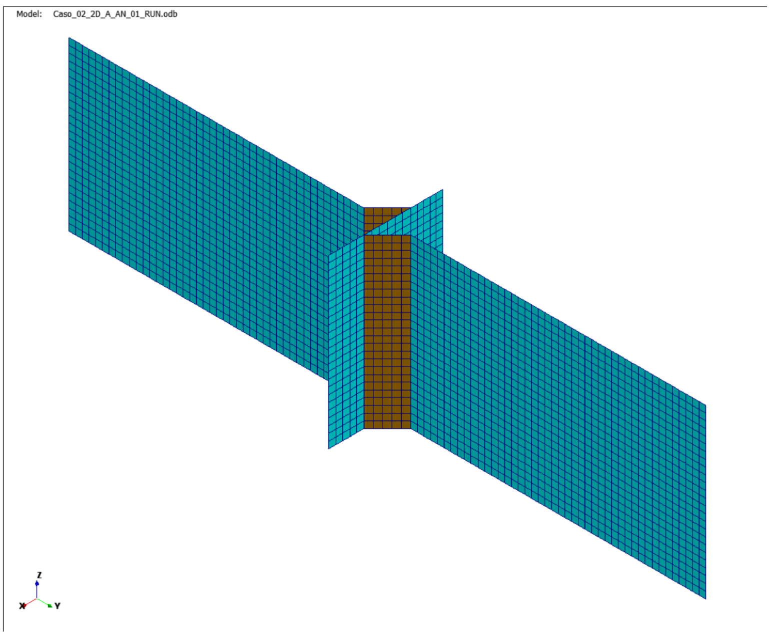

Figure 8.17: case 2, shell elements, single row: mesh.

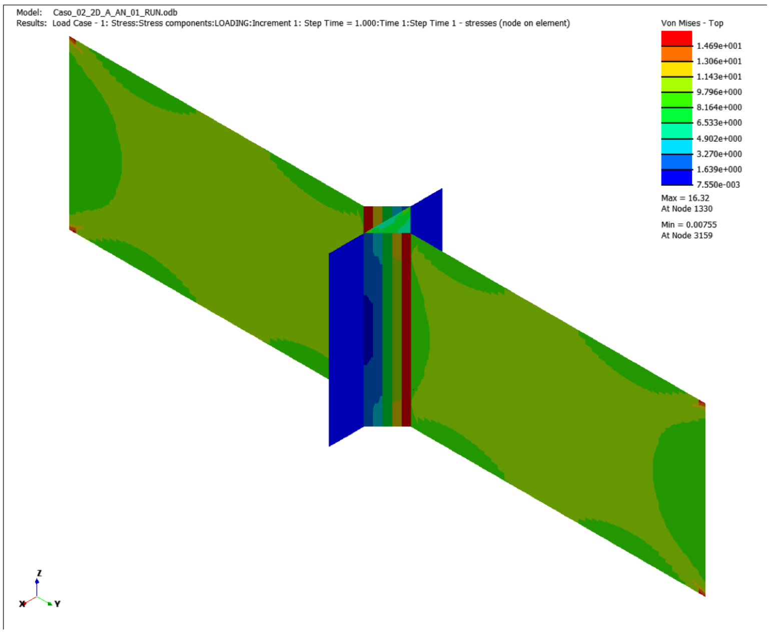

Figure 8.18: case 2, shell elements, single row: FE analysis results (Von Mises stress).

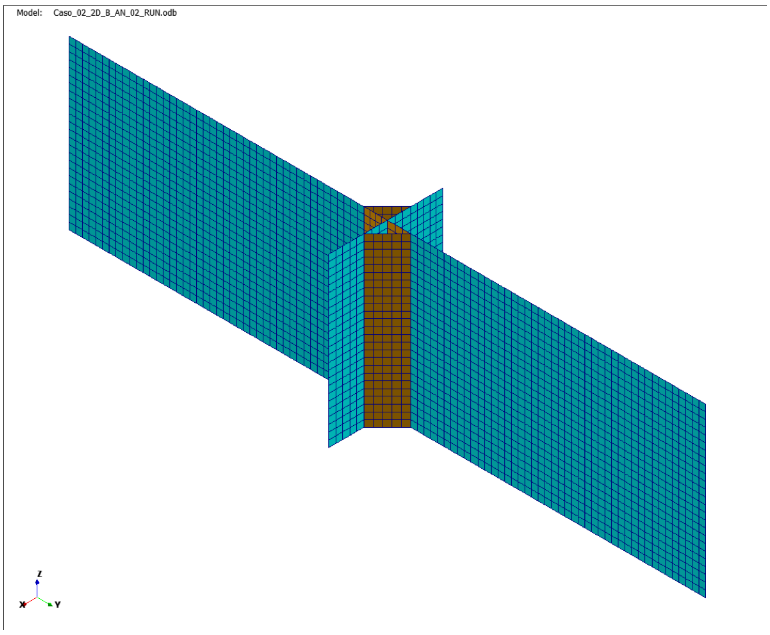

Figure 8.19: case 2, shell elements, two rows: mesh.

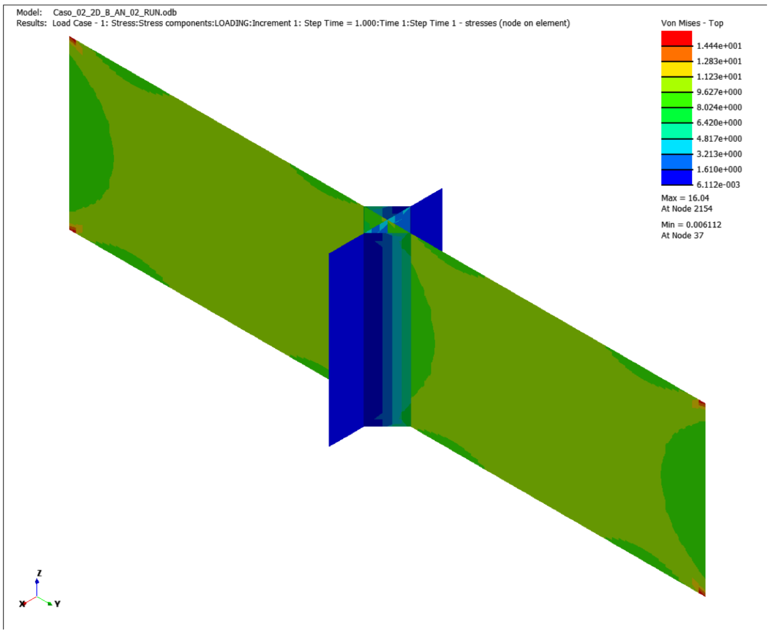

Figure 8.20: case 2, shell elements, two rows: FE analysis results (Von Mises stress).

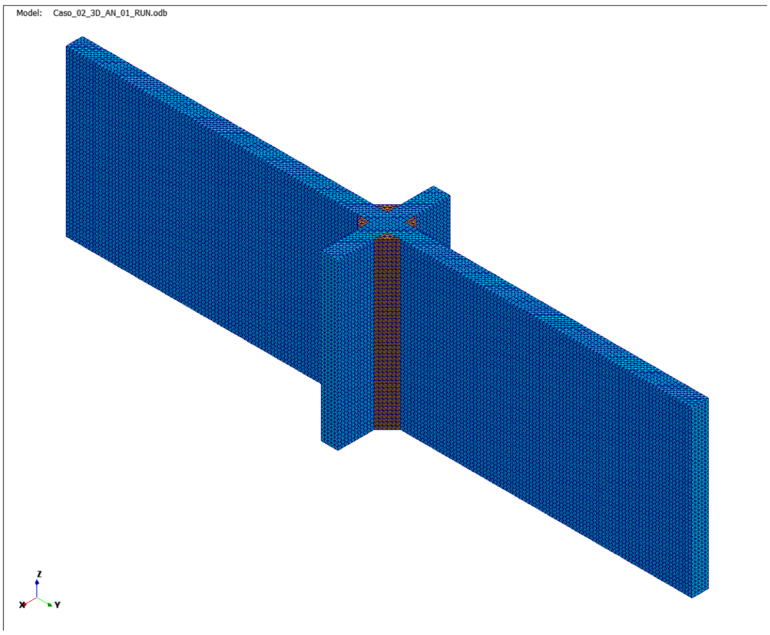

Figure 8.21: case 2, solid elements: mesh.

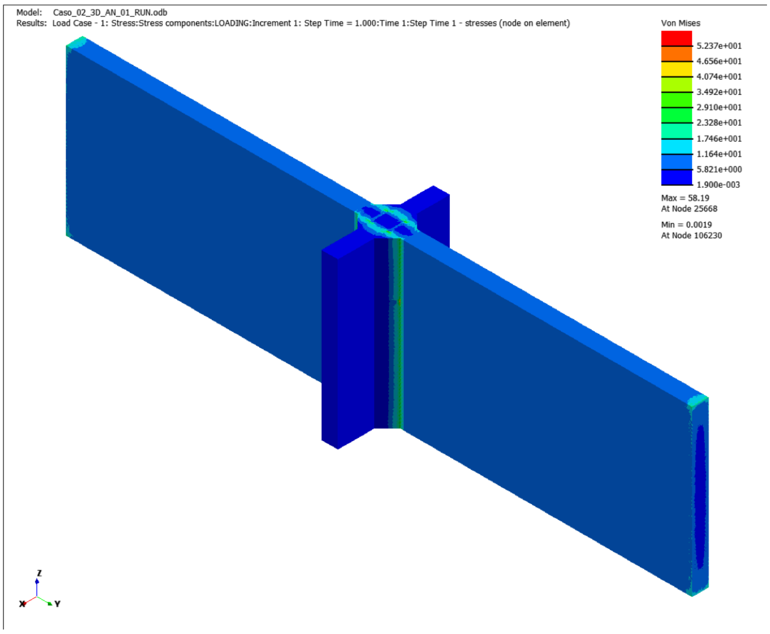

Figure 8.22: case 2, solid elements: FE analysis results (Von Mises stress).

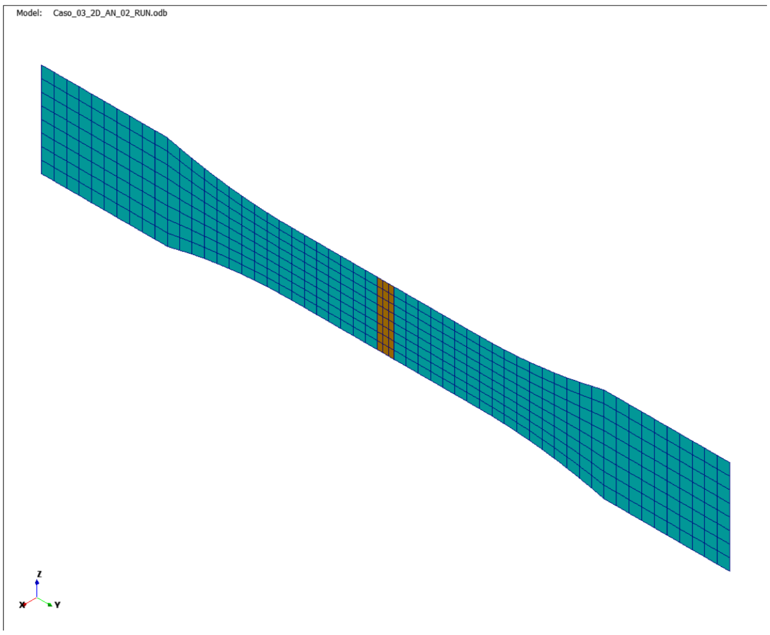

Figure 8.23: case 3, shell elements: mesh.

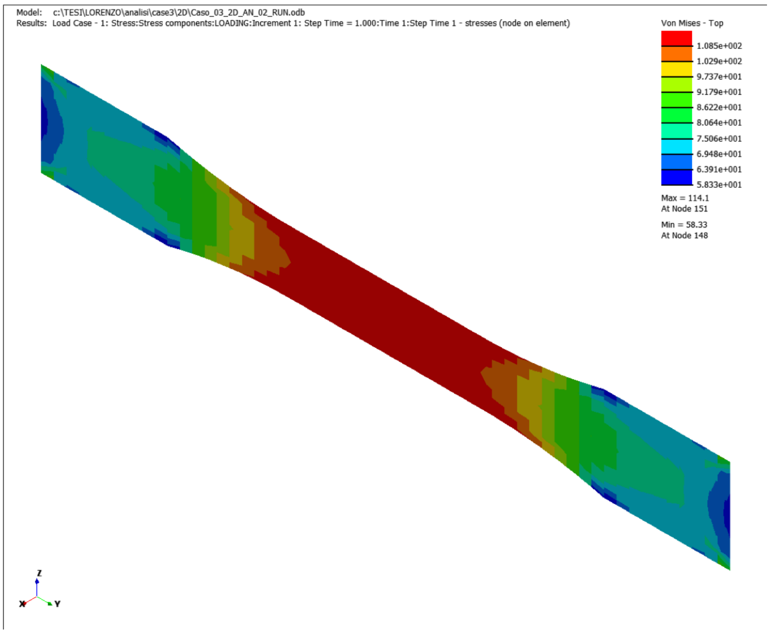

Figure 8.24: case 3, shell elements: FE analysis results (Von Mises stress).

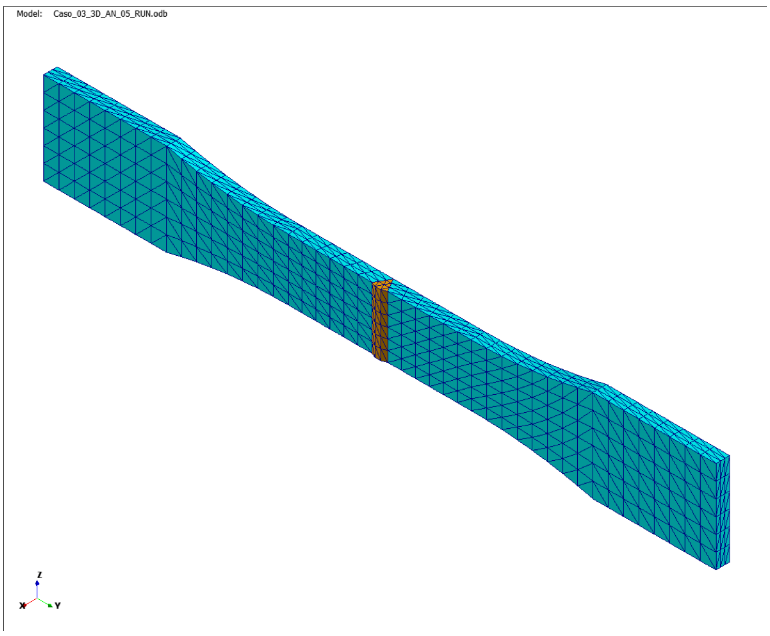

Figure 8.25: case 3, solid elements, first model, coarse mesh: mesh.

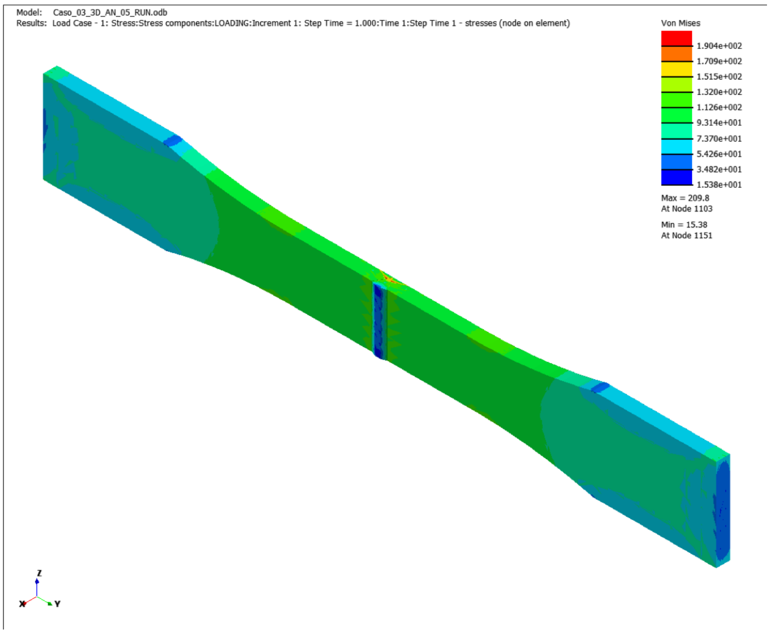

Figure 8.26: case 3, solid elements, first model, coarse mesh: FE analysis results (Von Mises stress).

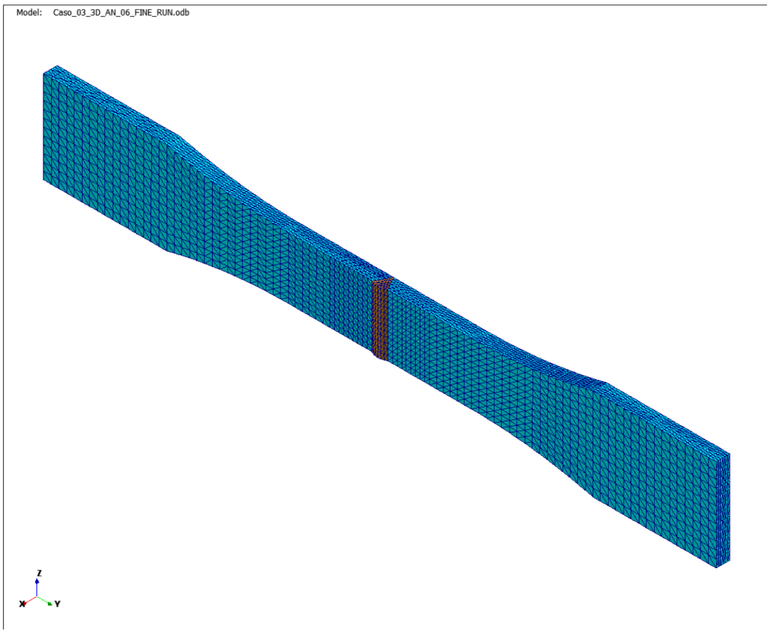

Figure 8.27: case 3, solid elements, first model, fine mesh: mesh.

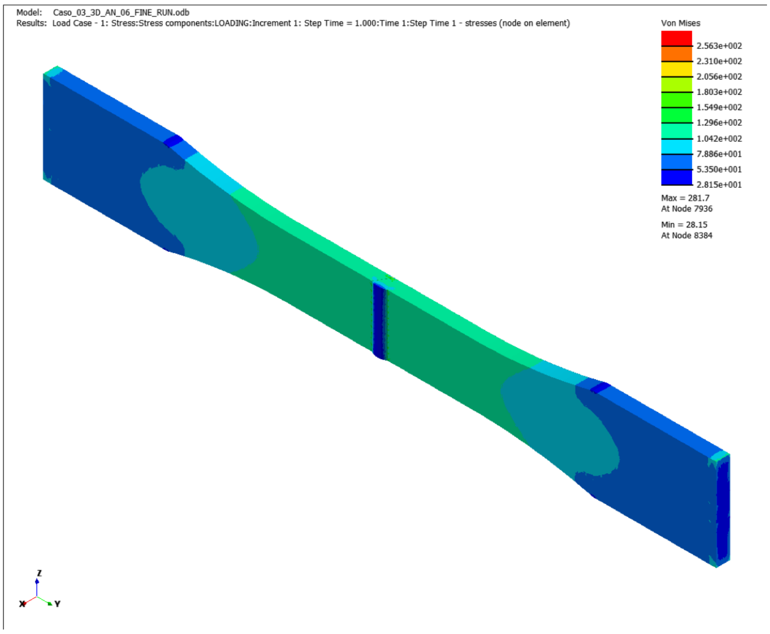

Figure 8.28: case 3, solid elements, first model, fine mesh: FE analysis results (Von Mises stress).

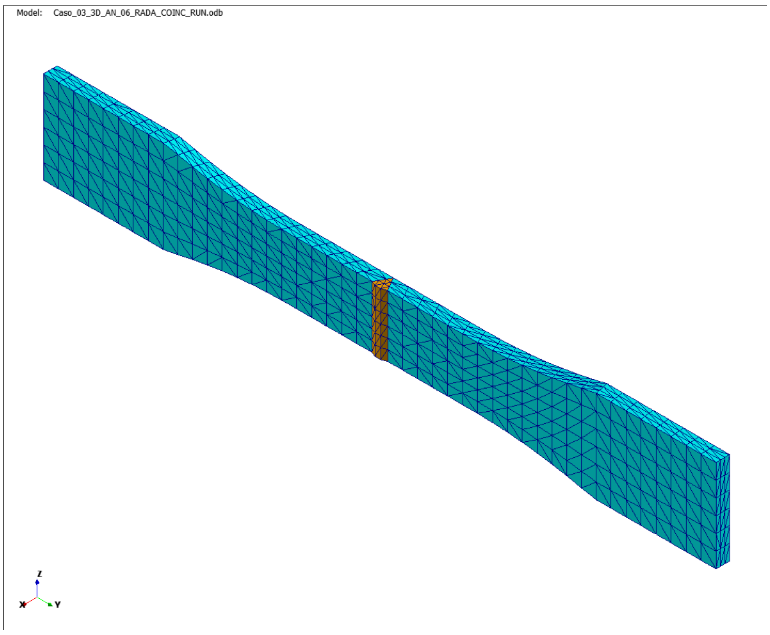

Figure 8.29: case 3, solid elements, second model, coarse mesh: mesh.

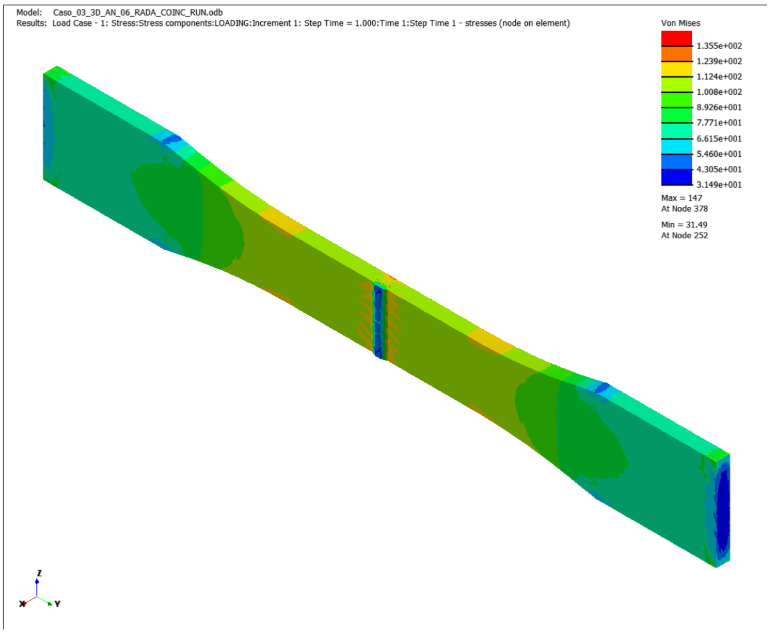

Figure 8.30: case 3, solid elements, second model, coarse mesh: FE analysis results (Von Mises stress).

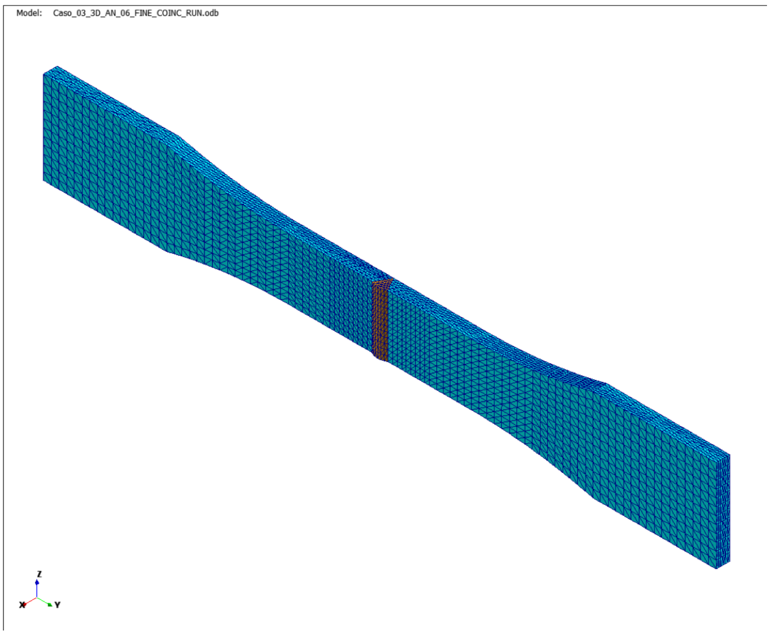

Figure 8.31: case 3, solid elements, second model, fine mesh: mesh.

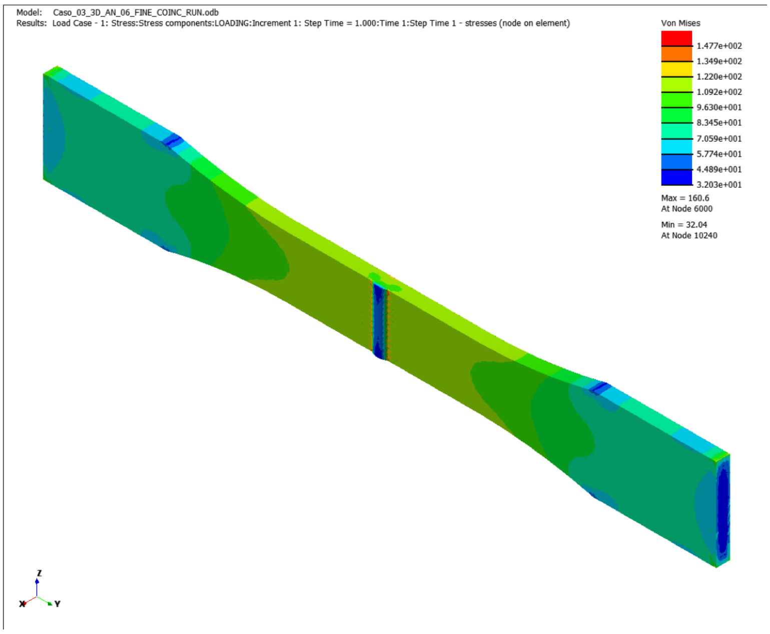

Figure 8.32: case 3, solid elements, second model, fine mesh: FE analysis results (Von Mises stress).

Bibliography

[1] Jaime Tupiassú Pinho de Castro, Marco Antonio Meggiolaro: *Fatigue Design Techniques: Vol. I - High-Cycle Fatigue*, (2016).

[2] Jaime Tupiassú Pinho de Castro, Marco Antonio Meggiolaro: *Fatigue Design Techniques: Vol. II - Low-Cycle and Multiaxial Fatigue*, (2016).

[3] Jaime Tupiassú Pinho de Castro, Marco Antonio Meggiolaro: *Fatigue Design Techniques: Vol. III - Crack Propagation, Temperature and Statistical Effects*, (2016).

[4] International Institute of Welding: *Reccomendations for Fatigue Design of Welded Joints and Components*, (2016).

[5] HBM Prenscia: *WholeLife Fatigue Theory guide*, (2018).

[6] HBM Prenscia: *DesignLife Theory Guide*, (2018).

[7] Alfredo S. Ribeiro, José A.F.O. Correia, António L.L. Silva, Abilío M. P. de Jesus: *Evolution of Fatigue History*, Congresso Brasileiro de Engenharia Mecânica, Natal, Brasil, (2011).

[8] S. Suresh: *Fatigue of Materials: 2nd edition*, Cambridge University Press, (1998).

[9] Ministry of Transport and Civil Aviation: *Civil Aircraft Accident: Report of the Court of Inquiry into the Accidents to Comet G-ALYP on 10th January, 1954 and Comet G-ALYY on 8th April, 1954*, (1955).

[10] Ralph I. Stephens, Ali Fatemi, Robert R. Stephens, Henry O. Fuchs: *Metal Fatigue in Engineering: 2nd edition*, John Wiley & Sons, (1998).

[11] HBM Prenscia: *DesignLife User Guide*, (2018).

[12] Brian Reiling (Endeavor Analysis), George Laird (Predictive Engineering): *Fatigue Essentials: Stress-Life Made Easy* , (2013).

[13] MILLER Electric Manufacturing Co.: *Welding And The World Of Metals*, Woodhead Publishing, (2018).

[14] S. E. Hughes: *A Quick Guide to Welding and Weld Inspection*, Woodhead Publishing, (2009).

[15] Eugene A. Avallone, Theodore Baumeister III, Ali M. Sadegh: *Marks' Standard Handbook for Mechanical Engineers: 11th edition*, McGraw-Hill Education, (2006).

[16] Caiyan Deng, Yong Liu, Baoming Gong, Dongpo Wang: *Numerical implementation for fatigue assessment of butt joint improved by high frequency mechanical impact treatment: A structural hot spot stress approach*, International Journal of Fatigue, Vol. 92, p. 211-219, (2016).

[17] `https://www.efatigue.com`

[18] Ibrahim Al Zamzami, Luca Susmel: *On the accuracy of nominal, structural, and local stress based approaches in designing aluminium welded joints against fatigue*, International Journal of Fatigue, Vol. 101, p. 137-158, (2016).

[19] M. Matsuishi, T. Endo: *Fatigue of Metals Subjected to Varying Stresses*, Japan Soc Mech Eng, (1968).

[20] ASTM E 1049: *Practices for Cycle Counting in Fatigue Analysis*, ASTM Standards v.03.02.

[21] K. Molski, G. Glinka: *A Method of Elastic-Plastic Stress and Strain Calculation at a Notch Root*, Materials Science and Engineering, Vol.50, p. 93-100, (1981).

[22] Sadananda, Kuntimaddi & Vasudevan, A.K.: *Crack growth behavior of 4340 steel under corrosion and corrosion fatigue conditions*, Corrosion Reviews. 33. 10.1515/corrrev-2015-0034, (2015).

[23] American Welding Society: `https://awo.aws.org/`

[24] Julie A. Bannantine, Jess J. Corner, James L. Handrock: *Fundamentals of Metal Fatigue Analysis*, Prentice Hall, (1989).

[25] Tom Lassen, Naman Rècho: *Fatigue Life Analyses of Welded Structures*, Iste, (2006).

[26] Yung-Li Lee, Mark E. Barkey, Hong-Tae Kang: *Metal Fatigue Analysis Handbook: Practical Problem-solving Techniques for Computer-aided Engineering*, Butterworth-Heinemann, (2011).

[27] K. Macdonald: *Fracture and Fatigue of Welded Joints and Structures*, Woodhead Publishing, (2011).

[28] S. J. Maddox: *Fatigue Strength of Welded Structures*, Woodhead Publishing, (1991).

[29] Dieter Radaj: *Design and Analysis of Fatigue Resistant Welded Structures*, Woodhead Publishing, (1990).

[30] A. Chattopadhyay, G. Glinka, M. S. El-Zein, J. Qian, R. Formas: *Stress Analysis and Fatigue of welded structures*, Welding in the World, (2013).

[31] B. Jonsson, G. Dobmann, A.F. Hobbacher, M. Kassner, G. Marquis: *IIW Guidelines on Weld Quality in Relationship to Fatigue Strength*, Springer, (2016).

[32] American Welding Society: *Standard Welding Terms and Definitions*, (1999).

[33] K. Weman: *Welding Processes Handbook 2nd Edition*, Woodhead Publishing, (2011).

[34] Klemens Rother, Wolfgang Fricke: *Effective notch stress approach for welds having low stress concentration*, International Journal of Pressure Vessels and Piping, Vol. 147, p. 12-20, (2016)

[35] T. Holmstrand, N. Mrdjanov, Z. Barsoum, E. Åstrand: *Fatigue life assessment of improved joints welded with alternative welding techniques*, Engineering Failure Analysis, Vol. 42, p. 10-21 (2014).

[36] D. Radaj, C.M. Sonsino, W. Fricke: *Recent developments in local concepts of fatigue assessment of welded joints*, International Journal of Fatigue, Vol. 31, p. 2-11, (2009)

[37] Fricke Wolfgang: *IIW guideline for the assessment of weld root fatigue*, Welding in the World, Vol. 57, p. 753-791, (2013)

[38] D.Radaj, P.Lazzarin, F.Berto: *Generalised Neuber concept of fictitious notch rounding*, International Journal of Fatigue, Vol. 51, p. 105-115, (2013)

[39] HBM Prenscia nCode: `https://www.ncode.com/`

[40] T.Marin, G.Nicoletto: *Fatigue design of welded joints using the finite element method and the 2007 ASME Div. 2 Master curve*, Frattura ed integrità strutturale, Vol. 9, p. 76-84, (2009)

[41] P.Dong: *A structural stress definition and numerical implementation for fatigue analysis of welded joints*, International Journal of Fatigue, Vol. 23, p. 865-876, (2001)

[42] P.Dong, J.K.Hong, Z.Cao: *Stresses and stress intensities at notches: 'anomalous crack growth' revisited*, International Journal of Fatigue, Vol. 25, p. 811-825, (2003)

[43] G.Glinka, G.Shen: *Universal Features of Weight Functions for Cracks in Mode I*, Engineering Fracture Mechanics, Vol. 40, p. 1135-1146, (1991)

[44] S. Mikheevskiy: *Elastic-Plastic Fatigue Crack Growth Analysis under Variable Amplitude Loading Spectra*, PhD thesis, University of Waterloo, (2009)

[45] A.H.Noroozi, G.Glinka, S.Lambert: *A two parameter driving force for fatigue crack growth analysis*, International Journal of Fatigue, Vol. 27, p. 1277-1296, (2005)

[46] A.H.Noroozi, G.Glinka, S.Lambert: *A study of the stress ratio effects on fatigue crack growth using the unified two-parameter fatigue crack growth driving force*, International Journal of Fatigue, Vol. 29, p. 1616-1633, (2007)

[47] S.Mikheevskiy, G.Glinka: *Elastic–plastic fatigue crack growth analysis under variable amplitude loading spectra*, International Journal of Fatigue, Vol. 31, p. 1828-1836, (2005)

[48] S. Bogdanov: *Fatigue Life Prediction Based on the Advanced Fatigue Crack Growth Model and the Monte-Carlo Simulation Method*, PhD thesis, University of Waterloo, (2014)

[49] *Eurocode 3: Design of steel structures, Part 1-9: Fatigue*, BSI, (2010)

[50] J. Maierhofer, H.-P. Gänser, R. Pippan: *Crack closure and retardation effects – experiments and modelling*, Procedia Structural Integrity, Vol. 4, p. 19-26, (2017)

[51] V. Tvergaard: *Effect of underloads or overloads in fatigue crack growth by crack-tip blunting*, Engineering Fracture Mechanics, Vol. 73, p. 869-879, (2006)

[52] V. Infante, C. M. Branco, R. Martins: *A fracture mechanics analysis on the fatigue behaviour of cruciform joints of duplex stainless steel*, Fatigue & Fracture of Engineering Materials & Structures, Vol. 26, p. 791-810, (2003)

[53] Liang Zong, Gang Shi, Yuan-Qing Wang, Jia-Bao Yan, Yang Ding: *Investigation on fatigue behaviour of load-carrying fillet welded joints based on mix-mode crack propagation analysis*, Archives of Civil and Mechanical Engineering, Vol. 17, p. 677-686, (2017)

[54] Liang Zong, Gang Shi, Yuanqing Wang: *Experimental investigation on fatigue crack behavior of bridge steel Q345qD base metal and butt weld*, Materials and Design, Vol. 66, p. 196-208, (2015)

[55] Peng-Hsiang Chang, Tso-Liang Teng: *Numerical and Experimental Investigations on the Fatigue Life Evaluation of Butt-Welded Joints*, Metals and Materials International, Vol. 14, p. 361-372, (2008)

[56] E.J. Kaufmann, B.R. Metrovich, A.W. Pense: *Characterization of Cyclic Inelastic Strain Behavior On Properties of A572 Gr.50 and A913 Gr.50 Rolled Sections: Final Report to American Institute of Steel Construction*, ATLSS, ATLSS Report N°01-13, (2001)

[57] ASM International Handbook Committee: *ASM Handbook: Volume 19 Fatigue and Fracture*, ASM International, (1997)

[58] Taylor Mac Intyer, Fonseca Junior, Rodrigo Magnabosco: *Evaluation of methods for estimating fatigue properties applied to stainless steels and aluminum alloys*, Tecnologia em Metalurgia, Materiais e Mineração, Vol. 9, p. 284-293, (2012)

[59] Muhammad Waqas Tofique: *Very high cycle fatigue of duplex stainless steels and stress intensity calculations*, Licentiate Thesis, Karlstad University Studies, (2014)

[60] Eurocode's site: `https://eurocodes.jrc.ec.europa.eu/`